

SPIN ORBIT TORQUE DRIVEN MAGNETIC SWITCHING IN THREE
TERMINAL MAGNETIC TUNNEL JUNCTIONS

A Dissertation

Presented to the Faculty of the Graduate School
of Cornell University

In Partial Fulfillment of the Requirements for the Degree of
Doctor of Philosophy

by

Shengjie Shi

May 2019

© 2019 Shengjie Shi

SPIN ORBIT TORQUE DRIVEN MAGNETIC SWITCHING IN THREE TERMINAL MAGNETIC TUNNEL JUNCTIONS

Shengjie Shi, Ph. D.

Cornell University 2019

As the world has growing needs for storage of information, searching for the new generation memory technology that is non-volatile, energy efficient, and can be compatible with silicon technology is one of the popular topics of academic as well as industrial research. In this dissertation I present experimental work on various spin-orbit-torque driven switching behaviors and possible application of these phenomena. I show that with novel methods of material optimization and structural modification, three terminal magnetic tunnel junctions with in-plane anisotropy can rise up to the front of this search and can possibly change the memory writing scheme in the future. From the beginning of this century, spintronics has gained much attention due to its rich and intriguing physics. The possibility of manipulating magnetization locally through angular momentum exchange by the spin orbit coupling also advances the magnetic storage technology from field-driven to current-driven switching, which significantly enhances the compatibility and scalability of these elements. After the introduction in Chapter 1, I show some switching experiments on micron-sized Hall bar structures with perpendicular magnetic anisotropy (PMA) in Chapter 2. I discuss the significance of various works on PMA structures and the popularity of future direction of the research. In Chapter 3 and 4 I describe the nano-fabrication procedures and novel measurement techniques that I built and used to obtain the switching results that will be introduced in the subsequent chapters. In Chapter 5 I show an effective

way of reducing write current in three terminal magnetic tunnel junctions (MTJs) using sub-atomic Hf dusting layers and explore the various properties of this technique. In Chapter 6 and 7 I mainly focus on fast, nanosecond pulse switching of MTJ devices based on the $\text{Pt}_{85}\text{Hf}_{15}$ alloy spin Hall channel. I present some novel ways of manipulating spin torque switching dynamics and how we can obtain enhanced switching behavior with the modification of device geometries. Finally in Chapter 8 I briefly touch on the set-up of a high frequency low temperature cryostat and some interesting and yet-to-be-understood phenomena of spin-torque switching in the low temperature regime where the amplitude of thermal fluctuations is low.

BIOGRAPHICAL SKETCH

Shengjie was born in 1990 in Jiangsu Province, China. Soon after he was born, his family moved to Shanghai, where his grandparents worked and lived for years, and have settled down since then. Growing up in the 90s when the economy started booming and the cultural environment underwent dramatic change, Shengjie spent joyful childhood time exploring a wide scope of interests including art, literature as well as science. Though having a talent in languages, he started to appreciate the beauty of math and physics in high school. Thanks to the high-level science education in the high school, he developed a systematic understanding of physics and decided to major in this field in college. He successfully got enrolled in Shanghai Jiao Tong University, one of the most prestigious universities in China. After four years of undergraduate study, he was not satisfied with what he had achieved, and wanted to step onto a higher platform to continue his interest in physics research. He applied and got accepted by Cornell University, where he had six memorable years living a completely different life overseas. He joined Prof. Buhrman's spintronics group in 2014. It was happy and fruitful four years in Buhrman lab with adorable people and exciting projects. He helped to develop a new generation of magnetic memory that could potentially change tomorrow's storage scheme. With all he has achieved, he decided that it is time to move on to a new stage of his life.

To my parents, if I ever become someone who changes the world, you are the reason.

ACKNOWLEDGMENTS

Among all the people I'm thankful to, I would like to first thank my advisor, Bob Buhrman for his excellent coaching and his continuous trust in me, which give me the confidence and the opportunity to do exciting research in this field. To me Bob's ability to oversee the big picture of the research and directing us to a promising path impresses me the most. I can always gain wisdom from discussing with him, both within research and within life. He has been kind and caring, always encouraging when I stumble in research. It is a pleasure and great honor working with him and those four years will always stay fresh in my memory. I would also like to thank my other committee members, Prof. Fuchs and Prof. Kim, for their support during this time, and for beneficial discussions we have had.

I would like to thank my group members, Yongxi and Minh-Hai, who taught me about the basic fabrication techniques when I first joined the group. I also remember the days we had together as rookie graduate students trying to survive E&M and quantum mechanics. Those were very special and memorable days in my life. Yongxi and I worked together in many projects and became close friends. We helped each other and achieved many things together. We had interesting discussions about all kinds of things in life, politics, literature, etc. I wish that someday in the future we would once again work together. I would like to thank Graham and Sri, who taught and guided me into MTJ fabrication and measurements, which became the foundation of my primary research later in the days. They are patient and are willing to help any time I had questions or confusions. I remember the road trips with Sri to those sponsor meetings – always a long trip but never boring at all. I also want to thank Ryan and Lijun, who joined our group after me but certainly helped me in many ways along the recent years. There are a couple of people in Prof. Ralph group who I worked with, Colin,

Neal, and Greg. I'm thankful for their help with the setup building and many other aspects.

I would also like to give my thanks to the CNF staff who helped me with the fabrication along the years, Garry, Alan, John, Amrita, Jerry, Aaron. Also thank CCMR staff Steve and Mick for various kinds of equipment operation and FIB work.

Of course nothing can be achieved without the strong support from my parents and family. I have the courage and the strong will to always step forward knowing you all will be standing behind me. I know whatever happens you will be with me, and there's always a home where I feel safe and warm no matter how much I get hurt. I wanted to thank my best friend Yifan with whom I always had a good time, studying, travelling, laughing and supporting each other, whether we are on the same land or separated far apart. Chloe, you gave me the fantastic three years I never dreamt of. I wouldn't be who I am now if it wasn't you coming into my life. Shihao, we had joyful days as young, naive PhD students, and we did a lot of stupid things together. Those are good memories.

Time flies very fast. I still remember the day I received the acceptance letter from Cornell and now I'm about to graduate. The six-year life has been long, long enough that it occupies a permanent place in my heart. It has been short – so short that I didn't even have time to enjoy it enough and it's gone.

It brings me the new life, a life that I couldn't imagine having when I sat by my window watching beautiful snowfall that came once in a few years in my hometown. It brings me the piece of tranquility and serenity that lets me re-think about life and future. It changes me, to who I am now.

To the beautiful days.

TABLE OF CONTENTS

LIST OF FIGURES	xi
LIST OF TABLES	xvi
LIST OF ABBREVIATIONS	xvii
1 INTRODUCTION	1
1.1. From spin transfer torque to spin orbit torque	1
2.2 Magnetic tunnel junctions and SOT-MRAM	6
2 MAGNETIC AND CURRENT INDUCED SWITCHING IN PERPENDUCULARLY MAGNETIZED HALL BAR STRUCTURES	13
2.1. Magnetic reversal in heterostructures with tilted magnetic anisotropy	13
2.2 Current induced switching in antiferromagnet PtMn	22
3 FABRICATION OF THREE TERMINAL MAGNETIC TUNNEL JUNCTIONS	31
3.1. Film growth	31
3.2 Fabrication procedures	32
3.2.1 Alignment marks	32
3.2.2 Spin Hall channel	35
3.2.3 MTJ pillar and contact vias	39
3.2.4 Top contact	44
3.2.5 Miscellaneous procedures	45
4 CONSTRUCTION OF A HIGH FREQUENCY SETUP FOR PULSE MEASUREMENT OF MTJS	46
4.1. General MTJ measurement technique	46
4.2 NI-DAQ based high-speed pulse measurement technique	47
5 ACHIEVING LOW SWITCHING CURRENT IN 3T-MTJS THROUGH MODIFICATION OF MAGNETIC INTERFACES	54
5.1. Enhancement of perpendicular magnetic anisotropy through an atomic layer of Hf at FeCoB/MgO interface	54
5.2 Switching of the MTJs with a Hf dusting layer	60
5.3 Temperature dependence of Hf dusting effect	66
5.4 Control of magnetic damping through additional Hf spacer layer	71
6 FAST AND RELIABLE SWITCHING IN $\text{Pt}_{85}\text{Hf}_{15}$ BASED IN PLANE MAGNETIC TUNNEL JUNCTIONS	82
6.1. Fast pulse switching using $\text{Pt}_{85}\text{Hf}_{15}$ alloy as the spin Hall channel	82

6.2 Highly reliable SOT switching at short pulse durations.....	90
7 VARIOUS NOVEL SWITCHING PHENOMENA IN IN-PLANE MAGNETIZED MAGNETIC TUNNEL JUNCTIONS	94
7.1. Size and shape dependence of the switching current of in-plane magnetized MTJs	94
7.2 Switching of MTJs with an easy axis parallel to the spin Hall channels	104
8 CONSTRUCTION OF HIGH FREQUENCY LOW TEMPERATURE MEASUREMENT SYSTEM AND THE SWITCHING BEHAVIOR OF MTJS AT LOW TEMPERATURES.....	112
8.1 High frequency low temperature measurement system and its operation	112
8.2 Field switching behavior and DC current induced switching at low temperatures	118
8.3. Low temperature FMR measurements	126
8.4. Switching of the MTJs under short voltage pulses at low temperatures	128
REFERENCES	132

LIST OF FIGURES

Fig. 1. 1 Magnetization dynamics with the presence of spin transfer torques. Figure reproduced from Locatelli et al. ⁶	3
Fig. 1. 2 Steady state precession or magnetic reversal caused by spin transfer torques. Figure reproduced from Ralph and Stiles ⁷	4
Fig. 1. 3 A comparison of 3T-MTJ switched by SHE and a 2T-MTJ switched by STT ⁷	7
Fig. 1. 4 Comparison of different geometries for SOT switching. Figure reproduced from Fukami et al. ³²	10
Fig. 1. 5 Different switching regimes at different applied current pulse time scales. Figure reproduced from Bedau et al. ⁴¹	12
Fig. 2. 1 Tilted magnetic anisotropy induced by a wedge structure in the FeCoB nanodot. (reproduced from You et al. ³⁹)	15
Fig. 2. 2 Sputtering procedure used in Hellman et al. where Tb and Fe guns are tilted towards the substrate. The graph on the right shows measured tilt angles from the perpendicular direction with the change of Tb concentration in the alloy. (Reproduced from Hellman et al. ⁴⁹)	16
Fig. 2. 3 (a), Sputter configuration for TbCoFe layer. (b), Hall bar structure and dimensions	17
Fig. 2. 4 Labeling convention for the TbCoFe Hall bar device wafer. The resistance results show that the thickness of the film stack increases in the direction depicted by the arrows.	17
Fig. 2. 5 Anomalous Hall loops of TbCoFe samples at different thicknesses. (a), In-plane anisotropy (b) and (c), Tilted anisotropy (d), Out-of-plane anisotropy	20
Fig. 2. 6 Transition from in-plane to out-of-plane anisotropy in CoFeB films.	21
Fig. 2. 7 AMR measurements with a fixed field scanning 360° in plane on TbCoFe tilted samples	22
Fig. 2. 8 Comparison between PtMn-FeCoB PMA structures with and without a Hf Spacer. Anomalous Hall loops with out-of-plane field scan.	24
Fig. 2. 9 Anomalous Hall response of sample A with external field scanned in hard axis directions (x and y directions)	25
Fig. 2. 10 Current induced switching in PtMn samples with an in-plane field applied along the current direction, as explained by domain nucleation and propagation model.	28
Fig. 2. 11 Unidirectional switching of specially shaped nanodots. (Reproduced from Safeer et al. ⁴⁶)	28
Fig. 2. 12 Current switching phase diagram of a PtMn sample.	30
Fig. 3. 1 Fabrication flow of three terminal MTJs	32

Fig. 3. 2 Sizes and locations of alignment marks for MTJ fabrication	33
Fig. 3. 3 Ion source parameters for etching the spin Hall channels.....	37
Fig. 3. 4 An AFM image of a completed spin Hall channel with a nominal width of 300 nm and measured width of 290 nm.	38
Fig. 3. 5 An AFM image showing a failed spin Hall channel with "fence" on the edge of the channel	39
Fig. 3. 6 An example of an E-beam job file	41
Fig. 3. 7 An AFM image showing a successfully lift-off of E-beam resist, which exposes a hole on top of the MTJ pillar for subsequent top contact deposition.....	43
Fig. 3. 8 A microscopic image showing a completed MTJ device. The two bright triangles are two contact vias.	44
Fig. 4. 1 A schematic picture of general MTJ measurement method.....	46
Fig. 4. 2 NI-DAQ card, ports and wires	49
Fig. 4. 3 Wiring diagram for the fast pulse measurement setup.....	50
Fig. 4. 4 Time sequence of NI-DAQ based fast pulse measurement	52
Fig. 4. 5 Pulse shape of a 1 V pulse at different durations from two pulse generator models 10100 and 10070A.....	53
Fig. 5. 1 A comparison of anomalous Hall response of the structure Ta(1)-W(4)-FeCoB(0.8)-Hf(wedge)-MgO-Ta(1.5) with different Hf layer thicknesses	57
Fig. 5. 2 Anomalous Hall response of the structure W(4)-FeCoB(t)-Hf(0.1)-MgO-Ta (annealed at 300 °C) with easy axis (a) and hard axis (b) scan of the external magnetic field.....	58
Fig. 5. 3 Perpendicular anisotropy energy density at different annealing temperatures for a structure W(4)-FeCoB(t)-Hf(0.1)-MgO-Ta (a) and XPS measurements done on a structure W(4)-FeCoB(1.8)-Hf(0.3)-MgO-Ta (b)	59
Fig. 5. 4 Device schematic and an SEM image of an MTJ pillar on a W spin Hall channel.....	61
Fig. 5. 5 Comparison of W5 and W10 devices. (a), Magnetic minor loop (b), Current induced switching loop.....	62
Fig. 5. 6 Current ramp rate measurements on W5 and W10 devices and fitting results	63
Fig. 5. 7 FMR measurements on W5 and W10 samples. (a), Comparison of 9 GHz resonances of the two samples, showing a large shift of the resonance field with Hf dusting. (b) and (c), Resonance raw data and fitting. (d), Fitting to the Kittel model and extracted M_{eff} showing a large reduction with Hf dusting layer.....	65
Fig. 5. 8 M_{eff} of MTJ structures with different Hf dusting thicknesses.....	66
Fig. 5. 9 W5 devices annealed at different temperatures, 240 °C and 300 °C. (a), FMR measurements showing reduced M_{eff} at the higher annealing temperature. (b), Switching experiments confirm the reduction of I_{c0} at the higher annealing temperature.	67

Fig. 5. 10 Saturation magnetization M_s at two different annealing temperatures, 240 °C and 300 °C.	68
Fig. 5. 11 M_{eff} in various structures at various annealing temperatures. W10 – without Hf dusting layer. W13 – with 0.05 nm Hf dusting layer. W5 – with 0.1 nm Hf dusting layer.	69
Fig. 5. 12 (a), TMR of W5 and W10 devices at different annealing temperatures. (b), A thinner Hf dusting layer and higher annealing temperature result in much higher TMR.	70
Fig. 5. 13 Comparison of damping α between W5 and W9 samples both annealed at 240 °C.....	72
Fig. 5. 14 A summary of M_{eff} in various structures at different annealing temperatures	73
Fig. 5. 15 Current induced switching in Hf dusting - Hf spacer sample (W9) and comparison of I_c between W9 and W5.	74
Fig. 5. 16 Ramp rate measurements on a W9 device with both Hf dusting and Hf spacer layers. An average of $I_{c0} = 115 \mu A$ and $\Delta = 36$ is achieved.	75
Fig. 5. 17 ST-FMR measurement on two structures with Hf dusting + Hf spacer and without any Hf insertion layers, both annealed at 240 °C.....	76
Fig. 5. 18 Pulse switching probabilities of a W9 device annealed at 240 °C for polarities (a), AP→P (b), P→AP.	79
Fig. 5. 19 Pulse switching phase diagrams of a W9 device annealed at 240 °C.....	80
Fig. 5. 20 WER measurement on a W9 device annealed at 240 °C. WER as low as 10^{-6} can be achieved for both switching polarities.	81
Fig. 6. 1 Typical field and current switching loops of Canon4-7 devices.....	84
Fig. 6. 2 A typical set of switching phase diagrams of a Canon4-7 device. (a) and (b) show macrospin fit to the whole duration range. (d) shows an imaginary shift of the pulse curve upward for P→AP polarity which makes it look less asymmetric from AP→P in (c). (e) and (f) show the new fitting scheme that captures the same $V_0 \sim 2V_0$ regime for both polarities, regardless of the V_0 in each polarity. White dashed lines are guide to the eyes. For these devices, the $V_0 \sim 2V_0$ regime usually falls into 0.5 ns ~ 3 ns region.	87
Fig. 6. 3 Switching phase diagrams of a Canon4-7 device with different offset field. (c) and (d) have an offset field of 4 Oe greater than (a) and (b), which effectively adjusted the symmetry of the two polarities. The new fitting scheme yield almost the same results regardless of the V_0 change.....	88
Fig. 6. 4 Write error rate measurement on different shapes at different pulse durations. WER has a steep decrease at large pulse amplitude regardless of the shapes and can reach 10^{-6} for both P→AP and AP→P polarities.	91
Fig. 6. 5 WER measurement on a Canon4-7 device with slightly different offset field. As the field is tuned, the switching transitions from favoring one polarity to the other.	92

Fig. 6. 6 WER measurements on two different samples with the same nominal design, showing reliability of these SOT devices with WER $\sim 10^{-5}$ down to 200 ps pulse duration.	93
Fig. 7. 1 TEM image of an MTJ showing the cross section of the pillar with elements denoting materials in each layer. Instead of a sharp profile, a long tail of ~ 20 nm long at the bottom of the MTJ is observed, which causes the actual FL aspect ratio to be smaller than designed.	96
Fig. 7. 2 MTJ resistances at different sizes. Row 1 denotes the largest size 220×86 nm ² and row 7 the smallest 160×62 nm ²	97
Fig. 7. 3 Zero-temperature critical current in MTJ devices with different sizes ranging from largest in row 1 to smallest in row 7.	98
Fig. 7. 4 Possible explanation for the I_{c0} decrease with smaller MTJ sizes. (a), Larger devices has a smaller tapered area due to the limitation of the channel width. (b), Tapered region has tilted magnetic anisotropy, which helps the activation of the magnetization precession and switching. (Part (b) reproduced from Ref. 4)	100
Fig. 7. 5 SEM images showing various shapes of the MTJ pillars with the same nominal area. (a), regular rectangle (b), triangle (c), dumbbell (d), diamond (Note that (d) has a different scale from the other three images. Yellow lines are channel contours as guide to the eyes.)	101
Fig. 7. 6 Comparison of the critical switching current in various shaped MTJs with the same nominal size.	103
Fig. 7. 7 Comparison of rectangle and diamond devices with slightly varying sizes.	104
Fig. 7. 8 Field switching minor loop and current induced switching with out-of-plane external field in an orthogonal device.	106
Fig. 7. 9 Current induced switching in an orthogonal device with different applied external field. The device can be switching at zero field and even at opposite field that would otherwise give switching in an opposite polarity.	108
Fig. 7. 10 Pulse switching probability of an orthogonal device (190×45 nm ²) with an applied external field $H_z = 1000$ Oe.	109
Fig. 7. 11 Pulse switching behavior of an orthogonal device with different applied z field.	109
Fig. 7. 12 Comparison of fast pulse switching characteristics between orthogonal devices and collinear devices.	111
Fig. 8. 1 A picture showing the details of the high frequency sample positioner for low temperature measurements	113
Fig. 8. 2 Delrin baffles used to hold RF cables in place.	114
Fig. 8. 3 Sample holder and various waveguides for high frequency measurement ..	115
Fig. 8. 4 Transmitted signal at room temperature and low temperatures at different frequencies.	116
Fig. 8. 5 Bonding diagram for MTJ samples on high frequency waveguides.	117

Fig. 8. 6 Major magnetic loops of an IrMn-pinned sample from room temperature to 100 K	119
Fig. 8. 7 Major magnetic loops of an IrMn-pinned sample from 40 K to 5 K	120
Fig. 8. 8 Minor magnetic loops of an IrMn pinned sample at low temperatures	121
Fig. 8. 9 DC current induced switching of an IrMn pinned sample at various temperatures	123
Fig. 8. 10 Temperature dependence of TMR, coercivity and switching current of a Canon Large 1 device	124
Fig. 8. 11 Channel resistance of the Canon Large 1 sample at various cryogenic temperatures	125
Fig. 8. 12 Major (a) and minor (b) loops of a Canon Large 1 sample at low temperatures	126
Fig. 8. 13 FMR measurement on Canon 1 sample	127
Fig. 8. 14 (a), Field and DC current switching of a typical W5 device (b), ramp rate measurement of the W5 device	129
Fig. 8. 15 Pulse switching probability curves for a W5 device for P→AP and AP→P polarities (a) and (b), along with 50% probability points and macrospin fitting (c) and (d)	130
Fig. 8. 16 Pulse switching phase diagrams of a W5 device at 4 K.....	131

LIST OF TABLES

Table 3. 1 ASML resist stack with spinning and baking protocols.....	35
Table 3. 2 E-beam resist stack with spinning and baking protocols	40
Table 3. 3 Parameters for oxygen plasma etch of PMMA/OmniCoat resist stack.....	42
Table 5. 1 Comparison of J_{c0} between the different 3T-MTJ structures reported to date	77

LIST OF ABBREVIATIONS

AHE	Anomalous Hall effect
AMR	Anisotropic magnetoresistance
FM	Ferromagnetic layer
FMR	Ferromagnetic resonance
FL	Free layer
HM	Heavy metal
MTJ	Magnetic tunnel junction
SHE	Spin Hall effect
SOT	Spin orbit torque
STT	Spin transfer torque
PMA	Perpendicular magnetic anisotropy
TMR	Tunneling magnetoresistance

CHAPTER 1

INTRODUCTION

1.1. From spin transfer torque to spin orbit torque

In the early 20th century when people first discovered that electrons can carry angular momentum in their spin they did not realize that this property can become the fundamental building block of the modern information storage technology. In 1988 a phenomenon called giant magnetoresistance (GMR) based on spin-dependent scattering in ferromagnetic materials which gives a distinct high or low resistance state in a ferromagnet/non-magnetic/ferromagnet (FM/NM/FM) sandwiched structure was discovered and turned into applications in read heads and sensors now used widely in various kinds of electronics^{1,2}. In 1996 Slonczewski and Berger succeeded in predicting a more complicated application of the electron spins where the spin polarized electrons can exert a spin transfer torque (STT) on the magnetization of the FM through the exchange of angular momentum and result in the reversal of the magnetization direction^{3,4}. More recently people discovered that the interaction between electron spins and atomic orbital momentum in certain heavy metals results in accumulation of large spin polarization and spin orbit torque (SOT), which is known as the spin Hall effect (SHE)⁵. These findings stimulated the emergence of a new scientific branch called spintronics, which focuses on utilizing the electron spin to manipulate magnetization orientation and dynamics.

To describe the precessional motion of the magnetization in a non-equilibrium configuration, Landau, Lifshitz and Gilbert introduced an equation with a damping

term,

$$\frac{d\mathbf{M}}{dt} = -\gamma \mathbf{M} \times \mathbf{H}_{\text{eff}} + \frac{\alpha}{M_s} \mathbf{M} \times \frac{d\mathbf{M}}{dt} \quad (1.1)$$

where γ is the gyromagnetic ratio, α is the damping factor and M_s is the saturation magnetization. The second term on the right-hand side is the phenomenological damping term that dissipates energy of the system and tends to align the magnetization along the effective field direction. Note that in some cases this model can be more easily treated using the macrospin approximation where the magnetic element is modeled as one uniform spin. However, in other cases even when the size of the element is small, the microscopic details of the magnetic behavior, the micromagnetics, needs to be taken into account to explain more complicated domain related behaviors, which will be covered and discussed in later chapters of this dissertation. When there is an interaction between the spin polarized electrons and the magnetic moment, an adapted equation including two more terms is required,

$$\frac{d\mathbf{M}}{dt} = -\gamma \mathbf{M} \times \mathbf{H}_{\text{eff}} + \frac{\alpha}{M_s} \mathbf{M} \times \frac{d\mathbf{M}}{dt} + \tau_{\parallel} \mathbf{M} \times (\boldsymbol{\sigma} \times \mathbf{M}) + \tau_{\perp} (\boldsymbol{\sigma} \times \mathbf{M}) \quad (1.2)$$

where $\boldsymbol{\sigma}$ is spin polarization, τ_{\parallel} and τ_{\perp} are in-plane and out-of-plane spin torques.

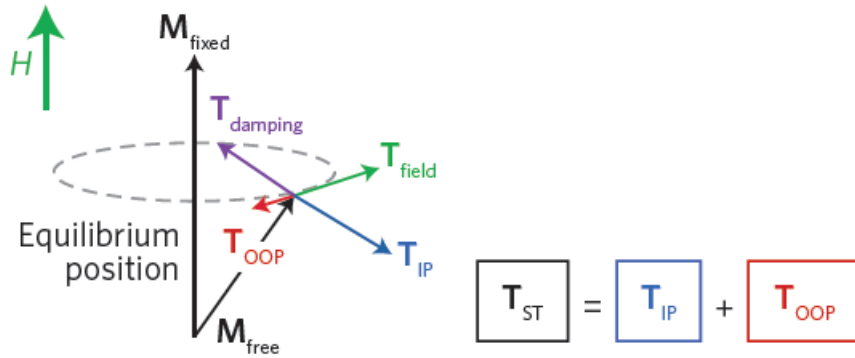


Fig. 1. 1 Magnetization dynamics with the presence of spin transfer torques. Figure reproduced from Locatelli et al.⁶

As illustrated in Fig. 1.1, the in-plane spin transfer torque acts against the dissipative damping torque and another torque, usually called the field-like torque that is usually small compared to the spin transfer torque, acts in the perpendicular direction and acts to cause the magnetization to precess around the effective field. For an electric current passing through a multilayer stack patterned into nanopillars, the current becomes spin polarized when it passes through an FM layer with uniaxial anisotropy. This spin polarization interacts with the second FM layer and can switch the second layer through the spin transfer torque (Fig. 1.2). For applications, the spin transfer torque relies on two magnetic layers acting as filters to polarize and detect the electric current, in devices where the current flow is perpendicular to the plane of the magnetic layers, which is referred to as the CPP geometry.

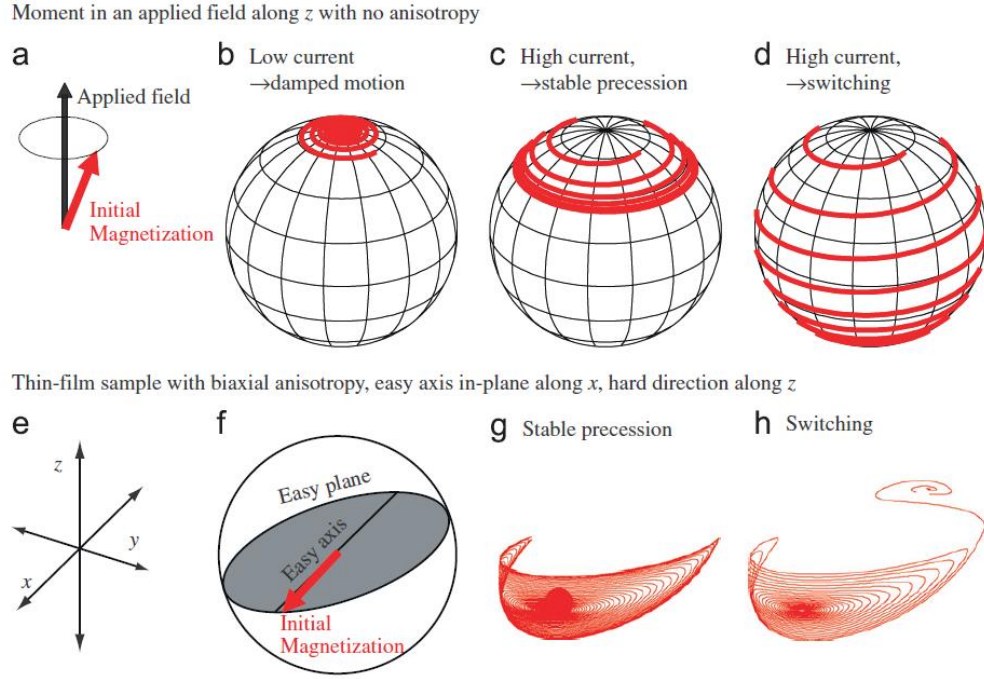


Fig. 1. 2 Steady state precession or magnetic reversal caused by spin transfer torques. Figure reproduced from Ralph and Stiles⁷.

More recently a new spin torque switching mechanism has been discovered which does not require an FM layer as the polarizer. It is theoretically predicted and experimentally observed that in certain heavy metals, due to strong spin orbit coupling, an electric current flowing in these materials creates a spin current which is deflected orthogonally and can switch an adjacent FM layer through spin orbit torque^{5,8,9}. The first observations in Ta, Pt and W showed a spin Hall angle, defined as

$$\theta_{\text{SH}} = \left(\frac{2e}{\hbar} \right) \frac{J_s}{J_c}, \text{ as large as } \sim 30\%^{8,10}.$$

Later it was shown that the heavy

metal/ferromagnet (HM/FM) interface plays an important role in determining the strength of the spin torque delivered to the FM through the transparency T , which in turn defines a modified property called spin torque efficiency $\xi_{\text{SH}} = T\theta_{\text{SH}}^{11,12}$. Various

efforts have been made to explore the phenomenon at the interfaces to optimize the efficiency of the spin orbit torque, among which the tuning of the damping and spin memory loss shows significant impact. The spin Hall effect, believed to share similar origin as the anomalous Hall effect, have two mechanisms, namely the intrinsic effect due to band structure and the extrinsic effect due to spin-dependent disorder and impurity scattering. The intrinsic mechanism predicts a spin Hall conductivity unique to the material structure and can be utilized to create high spin torque efficiency materials through alloying^{12–14}. Later people discovered that antiferromagnetic materials (AFMs) can show strong SHE too, which opens up new areas focusing on high frequency spin torque dynamics as well as field-free switching using both SHE and exchange bias effect from the AFM^{15,16}. More recently works have shown that even ferromagnetic materials exhibit SHE, and is sensitive to its magnetism around the Curie temperature^{17,18}. These findings raise interesting ideas of using the same material as the spin source and the spin detector. Furthermore, based on the knowledge that not only electrons carry spin information, spin wave can also interact with local magnetization in non-metallic systems, and people also discovered that certain families of topological insulators can achieve giant SHE with $\xi_{\text{SH}} > 100\%$ ^{19,20}. Although more work is needed to show the applicability of these materials in the next generation magnetic storage systems, these observations greatly enrich the spintronics field and can stimulate both fundamental research of the spin orbit torque and the application of the new technologies in industry.

2.2 Magnetic tunnel junctions and SOT-MRAM

The application of spin torques evolved over the past 20 years from a simple mechanical point contact where the sharp tip confines the electric current into a multilayer stack to sandwich structures as small as 20 nm size thanks to advanced lithography techniques. Spin valve structures that utilizes GMR to read and write information was first developed in the 1980s, and became a popular research topic again in the early 21st century, when Katine et al. first demonstrated switching of Co/Cu/Co structures with electric current²¹. Subsequent research brought about the potential application of this technique in new generation memory technology which is now known as the spin-transfer-torque magnetoresistive random access memory (STT-MRAM)²². STT-MRAM is non-volatile due to the preserved magnetic states when an external switching field or switching current is removed, and can potentially operate at a faster speed than existing SRAM or DRAM due to the high frequency spin dynamics. The development of high tunneling magnetoresistance (TMR) led to a different configuration of these memory elements where two FM electrodes are separated by a thin tunnel barrier, usually an insulating oxide such as Al₂O₃ or MgO²³.

The TMR, which is defined as $TMR = \frac{R_{AP} - R_P}{R_P}$, shows the resistance swing

between the high and low states of the structure governed by the relative orientation of magnetization directions between two FM electrodes, being parallel (P) or anti-parallel (AP). Thus it is dependent upon the spin polarization of the two FM materials, as

shown by $TMR = \frac{2P_1P_2}{1 - P_1P_2}$ ²⁴, where the spin polarization of a specific material is

determined by the spin dependent density of states at the Fermi level

$$P_i = \frac{D_{\uparrow}(E_F) - D_{\downarrow}(E_F)}{D_{\uparrow}(E_F) + D_{\downarrow}(E_F)}^{25}.$$

The utilization of the TMR greatly enhances the ease of the

reading of these magnetic elements thanks to materials with high spin polarization being discovered over the years^{26,27}. This is explained by the coherent lattice matching between (001) plane of body-centered cubic (bcc) CoFeB and (001) plane of MgO upon annealing. Room temperature TMR > 600% and low temperature TMR > 1000% at 4 K have been achieved so far²⁸, which has led to the rapid development of magnetic tunnel junctions (MTJs) that use the FM/tunnel barrier/FM structure²⁹.

Though the focus of widespread research and development efforts with commercial products now being delivered, STT-MRAM suffers from several drawbacks due to its switching and reading mechanism. For example, it can have both write errors and read disturbance due to the shared read and write path. Furthermore, continuous writing through the tunnel barrier can speed up the wear-out of the tunnel barrier and cause device failure after repeated application of high current/bias voltage³⁰.

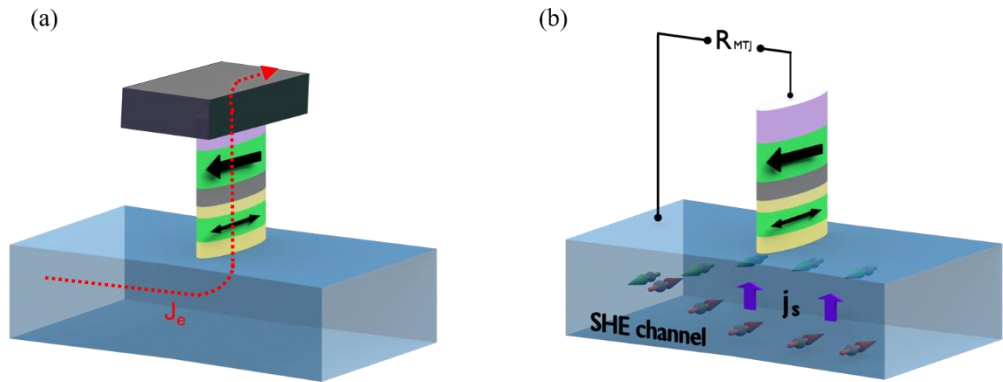


Fig. 1. 3 A comparison of 3T-MTJ switched by SHE and a 2T-MTJ switched by STT

The discovery of SHE offers a different solution to these issues with a new geometry. Liu et al. and Miron et al. showed deterministic bipolar switching of in-plane and perpendicularly magnetized MTJs with electric passing through a spin Hall channel^{8,9}. Figure 1.3 shows the comparison between a three terminal (3T) MTJ switched by SHE mechanism and a conventional STT MTJ. For the 3T-MTJ an electric current is passed in the SHE channel and due to spin orbit coupling in the HM, polarized spins with the polarization direction set by the sign of SHE form a spin current that is deflected toward the magnetic free layer (FL) grown on top of the HM (sometimes with a spacer layer in between, as will be discussed in later chapters). A reference layer (RL) is usually on top of the tunnel barrier and is kept at a preferred direction by exchange bias pinning. The generated spin current from the HM acts on the FL magnetization and switches it through the anti-damping torque. Due to the 3T design and SHE mechanism, the switching current does not go through the MTJ but instead flows in-plane, which greatly reduces the risk of wearing out the tunnel barrier, and in theory allows for a high overdrive voltage to enable improved performances. Meanwhile it circumvents the read disturbance issue since the reading now is separate from the writing path. Furthermore, in the 3T design various properties of the MTJ can be engineered independently without degrading other performances. For example, in Eqn. 1.1 the critical switching current density by a macrospin model predicts a dependence of J_{c0} on damping α , demagnetization field M_{eff} , in-plane coercive field H_c dictated by shape anisotropy and the spin torque efficiency ξ_{DL} .

$$J_{c0} = \frac{2e}{\hbar} \mu_0 M_s t_{\text{FM}} \alpha (H_c + M_{\text{eff}} / 2) / \xi_{\text{DL}} \quad (1.3)$$

For the 3T-MTJs, the demagnetization field is the key factor that determines the J_{c0} since the in-plane coercive field is one order of magnitude smaller. However, the thermal stability factor $\Delta = \frac{1}{2} M_s V H_c / k_B T$ is dominated by H_c . Thus by engineering the stack structure to reduce M_{eff} we can significantly reduce J_{c0} while maintaining a high Δ if we maintain a reasonable H_c which is mainly controlled by patterning of the devices³¹. This could not be achieved in STT devices since reducing the anisotropy usually brings the reduction of the thermal stability Δ at the same time, which makes the switching less robust against thermal fluctuations, causing reliability issues in applications.

While in-plane 3T-MTJs show great promise compared to many other emerging memory technologies, people still try to implement other geometries to address the relatively poor scalability issue that happens when we rely on elongated shapes across the SHE channels to achieve preferred P and AP states. Fukami et al. raised a different geometry in which the MTJ is aligned parallel to the channel direction which could potentially allow for a significantly narrower channel for a smaller footprint of memory device arrays³² (Fig. 1.4). Continuous interest is still in devices with perpendicular anisotropy due to their high scalability. Particularly with SOT switching of perpendicularly magnetized MTJs, the need to apply an in-plane field to enable deterministic switching is not preferable, so worldwide efforts are put into removing this field for better compatibility with the integrated circuits^{16,33–40}.

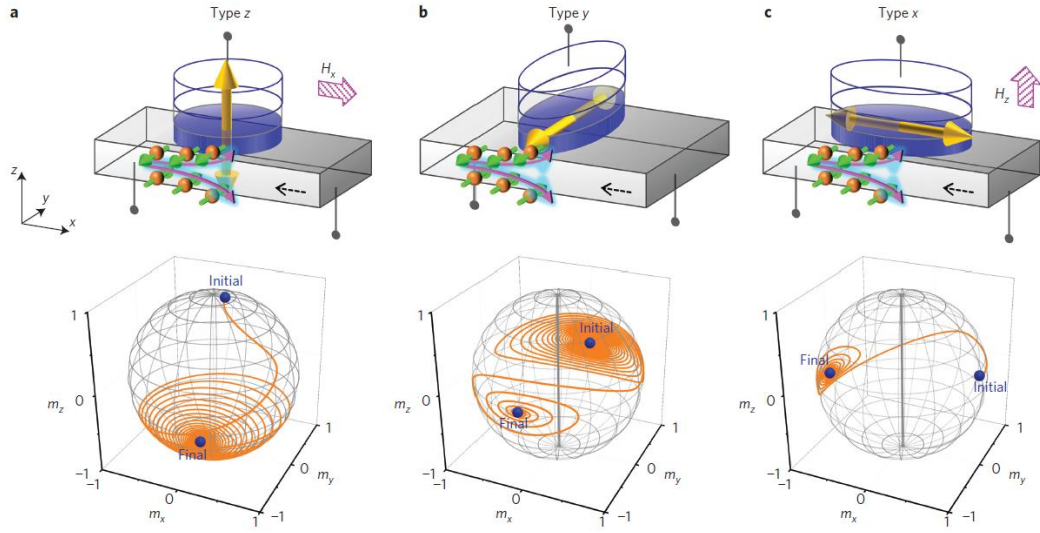


Fig. 1. 4 Comparison of different geometries for SOT switching. Figure reproduced from Fukami et al.³²

One initially surprising thing that in-plane magnetized SOT-MRAMs possess is the surprisingly fast dynamics compared to theoretical predictions. Although anti-damping torques do not act on magnetizations collinear with the spin polarization direction, micromagnetic structures at the edge of the nanometer size device as well as domain formation appear to eliminate the incubation delay which was once thought to be the obstacle for fast switching. There has been some research about different switching regimes at different time scales of the applied current (pulses)^{41–45}. Figure 1.5 shows the behavior of current induced magnetization reversal at different time scales. At the long time scale (usually larger than a few μs) the switching is thermally activated which means that the dynamics is least affected by the initial configuration of the magnetization. However, in the short pulse regime where the time scale is within a few nanoseconds, and where most of the research as well as application focuses on, the initial state can be critical as confirmed by various experimental and

computational works^{46,47} (see Chapter 7 of this dissertation for our related work). The initial state can be controlled actively or passively by the geometry of the sample edge, current induced Oersted field, tapering of the magnetic layer, the field-like torque, uniformity of the switching current, dipole field from the reference layer, etc. Among those methods to manipulate the micromagnetic configurations, via shape modification has gained more attention recently due to advanced lithography technology enabling more accurate control of the device geometry, which makes it no longer an obstacle for commercialization. To minimize the magnetostatic energy, the magnetization at the edge of a geometric shape tends to align slightly differently from the magnetization in the bulk region (in a saturated state), and this distribution can cause different torque distribution due to any current induced effective field. Thus the manipulation of the shape can possibly speed up the switching process by preferably inducing domain nucleation with a larger size or at certain preferred sites. Although it is very difficult to model this due to the complicated switching mechanism in the short pulse regime, more effort in this area will likely bring deeper understanding of the SOT switching and show the potential of these structures in future applications.

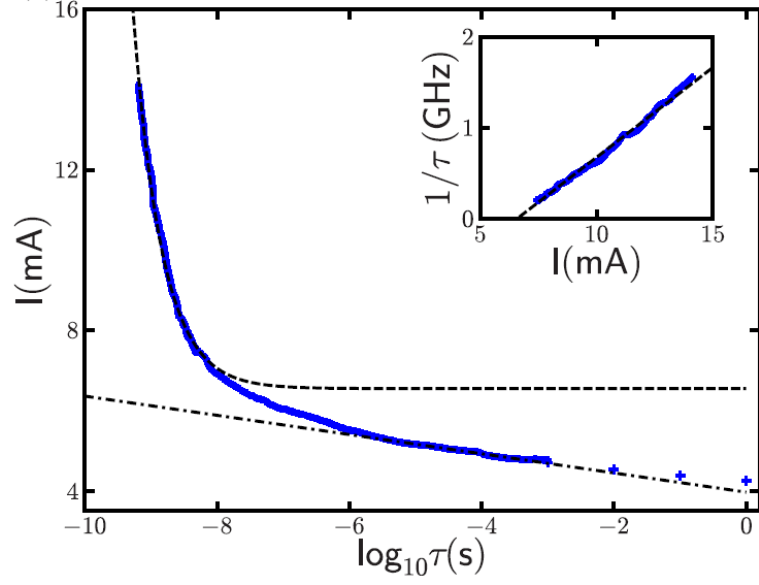


Fig. 1. 5 Different switching regimes at different applied current pulse time scales. Figure reproduced from Bedau et al.⁴¹

Not only does spintronics contribute to information storage technologies, but also it can be useful in ultra-high frequency oscillators, spin logics, terahertz signal transmission and many other frontiers of the new technologies. In the meantime, more experimental and theoretical work is needed to elucidate the debate of underlying mechanism of the spin orbit torques and allow for more exciting discoveries in the near future.

CHAPTER 2

MAGNETIC AND CURRENT INDUCED SWITCHING IN PERPENDUCLARLY MAGNETIZED HALL BAR STRUCTURES

In this chapter we introduce magnetization switching in micron-sized Hall bar structures with magnetic anisotropy that is slightly tilted away from perpendicular direction, which is caused by a special growth condition. We also show that in a Hall bar structure with antiferromagnet PtMn as the spin source, deterministic current induced switching can be achieved, which confirms the strong SHE in PtMn. The deterministic switching of nano-magnets with electric current is crucial to achieving future non-volatile memories that can be scaled down below 10 nm node. While PMA devices can be highly scalable, more work is still needed to demonstrate a feasible method to remove the requirement of an external field that is now applied to assist the current induced switching.

2.1. Magnetic reversal in heterostructures with tilted magnetic anisotropy

In integrated circuits, as the density of the microprocessor increases following Moore's law, people are gradually faced with further difficulty in the scalability of the elements.

The SOT-MRAM utilizes the spin Hall torque to switch an adjacent free layer and shows many advantages over existing and other emerging technologies. However, the three terminal design imposes a larger difficulty in scalability compared to two terminal STT-MRAM designs due to the larger device footprint. In order to minimize the disadvantage of the overall size, a lot of the research focuses on utilizing the pMTJ

(perpendicularly magnetized MTJ) that has both the free layer and reference layer magnetized out-of-plane so that it doesn't rely on the elongated shape of the device to achieve unidirectional anisotropy, thus shrinking the size of the magnetic bits. However, as the mechanism of the spin Hall effect switching indicates, whether the reversal proceeds as indicated by the ideal macrospin model or by the domain nucleation and expansion model, one has to apply an in-plane bias field along the direction of the switching current to achieve deterministic reversals between two opposite states. Although this bias field does not need to be strong in most cases, it adds a complexity to the memory as well as the circuit design. There are currently a few approaches to resolve this issue, including utilizing asymmetry of the layer^{37,48}, adding an in-plane magnetized layer to exert the required bias³⁴, using special substrates³⁵, etc. Another efficient way is to break the symmetry by tilting the perpendicularly magnetized moment slightly towards the in-plane direction. This includes utilizing antiferromagnetic layer and exchange coupling at the interface to pull the moment away from the perpendicular direction³⁸. Although not directly resulting in a broken symmetry, a special kind of ferromagnetic material that has a naturally tilted magnetic anisotropy also attracts people's interest and may be useful in future application of the perpendicular switching.

You et al. reported that by engineering the wedge shape of the magnetic layer in a Ta-FeCoB-MgO-Ta nanodot system, tilted anisotropy can be achieved and enables current induced switching without an external field³⁹. The symmetry is broken through the wedge shape at the edge of the nanodot where magnetization tends to line up with the slope of the wedge (Fig. 2.1). They calculated from their results that a $2^\circ \sim$

5° tilt in their system can successfully replace the in-plane bias field commonly required in this type of deterministic switching experiments. Although these results show promise in demonstrating field-free switching, the careful fabrication and characterization of the wedge of nanometer size could be a big obstacle for further improvements as devices are scaled down. In this manner, looking for a material that has naturally tilted anisotropy induced by crystal structure, which does not rely on complicated patterning is preferable for possible application and mass production.

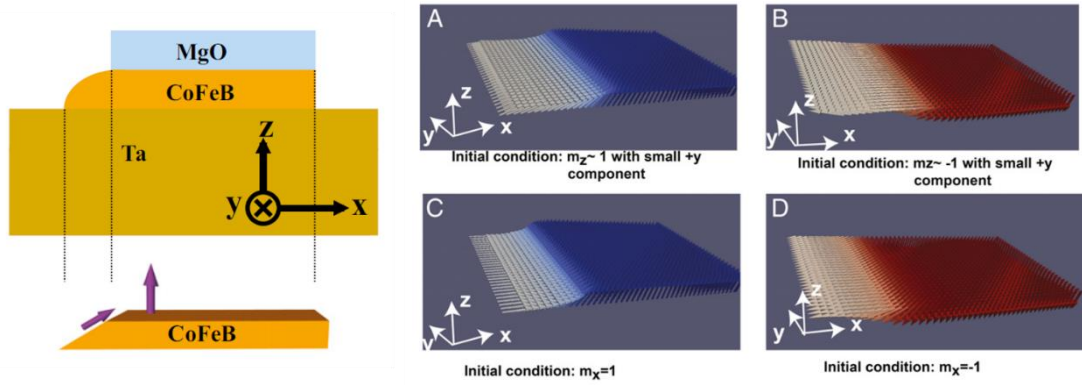


Fig. 2. 1 Tilted magnetic anisotropy induced by a wedge structure in the FeCoB nanodot. (reproduced from You et al.³⁹)

Hellman et al. showed in the 1980s that α -Tb-Fe could show tilted anisotropy due to a non-perpendicular incident angle of the material deposition⁴⁹. Figure 2.2 shows a schematic picture of their sputtering procedure and their measured tilt angles from the perpendicular direction. Tb and Fe targets are tilted towards the substrate and are co-sputtered onto the substrate with no sample rotation, which would otherwise remove the tilt. Their results showed that the tilt angle has a large dependence on the Tb concentration, where more Tb introduces larger tilt angles above the compensation composition at ~ 22%. The phenomenological explanation is that the easy axis of the

sputtered Fe (or Tb) lattice is at an angle compared to the incident angle of the atoms and the tilt leans toward Tb target as Tb concentration increases.

Shiomi et al. also reported tilted anisotropy in $\text{Tb}_x(\text{FeCo})_{1-x}$ films where they attribute the tilt to the single-ion anisotropy of Tb atoms in a local axial electrostatic field due to the substrate bias during the deposition⁵⁰.

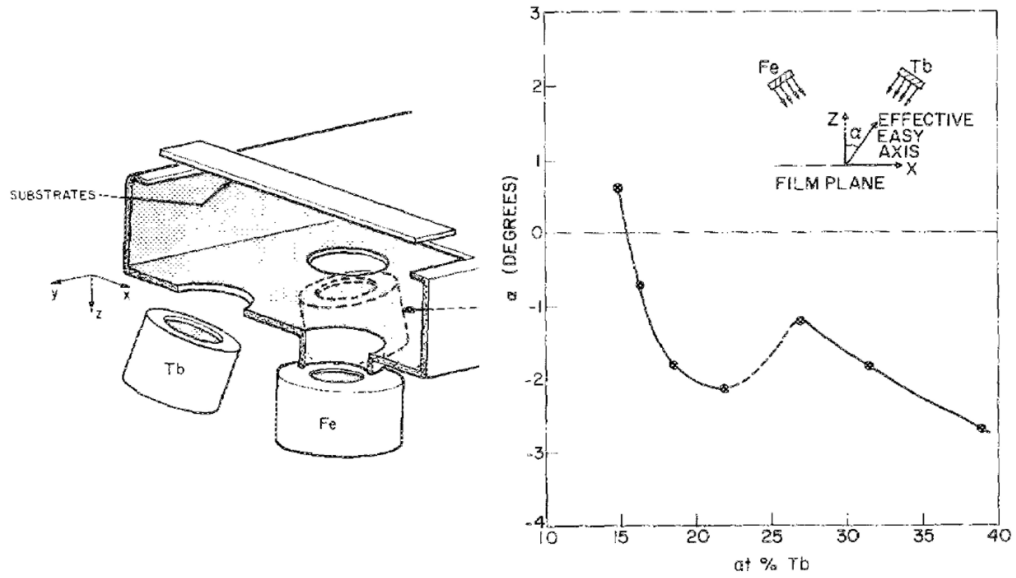


Fig. 2. 2 Sputtering procedure used in Hellman et al. where Tb and Fe guns are tilted towards the substrate. The graph on the right shows measured tilt angles from the perpendicular direction with the change of Tb concentration in the alloy. (Reproduced from Hellman et al.⁴⁹)

To explore the magnetic properties of Tb alloys, I prepared a Ta(1)-TbCoFe(w)-Ta(1)-MgO(2.9)-Ta(1) sample and measured the magnetic response from a Hall bar structure patterned by photolithography and ion beam etching. The TbCoFe layer was co-sputtered with two guns (Tb and CoFe) separated by some distance. In order to achieve the tilted anisotropy, I oriented the sample so that the wafer flat is slightly tilted towards the CoFe gun (Fig. 2.3). I grew a wedged TbCoFe to observe the transition from in-plane to out-of-plane anisotropy.

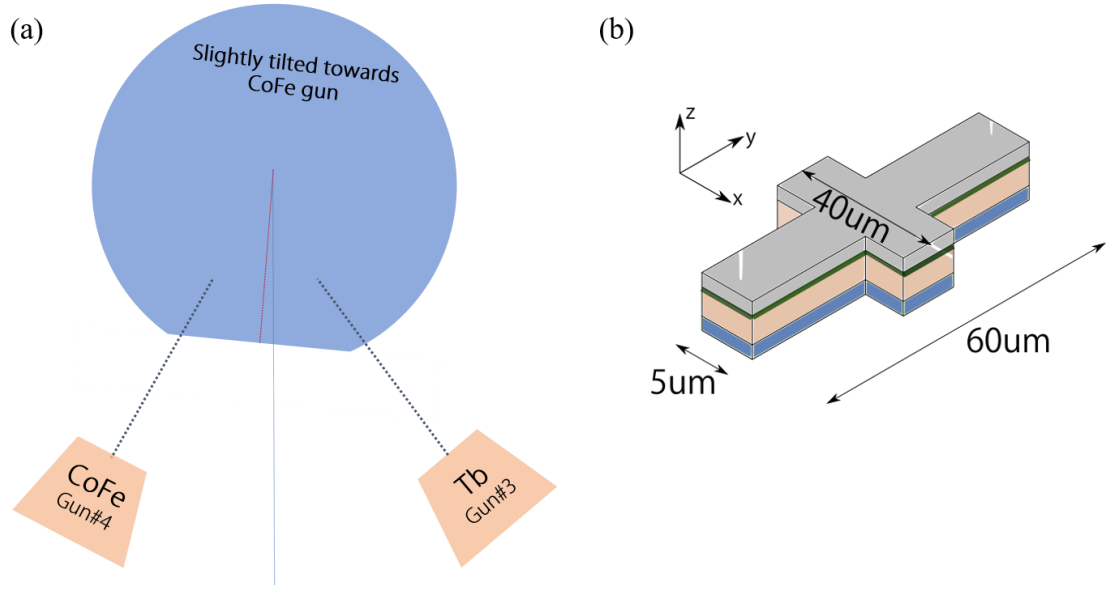


Fig. 2. 3 (a), Sputter configuration for TbCoFe layer. (b), Hall bar structure and dimensions

First, I measured the resistance of the Hall bars in both horizontal and vertical directions to probe the film thickness change across the wafer. Following the convention in Fig. 2.4, I recorded the longer Hall bar (nominally 60 μm long) resistance in Table 2.1.

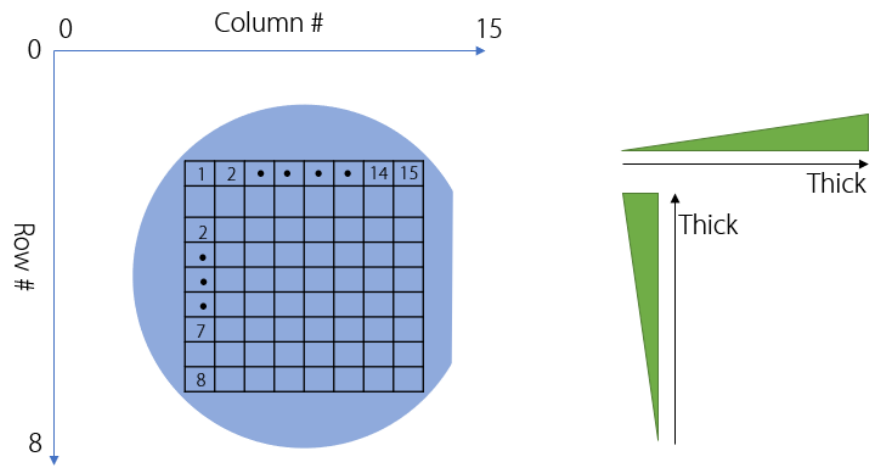


Fig. 2. 4 Labeling convention for the TbCoFe Hall bar device wafer. The resistance results show that the thickness of the film stack increases in the direction depicted by the arrows.

Column Row	1	3	5	7	9	11	13
1		5.09	3.47	2.37	1.65	1.2	0.93
3	7.14	4.88	3.83	2.62	1.88	1.42	1.12
5	7.42	5.98	4.64				
7	8.73	7.51	6.19				Units: k Ω

Table 2.1 Resistance of the TbCoFe Hall bars (in k Ω) across the wafer labelled by row and column numbers

As indicated by the decrease of the Hall bar resistance as it got closer to the longer flat of the wafer, the film thickness increased, which is consistent with the film growth condition where the longer flat is closer to the gun during deposition. However, there is also a clear trend of the film stack getting thicker as it gets closer to the left hand side of the wafer flat, possibly due to the deposition rate of the Tb being lower than that of the CoFe. I then carried out anomalous Hall measurements on these structures, where we apply an AC voltage across the long bar and sweep the field in out of plane direction to the maxima ± 2100 Oe. I probed the induced voltage across the shorter bar, which is directly proportional to the out-of-plane magnetization of the TbCoFe. Figure 2.5 shows an example of measured hysteresis loops of three devices with thickness of the TbCoFe changing from thick to thin. As is common in most of the amorphous magnetic materials, the anisotropy lies in-plane when the magnetic

layer is thick, due to the larger demagnetization field induced by the large lateral dimension. When we swept the out-of-plane field on an in-plane magnetized device, the magnetization rotated with the applied field from up direction to down direction, causing the observed anomalous Hall signal to continuously change from one value to another. In most cases there was a horizontal shift of the hysteresis loop due to the imperfection of the patterning, causing the two parts of the shorter bar being misaligned by a small distance, which induced a background voltage difference that did not vary with the applied field (causing the curve to not center around zero). When the device had out-of-plane easy axis, the anomalous Hall response looked like Fig. 2.5(d) where sharp, square loops indicate abrupt switching of the magnetization from up to down, with a coercive field given by half of the hysteresis loop (in this device ~ 500 Oe). The special feature of the TbCoFe samples lies in thickness range where the easy axis transitions from in-plane to out-of-plane. A distinct canted loop with still sharp switching but gradual change of anomalous Hall resistance before the switching shows an easy axis tilted at some angle from perpendicular direction (Fig. 2.5(b) and Fig. 2.5(c)). The canting behavior is due to the rotation of the magnetization from perpendicularly saturated state to its easy axis before it switches. This behavior is not observed in other systems such as CoFeB and Co, where in the transition from in-plane to out-of-plane the anomalous Hall loops show an “S” shape without hysteresis as depicted in Fig. 2.6.

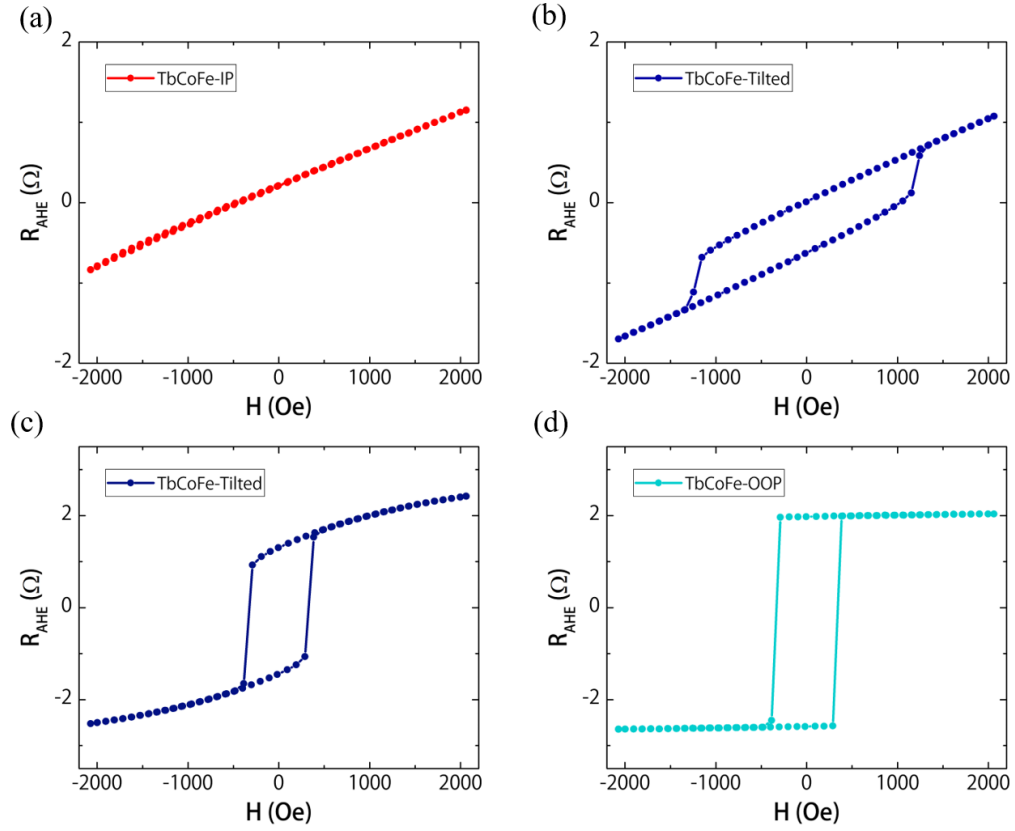


Fig. 2. 5 Anomalous Hall loops of TbCoFe samples at different thicknesses. (a), In-plane anisotropy (b) and (c), Tilted anisotropy (d), Out-of-plane anisotropy

Note that based on the calibration of the deposition, the center of the wafer was targeted at 6 nm TbCoFe thickness, which shows significant bulk PMA. For thinner layers, a coercive field as large as 2000 Oe was observed. Another interesting feature is that during the transition the tilted anisotropy went from small step switching with large hysteresis loops at thinner side to large step switching with small hysteresis loops at thicker side, as shown by the change from Fig. 2.5(b) to Fig. 2.5(c). This behavior qualitatively shows the tilt angle changing from closer to in-plane to closer to out-of-plane. However, the wider hysteresis loop at thicknesses closer to in-plane anisotropy has not been elucidated so far.

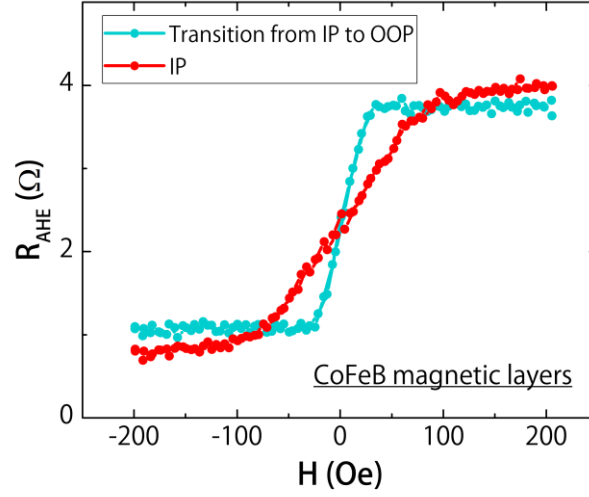


Fig. 2. 6 Transition from in-plane to out-of-plane anisotropy in CoFeB films.

Next, we did an anisotropic magnetoresistance (AMR) measurement where I fixed the external field at 2000 Oe and scanned the field in the horizontal plane. Due to the external field dragging down the magnetization to be almost in-plane, the AMR signal which is related to the angle between the direction of magnetization and the measurement current varies as the field scan angle is swept from 0 to 2π . We see a shift of the AMR curve relative to the zero angle, as shown by Fig. 2.7. This is indicative of a tilted magnetization that has an in-plane component at some angle from either along or perpendicular to the Hall bar direction. This is likely due to the tilted direction of the Tb target during the sputtering, following the analysis from Ref. 7. These measurements confirmed the tilted anisotropy of the bulk TbCoFe, and indicated that the magnetization of this material is relatively sensitive to the growth condition.

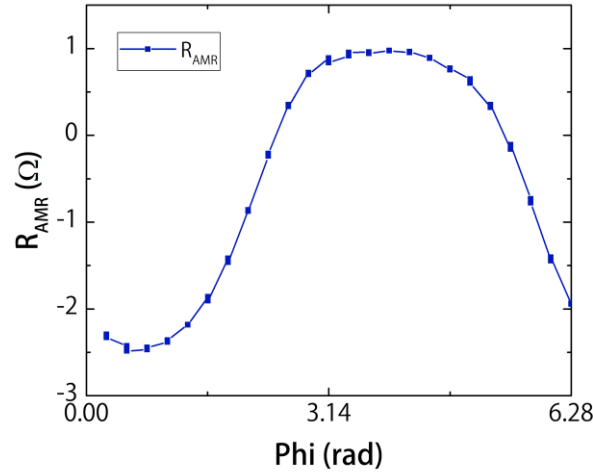


Fig. 2. 7 AMR measurements with a fixed field scanning 360° in plane on TbCoFe tilted samples

For memory applications requiring a high TMR in the MTJs, people first started using Al_2O_3 and in the more recent years MgO as the tunnel barrier due to their high spin injection efficiency. Amorphous CoFeB is widely used as the electrode material due to its high spin polarization of the electrons at the Fermi surface. With a high TMR of even $> 1000\%$ achieved in $\text{CoFeB}/\text{MgO}/\text{CoFeB}$ systems, low TMR has become an obstacle for other materials to be used in MTJ structures, even though they may have advantages in other properties. However, for TbCoFe , it is shown that with another oxide material Pr_6O_{11} , one can achieve high efficiency tunneling with $\text{TMR} > 200\%$ at liquid nitrogen temperature⁵¹. This can potentially enable further research in utilizing this bulk PMA material in non-volatile memory applications⁵².

2.2 Current induced switching in antiferromagnet PtMn

For a long time after antiferromagnetism was discovered, people have thought

that it was useless due to its zero net magnetization. However, in the 1990s people successfully discovered and utilized the strong exchange bias of antiferromagnetic (AFM) material in hard disk recording heads where an AFM layer is used to pin an adjacent ferromagnetic (FM) layer. More recently the emergence of spintronics opened a new way of looking at spins in various materials. While below the Neel temperature, AFM materials show zero net magnetization, the orientations of the spins in each sub-lattice can still carry useful information, which, due to the zero net moment, gives an extra advantage of high security over the general ferromagnetic storage. People have developed ways to image AFMs and to read AFMs electrically, and to further manipulate AFM's orientation including utilizing materials that have a net uncompensated moment in each sub-lattice, which gives a small net magnetization. Another interesting feature of the AFMs is the interface. Depending on specific materials, the compensated, or uncompensated interface in contact with another FM layer can lead to various novel and useful phenomena⁵³.

More recently, people have discovered that strong spin orbit coupling exists in some AFMs, some even comparable to many heavy metals^{16,54–58}. We systematically studied the spin Hall effect in several PtMn/FM systems including stack order of the layers, adding a spacer layer to remove the spin memory loss at the PtMn/FM interface, etc. We obtained the strongest spin torque efficiency of 0.24 in a Ta(1.5)-PtMn(8)-Hf(0.25)-FeCoB(0.8)-MgO(1.6)-Ta(1.5) system¹⁵. We also obtained a bulk spin diffusion length of 2.3 nm in PtMn and a spin conductance of $G_{PtMn} = 1 / (\lambda_s^{PtMn} \cdot \rho_{PtMn}) = 0.37 \times 10^{15} \Omega^{-1} m^{-2}$. The high spin torque efficiency and low spin conductance show a great promise in future application of this AFM in spintronic

devices.

To further validate the results we got from the spin torque measurements as well as to show the feasibility of utilizing PtMn in future storage devices, we carried out a series of switching experiments on various stack structures using PtMn as the spin source material. We first grew a sample with the stack A: Ta(1)-PtMn(4)-Hf(0.5)-FeCoB(wedge)-MgO-Ta(1.5). The wedged FeCoB was thin enough to yield PMA in the Hall bar structure. The 0.5 nm Hf insertion was used to suppress the spin memory loss at the PtMn/FeCoB interface as well as to enhance the PMA of the system as indicated by Nguyen et al.⁵⁹ Figure 2.8 shows the external field scan across the Hall bars in the out-of-plane direction. As shown by the comparison between this sample and another control sample B: Ta(1.5)-PtMn(8)-FeCoB(wedge)-MgO-Ta(1.5) at the same FeCoB thickness, coercive field of the device is significantly enhanced with the Hf spacer layer, indicating much stronger PMA.

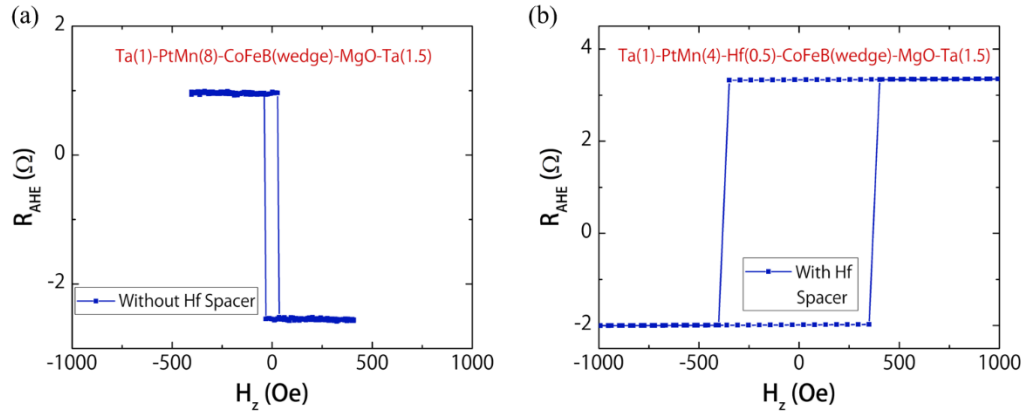


Fig. 2. 8 Comparison between PtMn-FeCoB PMA structures with and without a Hf Spacer. Anomalous Hall loops with out-of-plane field scan.

We further characterized the magnetic field response of this device with

external field scanning in the in-plane (hard axis) directions. Figure 2.9 shows the anomalous Hall response with the external field scanned in the in-plane x and y directions, respectively. Due to the strong PMA, even with a 3000 Oe in-plane field applied, the magnetization is still pointed largely out of plane, giving a significant anomalous Hall signal, which is proportional to the perpendicular magnetization. As the applied field decreases, the magnetization relaxes to the original upward (downward) direction and reaches the maximum value at the center of the loop, which corresponds to the results shown by Fig. 2.8(b). We observed switching in both x and y field sweeps with different hysteresis widths, which is not predicted by the ideal coherent rotation of macrospin model. While this could be related to the large domain structures with thermal fluctuation, it could also be due to the imperfection of the applied field having out-of-plane component, which, as the magnetization gets closer to in-plane direction, helps to switch it across the horizontal plane, thus allowing it to relax to the opposite state.

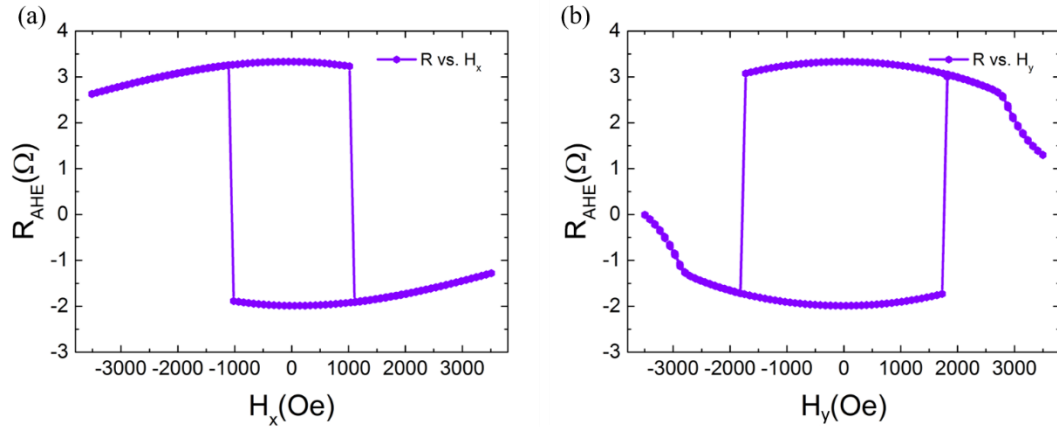


Fig. 2. 9 Anomalous Hall response of sample A with external field scanned in hard axis directions (x and y directions)

Next, we show current induced switching in our PtMn samples with an in-plane bias field applied along the direction of the current. The measurement scheme is shown in Fig. 2.10(a). DC current is applied in the y direction and an in-plane field of 200 Oe is applied in the same direction. We observe clean, abrupt switching of the magnetization deterministically between up and down with $I_c \sim 3.5$ mA, shown in Fig. 2.10(b). Our switching shows that, consistent with the spin torque measurement, the antiferromagnet PtMn exerts a sizable spin torque on the adjacent FM, which resulted in the reversal of its magnetization. Note that in these types of the devices an in-plane field is needed to break the symmetry and induce deterministic switching. In the large Hall bar structures with a size of $60 \mu\text{m} \times 5 \mu\text{m}$, the switching is usually not driven by coherent rotation of the moment, but rather by domain nucleation and expansion as shown by previous works^{60,61}. In this latter case the spin-polarized current diffuses into the FM, it nucleates a domain at a random spot (or at a preferred site by special engineering, which will be described later in this section). If no external field is applied, the domain wall which exists between the nucleated region and the rest of the film will only move under the applied spin current, which will not result in deterministic switching. However, when an external field is applied and is large enough to break the chirality dictated by Dzyaloshinskii-Moriya interaction and align the magnetization in the domain wall in the same direction, the out-of-plane effective field generated by the spin current can switch the magnetization up/down depending on the polarity of the injected spins. As the electric current is swept, the fast domain propagation follows the initial nucleation and finally results in the full switching of the magnet. In recent years people have developed various different ways to achieve

“field-free” switching in PMA systems using different concepts to replace the applied in-plane field^{16,33–35,38,40}, although none of them has proved highly reproducible for application so far.

In the meantime, there are also works that focus on manipulating the switching dynamics under the domain nucleation and propagation picture^{39,46}. For example, Safeer et al. introduced different shapes of the nanomagnet and underlying channel to achieve unidirectional switching at the time scale of 100 ps with an estimated domain wall velocity of ~ 400 m/s (Fig. 2.11). The origin of the switching comes from the specific combination of the magnetization direction caused by the shape of the nanomagnet and the spin polarization direction and distribution dictated by the shape of the channel. Similar to the explanation in Fig. 2.10(c), the two features mentioned above determine whether and in what direction the domain propagates, which follows the initial domain nucleation due to the short pulse heating on the tips of the nanomagnet.

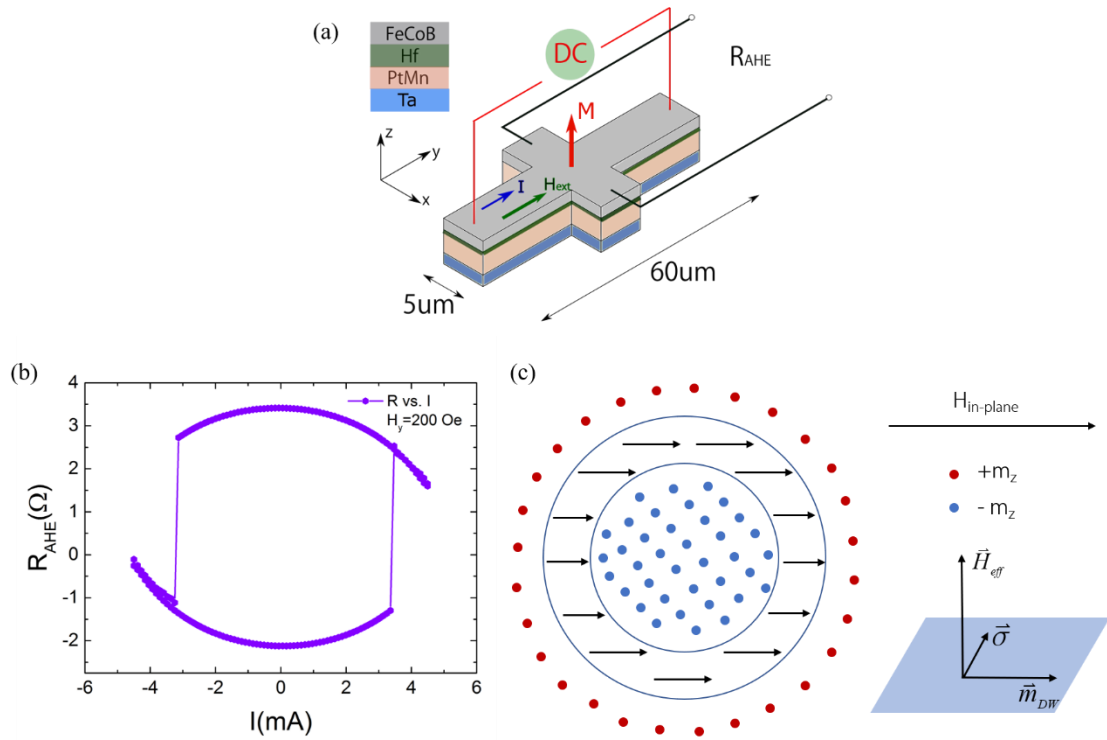


Fig. 2. 10 Current induced switching in PtMn samples with an in-plane field applied along the current direction, as explained by domain nucleation and propagation model.

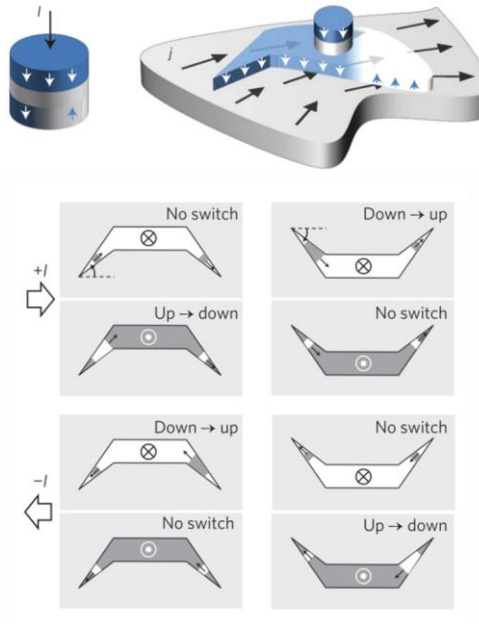


Fig. 2. 11 Unidirectional switching of specially shaped nanodots. (Reproduced from Safeer et al.⁴⁶)

Since most of the nanostructure systems people study are beyond the validity of the single domain model, understanding domain dynamics is crucial to the understanding of various switching behaviors. To date there are many developed ways of directly detecting the switching of multi-domain structures including scanning transmission X-ray microscopy⁶², differential Kerr microscopy⁴⁶, NV-spin⁶³, etc. These imaging methods can provide useful guidance for manipulation of the domain structures, leading to various future applications that rely on the understanding of domain dynamics, including domain-wall logics^{64–66}, fast SOT switching devices^{14,31,67,68} and racetrack memory^{69,70}.

Finally, we carried out current induced switching experiments on our PtMn samples with various applied fields. Figure 2.12 shows the resultant switching phase diagram. Before each switching attempt, we saturated the magnetization to the initial state with large out-of-plane field. This was to clean up the residual magnetic domain configuration caused by previous (current switching) measurement which may result in partial switching or reduced switching current due to part of the sample not in the ideal initial state to start with. On the phase diagram, the inner region is the bi-stable state of the magnetization while the data points indicate switching current at certain applied in-plane field for a particular switching polarity. As the applied field is larger, the switching current decreases slightly due to the larger effective spin Hall field generated by the current. Our switching phase diagram showed similar behavior to previously reported samples under the domain nucleation and propagation picture^{60,71,72}.

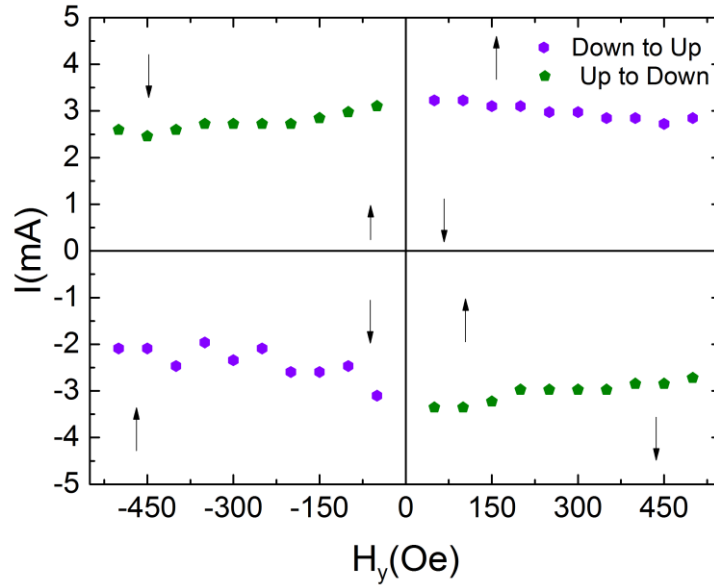


Fig. 2. 12 Current switching phase diagram of a PtMn sample.

In conclusion, in this chapter I have shown magnetic and current induced switching of PMA devices, which is the main focus of today's industrial MRAM research due to their better scalability. PMA devices can potentially switch faster, although an in-plane bias field is required to break the symmetry and give deterministic switching. Various methods and results have been published so far to eliminate the requirement of this field, although more reproducible results are still needed. While in-plane magnetized MTJs switched by spin orbit torque have been reported to generate low power, high speed switching (Chapter 5), there is still wide interest and great promise in the area of PMA studies to achieve reliable field-free switching, particularly if the switching current can be further decreased.

CHAPTER 3

FABRICATION OF THREE TERMINAL MAGNETIC TUNNEL JUNCTIONS

In this chapter I will introduce the fabrication procedures we used in patterning our three terminal MTJ structures. I will cover the step-by-step procedures with details of resist stack, machine operation, as well as points we need to pay special attention to.

3.1. Film growth

Except for the collaboration with Canon Anelva, who grew IrMn pinned-, SAF balanced-MTJ stacks for us, we sputtered simplified MTJ stacks in our magnetron sputtering tool, AJA ATC2200. We sputtered most of the materials from 2-inch targets with an Argon flow of 8 sccm and a pressure of 2 mTorr. Except for alloying, the power of the sputter gun is set at 30 W. When the target was in gun 7, where the wafer – target distance is closer, a higher pressure (≥ 3.5 mTorr) is usually needed to ignite the gun. MgO was sputtered from a single target with RF power of 100 W. Careful checking of the rotation of the wafer holder, ignition of the gun, and the opening of gun shutters was needed during the whole sputtering procedure to make sure every part works normally.

For the purpose of successful fabrication, a full 4-inch substrate was required for the sputter deposition and we must avoid small cracks caused by the sample clips directly pressing on the substrate that may evolve into big ones or even cause the wafer to break during sonication in later steps.

3.2 Fabrication procedures

The fabrication of three terminal MTJs mainly consists of five steps, which is depicted in Fig. 3.1.

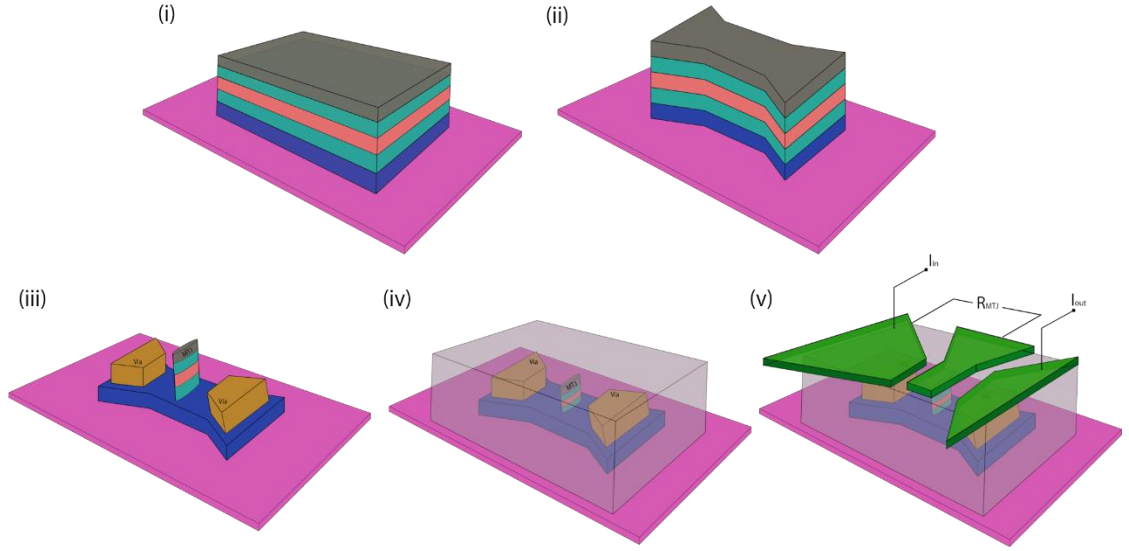


Fig. 3. 1 Fabrication flow of three terminal MTJs

3.2.1 Alignment marks

The MTJ fabrication starts with the creation of the alignment marks that will be used in all the subsequent steps to align different features. The alignment marks include 12 ASML marks (four on each side) for the deep UV lithography, 12 global marks (four on each side) for E-beam wafer alignment and 3 sets of chip marks within each die for E-beam exposure. The detailed locations and sizes are labeled in Fig. 3.2. In a successful fabrication, only 2 ASML marks, 2 E-beam global marks and 1 set of E-beam chip marks are used in alignment. Other marks serve as back-ups when primary marks are damaged or lost due to unexpected incidents.

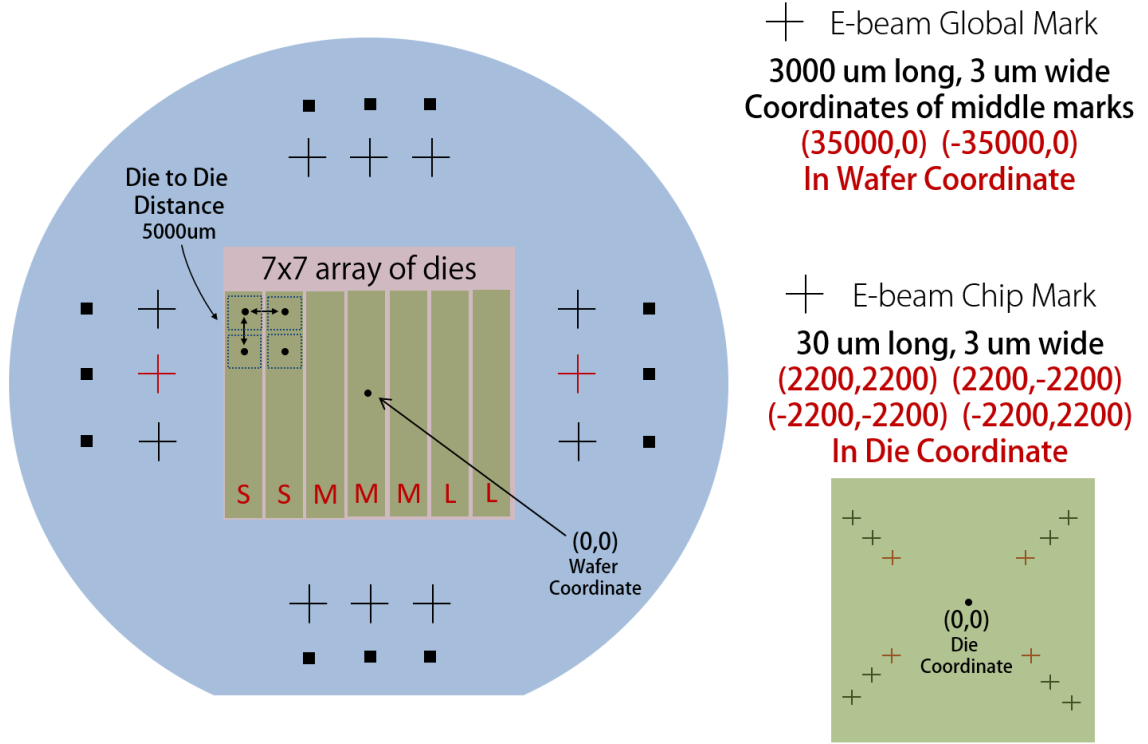


Fig. 3. 2 Sizes and locations of alignment marks for MTJ fabrication

There are two ways of creating alignment marks. One way is to lithographically define them together with the spin Hall channel (see step ii), which gives the benefit of saving time and less systematic shift of the features because of the removal of this extra step. However, the exposed/etched marks have poor contrast under SEM of the E-beam tool, causing the difficulty of finding/scanning the marks during E-beam exposures, which can significantly reduce the yield of the fabrication.

Here we introduce the other way of depositing alignment marks at the beginning of the fabrication procedure. After the sample is grown in the AJA, we use an ASML tool (PAS 5500/300C DUV Stepper) to define the marks. Images containing various marks are written on the ASML reticle (mask), which was designed in our lab and made by Photronics Inc. to achieve minimum feature size of 0.68 μm on the

reticle. We use bi-layer resist of DSK-101-4 and UV-210-0.3 and a low dose of 20 $\mu\text{C}/\text{cm}^2$ to expose the marks (see Table 3.1 for details of resist spinning and baking protocols). After the exposure, a post-exposure bake at 135 °C for 90 seconds is needed before we develop the wafer in the Hamatech-Steag wafer processor using a program 726MIF 150SEC. Next, we put the developed wafer into an AJA sputter system and deposit a bi-layer of Ti-Pt contact onto our film. The thickness of the layers is roughly 10 nm for Ti and 50 nm for Pt. The choice of the materials and thicknesses is such that there is enough height difference for photo mark detection and good contrast for SEM mark detection. We do a quick lift-off of the resist for 2 hours using Remover PG (MicroChem) with a solution temperature of 110 °C. After the temperature goes down to room temperature, we sonicate the wafer in Remover PG for approximately 30 minutes and transfer it to Acetone for another 30-minute sonication. Then we clean the wafer with isopropyl alcohol (IPA) and blow dry with pure nitrogen. Finally, we do a quick development in Hamatech using program 726MIF 60SEC to clean the residual DSK layer that is not completely removed by Remover PG. After this step there will be only sputtered marks on the full film stack which are visible to the eyes due to their relatively large sizes (micron-size) and the rest of the region of the wafer should look shiny and clean with only the sputtered magnetic film stack.

Resist	Spin Condition	Bake Condition
DSK 101-4	2500 rpm, 60 seconds	175 °C, 75 seconds
UV 210-0.3	2500 rpm, 60 seconds	135 °C, 60 seconds
Post-exposure Bake: 135 °C, 90 seconds		

Table 3. 1 ASML resist stack with spinning and baking protocols

3.2.2 Spin Hall channel

The second step is defining and etching the spin Hall channels. With sputtered alignment marks, we use the same resist stack and same ASML procedure to expose and develop spin Hall channels. The dose is in the range of $20 - 30 \mu\text{C}/\text{cm}^2$ depending on the size of the channels and detailed dose test results. We then put the wafer in our ion beam etching (IBE) system (IntlVac NanoQuest I) to etch away materials in the non-channel region. The IBE system has a 12-cm DC Kaufman source (corresponding controller KSC1206) with a source – wafer distance of 6.65''. A set of typical etching parameters is shown in Fig. 3.3. We put thermal paste on the backside of the wafer to enhance the heat conduction between the wafer and the water-cooled stage. A glass etch mask with a square whole of $5 \text{ cm} \times 5 \text{ cm}$ is put on top of the wafer to restrict the etching area so that the material stack covered by the etch mask is preserved for FMR measurement afterwards. There are two etching steps involved in this channel etching procedure. First, we set the angle of the stage to 165° (15° from normal incident) to do the main etching. To reduce the heating of the wafer, which leads to difficulty in

removing the resist in the subsequent step, we put the wafer on a copper plate attached to the stage to enhance heat conduction. Moreover, we set up a shutter cycle program that controls the shutter on/off with preset time delays to avoid continuous ion beam bombardment of the resist. A working recipe is 5 seconds of etching (shutter open) followed by 10 seconds of cooling (shutter closed). The wafer stage is rotated uniformly during etching. We use a SIMS detector and software package (MASSoft) to monitor the progress of the etching where the peak of an element showing up indicates complete etch-away of this material at the center of the wafer. Due to the uniformity of the ion beam, there is an observable effect that the center of the wafer is more heavily etched than edge of the wafer, so we restrict the size of the active device region to within $\sim 5 \text{ cm} \times 5 \text{ cm}$ to reduce variation of the device behavior due to non-ideal etching. At this step we usually stop the (close to) normal incident etching when we reach the MgO layer. The choice of stopping at MgO layer is, 1) Mg typically has a large signal so it is easy to observe, 2) Due to another etching procedure that will be described in Fig. 3.1(iii) which also etches material in the non-channel region, we do not need to etch away everything in this step. The remaining materials will be etched away concurrently with the etching of the MTJ pillar in step iii. When we finish this first etching step, we change the stage angle to 110° to do a sidewall etch to clean up the re-deposited material during the first step etching, and to create a better profile on the edges of the channels. This step is usually a 10-second etch, repeated for four times (together 40 seconds).



Fig. 3. 3 Ion source parameters for etching the spin Hall channels

After the etching is done, we strip off the resist by heating the wafer in Remover PG at 130 °C for 6 hours. The same sonication procedure in Remover PG and Acetone is applied at the end of this step, as well as the Hamatech clean-up procedure (726MIF 60SEC). To check the results of the channel definition, we use AFM (Veeco Icon) to measure the size and profile of the channel. Fig. 3.4 shows an example of a 300-nm wide channel whose actual width is measured to be around 290 nm.

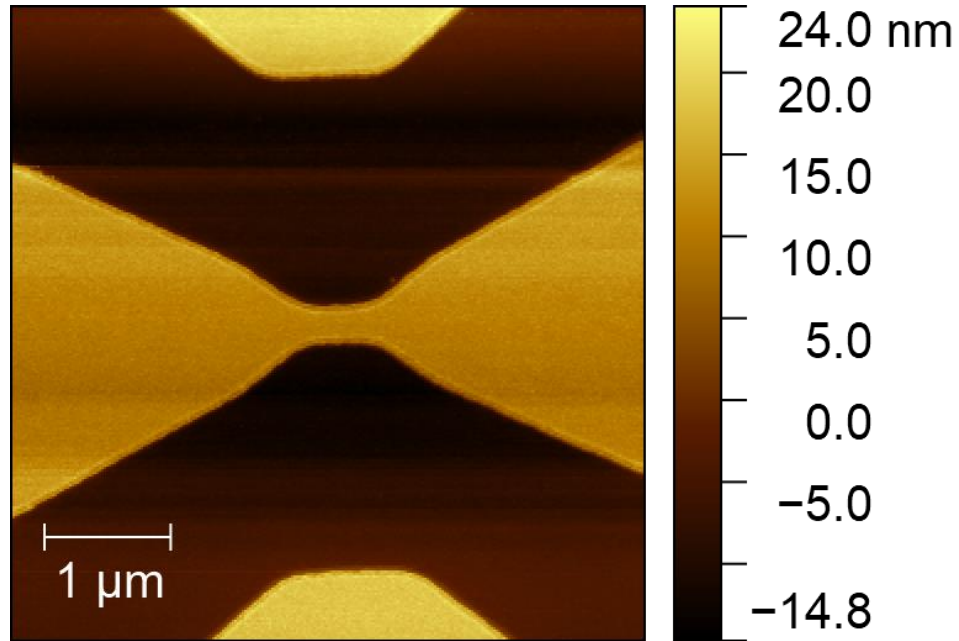


Fig. 3. 4 An AFM image of a completed spin Hall channel with a nominal width of 300 nm and measured width of 290 nm.

In the rare cases where the resist has gone bad, or where significant heating during the IBE causes the hardening of the resist, we could see a thin “fence” (resist residue) of usually a few nanometers wide along the edge of the channel, which is shown in Fig. 3.5. In this case repeated Remover PG heating at elevated temperatures and longer time may help to reduce the fencing but typically cannot fully get rid of the resist junk left on the channel.

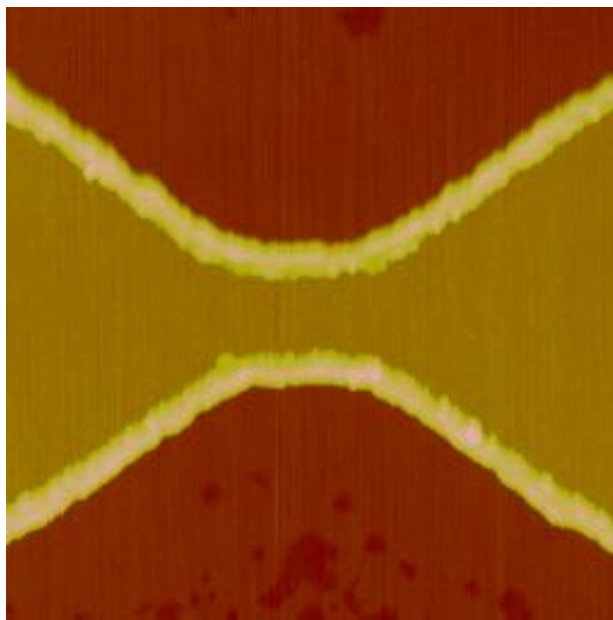


Fig. 3. 5 An AFM image showing a failed spin Hall channel with "fence" on the edge of the channel

As mentioned earlier, we can combine the first step of alignment mark definition and deposition into this step. To do that, we add the alignment mark images from the ASML reticle to the job file and expose the marks at the same time as the channels. The marks will be etched down together with the channels, so instead of having the marks on top of the magnetic layers this alternative procedure creates marks by having the dip into the magnetic layers.

3.2.3 MTJ pillar and contact vias

After the channels are made, we proceed to making MTJ pillars, and micron-size vias that serve as the contact from the top to the bottom channel. In order to achieve small size (< 100 nm laterally) and various shapes, we use E-beam lithography (JEOL JBX-6300FS) to write these features on the channel. We use a tri-

layer resist stack of OmniCoat/PMMA/HSQ as a writing mask. The details of the resist spinning procedures and thermal treatment are listed in Table 3.2.

Resist	Spin Condition	Bake Condition
OmniCoat	3000 rpm, 60 seconds	170 °C, 1 minute
PMMA 495k 4%	3000 rpm, 90 seconds	170 °C, 5 minutes
HSQ 6%	3000 rpm, 60 seconds	170 °C, 1 minute

Table 3. 2 E-beam resist stack with spinning and baking protocols

We use the 4th lens mode of the tool which has a maximum field size of 500 μm and a minimum pixel size of 1 nm. Design file was prepared using the KLayout software and is converted to JEOL v30 file using LayoutBeamer software. In the E-beam job file we define the location of to-be-exposed dies, the type of MTJ pillar to be written and corresponding doses. An example of a job file is shown in Fig. 3.6. During the exposure, two large micron-size vias are exposed concurrently with the MTJ pillar. These two vias are placed on each side of the MTJ with a separation of $\geq 4 \mu\text{m}$ from each other. These vias serve as electrical connection between the spin Hall channel and the top contact, which will be described in the next step. After the fabrication, only the top layer can be accessed by measurement probes, so to apply current in the spin Hall channel, we need good conduction from the top contact to the bottom. Due to the large area, the resistance of these vias is negligible compared to the MTJ or the channel, although current shunting due to spreading resistance could potentially play a

Time	1 min 30 sec	O₂ gas flow	20 sccm
Forward Power	100 W	Pressure	50 mTorr

Table 3. 3 Parameters for oxygen plasma etch of PMMA/OmniCoat resist stack

When these steps are finished, we are left with a full tri-layer resist stack covering the MTJ pillar and via regions. We then do an IBE in our etching system with same parameter as in the channel etching step. The same thermal paste and the etch mask method is applied. However, we need to be very careful about the stopping of the etching in this step. We need to stop the etching before the ion beam starts hitting the channel material to avoid dramatic increase in channel resistance, which will make the measurement of the devices very difficult or even impossible under short voltage pulses. On the other hand, we need to etch deep into the free FeCoB layer to get a good profile of the MTJ pillar to achieve high shape anisotropy, which is a critical property of the devices. Therefore, etch stop is very crucial in this step. Usually one more cycle of etching after the signal of the channel material starts to rise is a good timing to stop. We also do a sidewall clean after the main etch to remove the re-deposited materials that might short the tunnel barrier.

After the IBE we do a re-fill of an insulating material (SiO₂ or Si₃N₄) to protect the MTJ pillars and to electrically isolate them from other regions. We use an e-gun evaporator (CVC SC4500) to deposit around 60 - 70 nm of the insulating material. The choice of using an evaporator is due to the ease in lifting up the resist in the subsequent step while other deposition methods give a capping profile of the

insulating film over the MTJ pillar/resist, which causes difficulty for the lift-off chemical to get into contact with the resist. After the evaporation is done, we do a similar lift-off step of heating the wafer in Remover PG at 130 °C for 6 hours, followed by the same sonication protocols. After this step, MTJ pillars are formed and protected by the evaporated insulation. With a successful lift-off there should be holes opened up on top of the pillar and via regions, ready for deposition of the contact materials. An AFM image revealing these features is shown in Fig. 3.7. Note that the sizes of the holes do not necessarily match the designed size of the MTJ (via) due to imperfect lift-off and limitation of imaging resolution that does not accurately measure the width and the depth of a nanometer size dip. Since we only need electric contact from the top to the bottom, as long as we see sizable holes (sometimes even a slip, when designed features are small) it will be good for continuation to the next step.

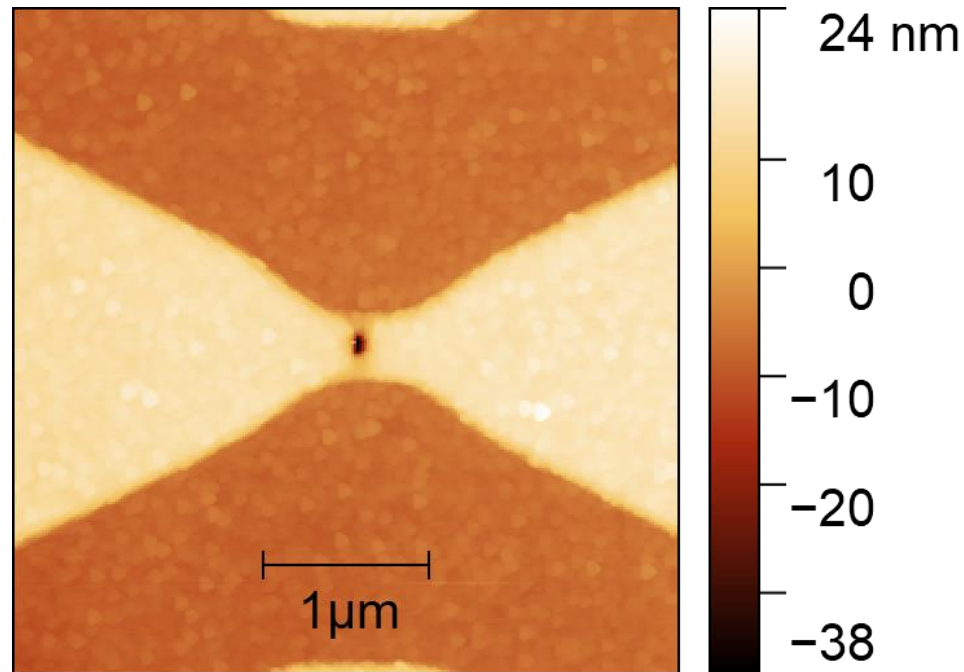


Fig. 3. 7 An AFM image showing a successfully lift-off of E-beam resist, which exposes a hole on top of the MTJ pillar for subsequent top contact deposition

3.2.4 Top contact

In this step we define and create top contact layers by ASML and AJA sputter tools. Once the holes are opened up, we do an ASML step and expose the designed shape of contact pads on the wafer. All the resist spinning, baking and developing protocols are identical to previous steps with ASML. We use a low dose of $22 \mu\text{C}/\text{cm}^2$ since the feature size in this step is large. After the development of the contact pads, we use the AJA sputtering tool to deposit Ti 10 nm/Pt 50 nm as the top contact. Finally, a lift-off procedure identical to the one used in the alignment mark step is carried out to clean up the wafer, which finishes the whole fabrication of the MTJ wafer. A completed device is exemplified in Fig. 3.8.

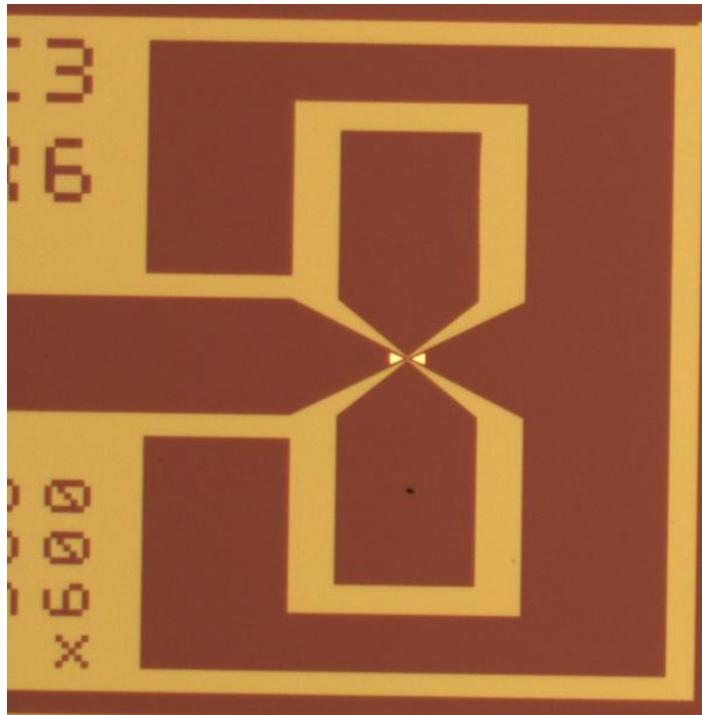


Fig. 3. 8 A microscopic image showing a completed MTJ device. The two bright triangles are two contact vias.

3.2.5 Miscellaneous procedures

When the fabrication is finished, an optional clean-up of the DSK101-4 using 726MIF 60SEC on the Hamatech is usually carried out. We dice the wafer into small chips or rows in order to apply different annealing schemes or other treatment. We spin a thin layer of S1813 resist on the wafer and use Disco DAD3240 to achieve the high precision dicing. Thermal annealing of various temperatures is applied on diced chips/rows using an air convection furnace (Vulcan 3-1750A). Vacuum annealing (Lindberg General Signal tube furnace) is also used in some cases to avoid oxidation of the chips at high temperatures.

CHAPTER 4

CONSTRUCTION OF A HIGH FREQUENCY SETUP FOR PULSE MEASUREMENT OF MTJS

In this chapter I will introduce an advanced measurement technique for fast pulse switching experiments. An NI-DAQ based high frequency hardware system is programmed to do automatic injection of pulse voltage, MTJ resistance detection and calculation of the switching probability/write error rate after the data acquisition.

4.1. General MTJ measurement technique

In a three terminal MTJ design, the resistance of the MTJ is measured from the top terminal and either one of the bottom terminals while the switching current (pulse) is sent to the spin Hall channel using the two bottom terminals (Fig. 4.1).

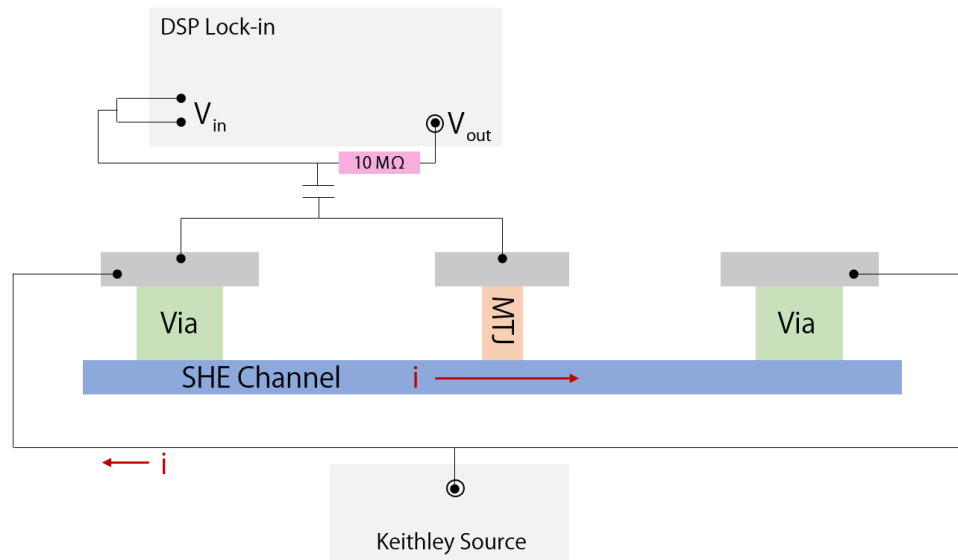


Fig. 4. 1 A schematic picture of general MTJ measurement method

To measure the MTJ resistance, we use a lock-in amplifier (Signal Recovery

DSP 7265) and connect its output to the top and bottom terminals. A resistor of 10 M Ω is inserted in series in the line to share part of the voltage drop from the output so the input channels of the lock-in measure the voltage drop on the MTJ device. A 100 μ F capacitor is inserted in series to screen out any possible large DC spikes that may cause damage to the MTJ device.

To apply switching current to the spin Hall channel, we connect the output of a Keithley 2450 current source to an RF probe that will touch down on the bottom terminals of the MTJ device. When we do pulse measurements, we output switching pulses and resetting pulses from two pulse generators and combine the two lines using a power divider. The power divider has a 6 dB attenuation of the pulse amplitude, which is accounted for in all the data processing.

4.2 NI-DAQ based high-speed pulse measurement technique

To study the switching behavior at nanosecond time scales, we use signal pulse generators (Picosecond Pulse Labs PSPL10100 and 10070A) to send short voltage pulses of various pulse amplitudes and durations to the spin Hall channel. The conventional measurement method consists of four steps for each switching attempts. First, the computer sends a command to the pulse generator through the GPIB and the pulse generator emits a voltage pulse to the sample through the RF cable and probe, with a preset pulse amplitude and duration in the measurement program. Second, the lock-in amplifier reads the resistance of the MTJ and compares it to the value before the voltage pulse was sent to the device. It outputs a message of “switched” when the measured MTJ resistance crosses the middle resistance as defined by

$R_{middle} = \frac{1}{2} R_P + R_{AP}$, where R_P and R_{AP} are MTJ resistances at P and AP states,

respectively. After this step, a command is sent from the computer to the other pulse generator to apply a voltage pulse of relatively low amplitude, larger duration but opposite polarity to reset the MTJ to its original state. Finally, a similar reading method using the lock-in will determine whether the MTJ has been successfully reset. It will keep triggering the second pulse generator to send reset pulses until the measured MTJ resistance has returned to the original state. To get good statistics, for each combination of pulse amplitude and duration, 200 switching attempts are carried out and the switching probability is calculated based on the results from these switching attempts.

However, due to the low speed of lock-in measurement (time constant ≥ 50 ms) and frequent data transfer/communication between instruments and the PC, this type of measurement can be very slow and inefficient. It usually takes a few hours to do a set of pulse sweep measurement and due to the delicate nature of our research objects, MTJs, longer measurement time creates more risks to kill the devices by stray pulses. To resolve this issue, we tried to implement a new measurement system using a high speed, high buffer data acquisition card (DAQ) (NI-USB-6361) where we write instructions into the memory of the card and let the card trigger acquisition, store information and finally transfer the full pack of data to the PC.

The DAQ and the wiring diagram are shown in Fig. 4.2 and Fig. 4.3, respectively.

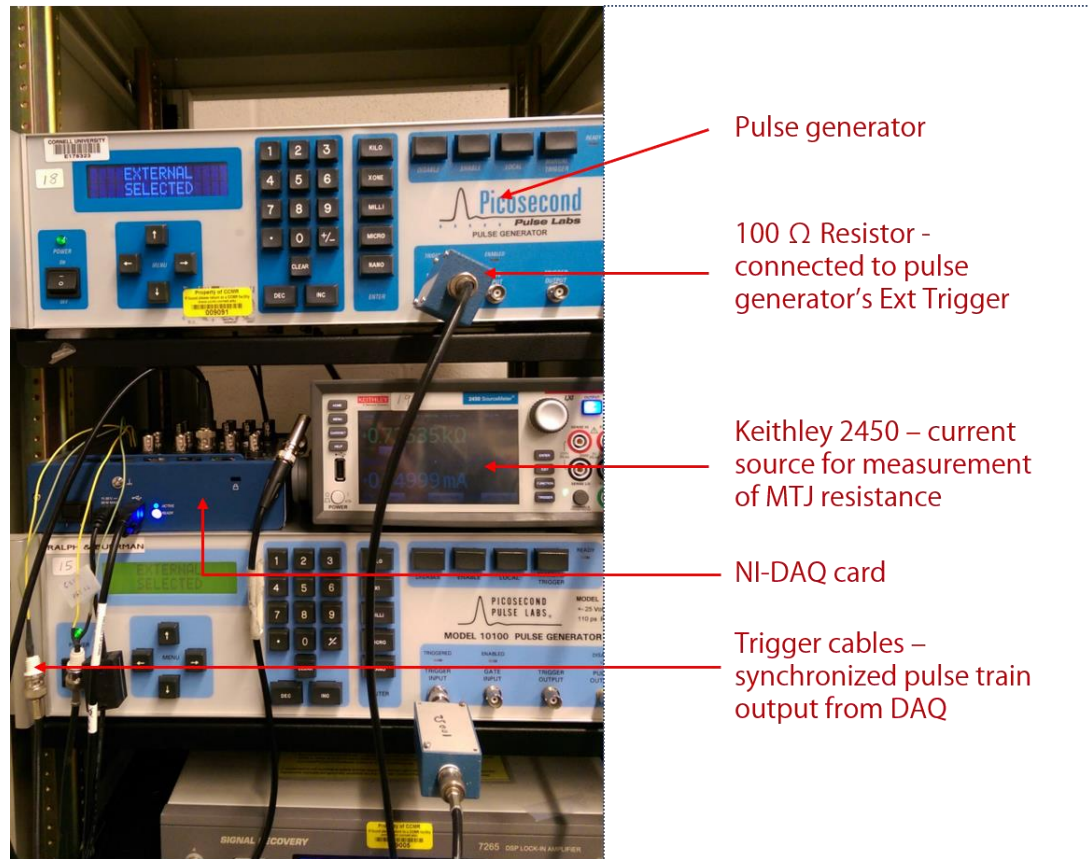


Fig. 4. 2 NI-DAQ card, ports and wires

The DAQ card is connected to the PC through a USB cable for data transfer. The port AI 1 is an analog input port, which is connected to a Tee adapter, one end of which is connected to a Keithley DC source and the other connected to the MTJ sample. The Keithley supplies a constant measurement current (usually 2~5 μA , depending on the resistance scale and TMR of the device) through the MTJ and the DAQ acquires the MTJ resistance by reading the voltage drop in this line. Three digital counters 0, 1 and 2 (PFI 12, PFI 13 and PFI 14) are used to trigger the switching pulse generator, the reset pulse generator and the reading (AI 1) from the DAQ. On the pulse generators, the ports Ext Trigger are connected to the digital counters (PFI 12 and PFI 13) of the DAQ, and are used to trigger output pulses when

receiving trigger signals from the DAQ. We set the trigger level to be 0.5 V, above which the output of preset pulse sequences is triggered. We need to wire in a $100\ \Omega$ resistor to each trigger line to reduce the voltage sent to the external trigger circuit of the pulse generator since the maximum it can take is 5 V and the output of digital counters from the DAQ is also 5 V. The other digital counter PFI 14 is set in the PC program to be internally connected to the AI 1 to trigger readings after each switching pulse and each reset pulse. The detailed wiring diagram is shown in Fig. 4.3.

Wiring Diagram

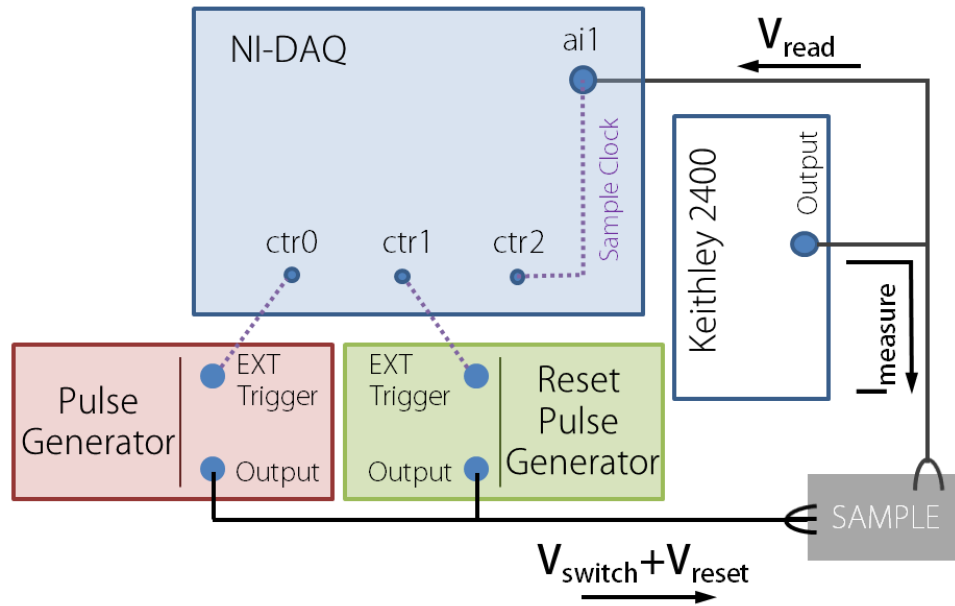


Fig. 4. 3 Wiring diagram for the fast pulse measurement setup

The detailed time sequence is shown in Fig. 4.4. The maximum measurement speed we can run with this system is at a 100 kHz repetition rate, which corresponds to $10\ \mu\text{s}$ between two consecutive pulse outputs. This is limited by the pulse generator's output capability. However, to ensure high precision reading especially in less than

optimal situations, we reduce the speed to 1 kHz, which is 1000 μ s for each switching cycle. The three pulse trains, switching, resetting and reading are synchronized at the beginning by default DAQ settings. As the DAQ program is initiated a set of 1000 reset pulses with appropriate polarity and long durations is sent to the device for a quick reset to the initial state defined in the measurement. Then a trigger pulse is sent to the switching pulse generator, which triggers the output of a switching pulse to the spin Hall channel. After 250 μ s a trigger pulse (internally wired) triggers the AI 1 of the DAQ to acquire a voltage reading of the MTJ. After another 250 μ s, a trigger pulse is sent to the reset pulse generator, which triggers the output of a reset pulse to the spin Hall channel. Finally, another trigger pulse triggers the reading of the MTJ after another 250 μ s, which finishes one cycle of the measurement. After repeating this procedure for a preset number of switching attempts, all the collected data, which is temporarily saved in the DAQ buffer, is transferred to the PC memory where the comparison calculation is carried out to determine switched/unswitched statuses. After calculation, switching probabilities are plotted with regard to pulse amplitude or pulse duration.

Although the reset pulse amplitude and duration are chosen to be sufficient to switch the MTJ to the initial state, there could still be occasional reset failures, which would give a false judgement of the switching since a failed reset will inevitably give a “switched” result in the next switching trial. To eliminate this potential issue, we add one step after transferring the data to the PC. We let the PC check the MTJ resistance (voltage) after the reset. If the MTJ resistance does not go back to the initial state as defined in the measurement, which indicates a reset failure, we pick out the next set of

data and discard it. By going through all the data pairs we make sure that all the results represent a correct initial state. Since for a particular combination of pulse amplitude and duration, the number of repeated trials is typically large (≥ 1000) to get a switching probability, removing a few sets of data points does not affect the nature of the statistical measurement.

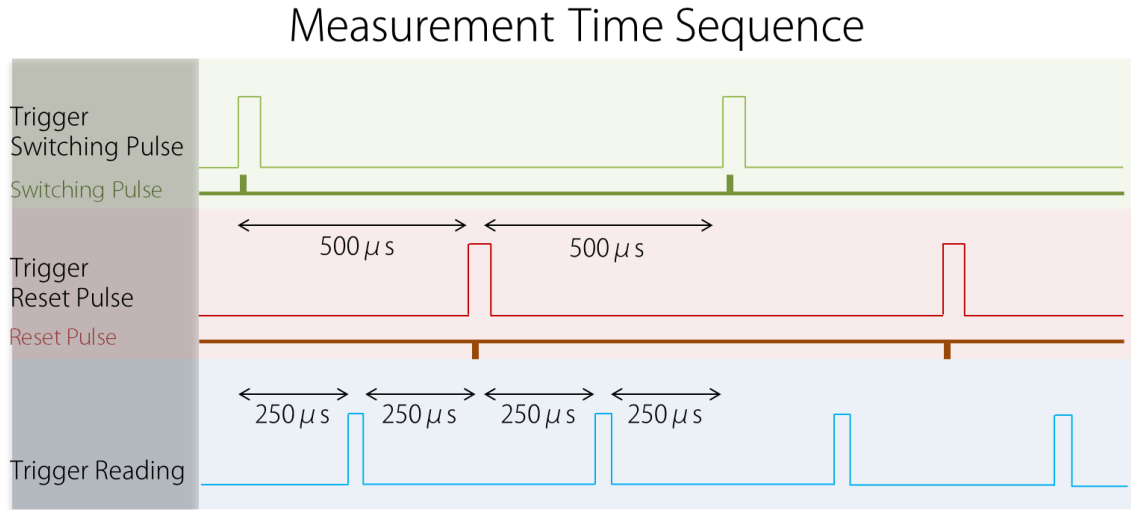


Fig. 4. 4 Time sequence of NI-DAQ based fast pulse measurement

To get the pulse switching phase diagrams that we are going to show in the next few chapters, we define a (typically) 50×50 grid where there are 50 increasing pulse amplitude values and 50 increasing pulse duration values. We carry out 1000 repeated trials using the method described above at each combination of amplitude and duration. We then construct the phase diagram using a color scale based on the switching probability calculated for each combination. The rise time of the pulse generator is 100 ps, which means that we cannot get to the set amplitude with a set pulse duration less than 100 ps. Moreover, at short pulse scheme (< 1 ns), due to the rise time and a long tail of the fall time, the actual duration when the pulse is at

maximum amplitude is shorter than the set value, but the overall effective time of the pulse is usually longer than nominal. Figure 4.5(a) shows a comparison of pulses at different set durations with an amplitude of 1 V (from PSPL 10100 model), as measured by the LeCroy SDA11000 signal analyzer. On the contrary, the pulse shapes from PSPL model 10070A shows a better rise time as well as a quick tail (Fig. 4.5(b)).

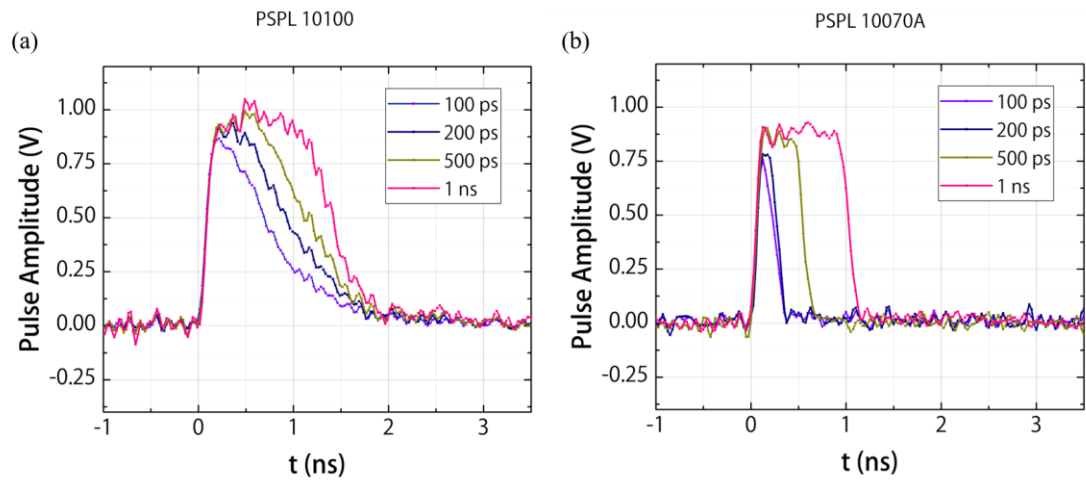


Fig. 4. 5 Pulse shape of a 1 V pulse at different durations from two pulse generator models 10100 and 10070A

CHAPTER 5

ACHIEVING LOW SWITCHING CURRENT IN 3T-MTJS THROUGH MODIFICATION OF MAGNETIC INTERFACES

In this chapter I will discuss an efficient method for reducing critical switching current in 3T-MTJs using atomic Hf layers to modify the interfaces. By inducing higher interfacial PMA, the demagnetization field can be greatly reduced, which directly reduces the critical current. I can also tune the magnetic damping of the system by passivating the W/CoFeB interface with Hf to remove the spin memory loss. Together these modifications give significant amount of reduction in critical current that makes these structures very promising in future memory applications.

5.1. Enhancement of perpendicular magnetic anisotropy through an atomic layer of Hf at FeCoB/MgO interface

Ever since the emergence of the STT-MRAM technology that utilizes spin current to switch a magnetic storage layer, reducing the write current has been a major focus of research in order to be compatible with scaled CMOS transistors and to reduce the energy consumption to replace the existing DRAM/SRAM technologies^{43,73}. However, due to the nature of spin transfer torques, in an STT-MRAM structure the efforts to reduce the switching current usually bring concurrent drawbacks in other aspects of the devices that make these approaches less effective. For example, people realized that the large demagnetization field of the MTJ free layer (FL) dominates the switching mechanism so reducing the M_{eff} can lead to smaller switching current. Various solutions have been proposed and tested including reducing

the FL thickness, using a different magnetic material that has smaller magnetization, and trying to create PMA using extra layers^{30,74–77}. However, since I_{c0} is directly related to $M_s \cdot H_k$ which contributes the thermal stability factor Δ of the device, a large reduction of the H_k will lead to significant reduction of the Δ , making the devices less stable for reliable data retention. If other materials than FeCoB are used as electrodes, we will suffer from reduced TMR, which will make reading of the switching difficult, especially in very fast operations intended for competing with the SRAM technology. Furthermore, making the thickness of the magnetic layer too small may result in exotic switching dynamics in the FL, which could possibly result in oscillatory switching or write error rate ballooning observed in some structures^{78,79}. 3T-MTJ designs have the advantage of separate read and write paths, which enables us to engineer different aspects of the magnetic structure independent of each other. In the context of current induced switching, both the demagnetization field M_{eff} determined mainly by the thickness of the ferromagnetic layer and any interfacial anisotropy energy density, and the uniaxial shape anisotropy H_c defined by the MTJ pillar geometry contribute to the critical current density as shown by eqn. (5.1)^{21,80}

$$J_{c0} = \frac{2e}{\hbar} \mu_0 M_s t_{FM} \alpha (H_c + M_{eff} / 2) / \xi_{DL} \quad (5.3)$$

where e is the electron charge, \hbar is the reduced Plank constant, μ_0 is the permeability of free space, M_s is the saturation magnetization of the FL and t_{FM} is the FL's effective magnetic thickness, $M_{eff} \equiv M_s - K_s/t_{FM}$ is the FL's effective demagnetization field, where K_s is the interfacial perpendicular magnetic anisotropy (PMA) energy density, and α is the effective magnetic damping constant of the FL. Note that H_c here is the

coercive field determined by the shape anisotropy of the elongated nanopillar, which can be larger than the apparent coercive field measured by magnetic field switching. In a typical material system with FeCoB-MgO-FeCoB structures, M_{eff} can reach (or surpass) one Tesla, while H_c is to the maximum on the order of several hundred Oersted (with optimized ion beam etching that creates a sharp profile of the MTJ pillar). The thermal stability factor is given by

$$\Delta = \frac{1}{2} M_s V H_c / k_B T \quad (5.4)$$

where V is the volume of the magnetic layer, k_B is the Boltzmann constant and T is the working temperature. Comparing the magnitude of the M_{eff} and H_c , we see that reducing M_{eff} by an order of magnitude while a sizable H_c can effectively reduce the switching current while maintaining high Δ , given that M_{eff} is still much larger than H_c , keeping the FL magnetization in plane.

People have shown that in a heavy metal (HM)/FeCoB/MgO structure, PMA of various strengths can exist depending on the choice of HM and the interfaces^{81–84}. A widely employed picture to explain the interfacial PMA is the boron diffusion at the FeCoB/MgO interface, enhancing the Fe-O bonds that are crucial to this phenomenon. While Yang et al. pointed out that an optimum amount of Fe-O bonds is the key to strong interfacial PMA, we try to seek for a better interface to enhance PMA, thus reducing the M_{eff} of the FL^{81,85}.

We discovered the usefulness of the Hf layer inserted at FeCoB/MgO interface (hereafter called “Hf dusting”) through a separate experiment where we aimed at separating FM layer and MgO layer to study the field-like torque behavior at the

FM/MgO interface⁸⁶. When the Hf is inserted at the interface, the anisotropy field is greatly enhanced. Then we started to vary a series of parameters including the Hf dusting thickness, FM thickness and annealing temperatures to explore this interesting effect. We first grew a wedged sample, Ta(1)-W(4)-FeCoB(0.8)-Hf(wedge)-MgO-Ta(1.5) (numbers in parentheses represent thickness in nanometers), and looked at the anomalous Hall response of the magnetization when an out-of-plane easy axis field was applied in the $60 \times 5 \mu\text{m}^2$ Hall bar patterned by standard photo-lithography and ion beam etching. Figure 5.1 shows a comparison of hysteresis loops at different Hf dusting thicknesses. The increase of the out-of-plane coercive field with thicker Hf dusting layers indicates that the PMA increases as the thickness of the Hf dusting layer increases.

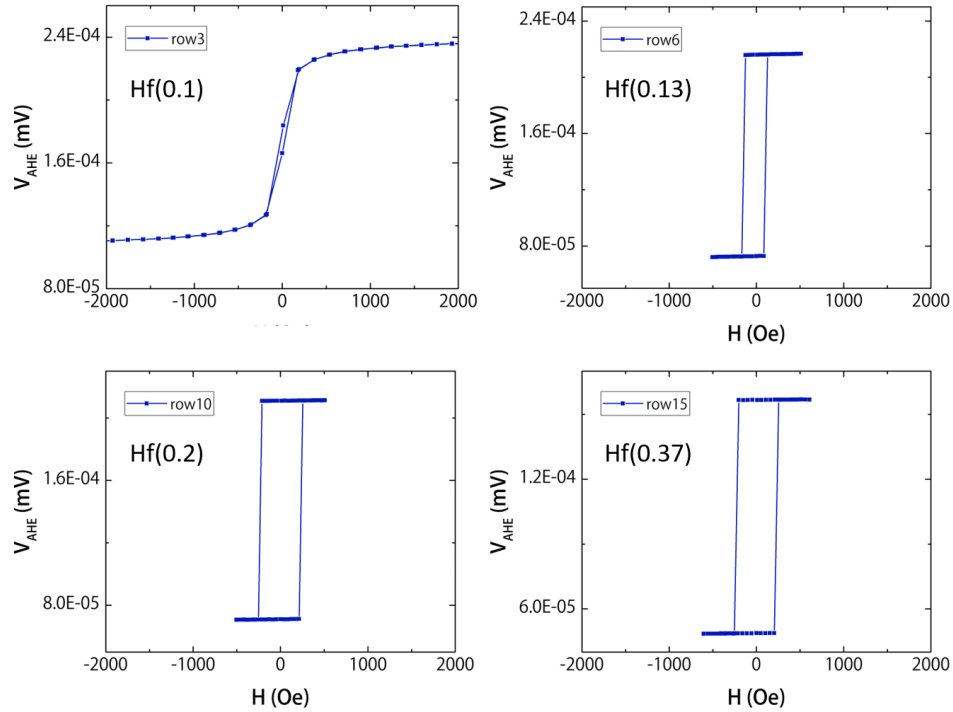


Fig. 5. 1 A comparison of anomalous Hall response of the structure Ta(1)-W(4)-FeCoB(0.8)-Hf(wedge)-MgO-Ta(1.5) with different Hf layer thicknesses

To characterize the anisotropy field of the Hf dusting structures, we fixed the Hf dusting thickness at 0.1 nm, i.e. less than an atomic monolayer, and grew a sample with a FeCoB wedge, namely W(4)-FeCoB(t)-Hf(0.1)-MgO-Ta with t being the thickness of the FeCoB. The Hall bars with the same $60 \times 5 \mu\text{m}^2$ size are annealed at 240 °C and 300 °C for 1 hour separately for study of the annealing temperature dependence. First we show the first harmonic response of the sample annealed at 300 °C when external field is swept in the easy axis direction (Fig. 5.2(a)) and hard axis direction (Fig. 5.2(b)).

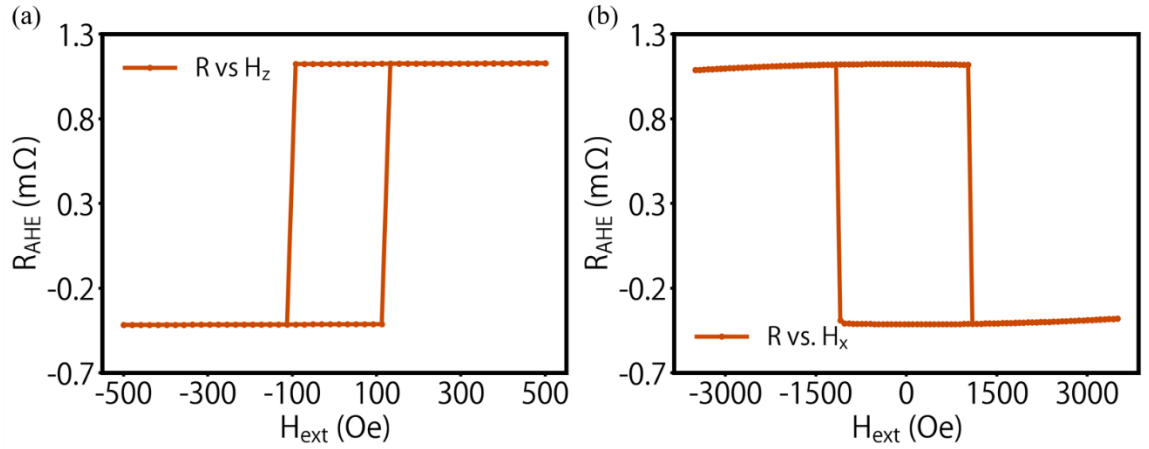


Fig. 5. 2 Anomalous Hall response of the structure W(4)-FeCoB(t)-Hf(0.1)-MgO-Ta (annealed at 300 °C) with easy axis (a) and hard axis (b) scan of the external magnetic field

The easy axis scan (out-of-plane direction) shows abrupt switching with a coercive field of $H_c \sim 100$ Oe. The hard axis scan shows a small parabolic curvature around zero field, which shows the coherent rotation of the magnetization with external field. We can use this region to fit to the macrospin model and get the anisotropy field H_{an} as follows,

$$R_{AHE} = \Delta R [1 - \frac{1}{2} (\frac{H}{H_{an}})^2] \quad (5.5)$$

We calculate PMA energy density K_{eff} through $K_{eff} \equiv \mu_0 H_{an} M_s / 2$ and plot it with various FeCoB thicknesses $t_{FeCoB}^{eff} = t_{FeCoB} - t_d$ where t_d denotes dead layer thickness as measured by VSM. Figure 5.3(a) shows the results at different annealing temperatures. The dashed lines show fitting to the relation $K_{eff} \cdot t_{FeCoB}^{eff} = (K_v - 2\pi M_s^2) \cdot t_{FeCoB}^{eff} + K_s$ where K_v (K_s) is the bulk (interfacial) anisotropy energy density. At 300 °C annealing temperature, K_s reaches 1.8 erg/cm², almost twice the value as in the 240 °C sample, indicating an enhanced Hf dusting effect.

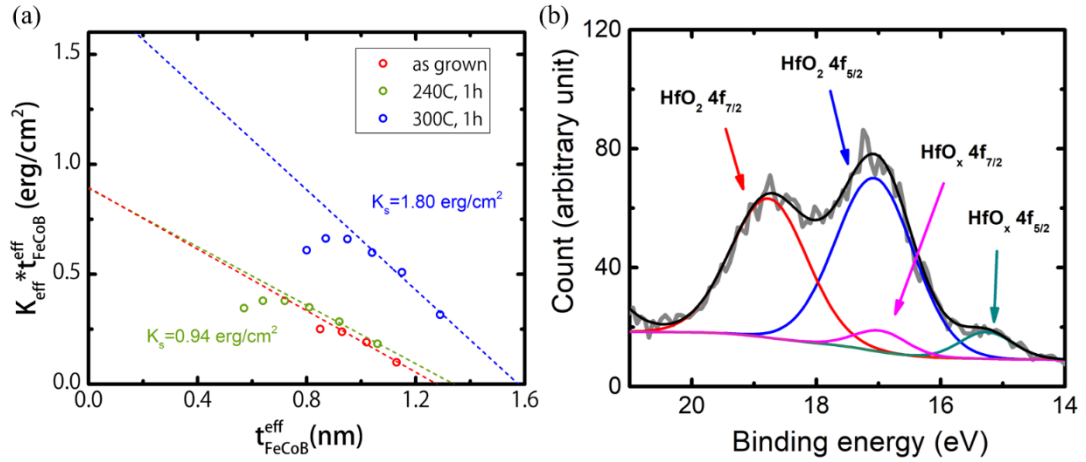


Fig. 5. 3 Perpendicular anisotropy energy density at different annealing temperatures for a structure W(4)-FeCoB(t)-Hf(0.1)-MgO-Ta (a) and XPS measurements done on a structure W(4)-FeCoB(1.8)-Hf(0.3)-MgO-Ta (b)

To get more insight into the Hf dusting effect, we carried out X-ray photoelectron spectroscopy (XPS) measurement and explored the chemical composition of the material stacks. The structure of the sample is as follows, W(4)-

FeCoB(1.8)-Hf(0.3)-MgO-Ta. We chose a structure with a relatively thick Hf dusting layer to enhance the signal of the XPS measurement. As is shown in the Fig. 5.3(b), various Hf oxide peaks were observed while there was no evidence of the metallic Hf peak, which indicates that the 0.3 nm Hf is fully oxidized and turns into HfO_x . We also obtain results showing the broadening of the Fe peak without Hf dusting layer, similar to what Ou et al. reported in the Ta-FeCoB-MgO system⁸⁷. We conclude that the very thin layer of Hf inserted between FeCoB and MgO absorbs oxygen liberated during the deposition of the MgO layer and creates a better interface for Fe-O bond than the original FeCoB/MgO interface, which leads to significantly enhanced PMA in the system.

5.2 Switching of the MTJs with a Hf dusting layer

Based on the observation of the enhancement of PMA using the Hf dusting layer, we designed an MTJ stack structure using 0.1 nm Hf dusting and β phase tungsten (W) as the spin Hall channel material, W(4)-FeCoB(1.8)-Hf(0.1)-MgO(1.6)-FeCoB(4)-Capping (hereafter called “W5”). In the meantime, a control sample W(4)-FeCoB(1.8)-MgO(1.6)-FeCoB(4)-Capping (hereafter called “W10”) was grown as the comparison to W5. We patterned the sample into 3T-MTJs using the procedures described in Chapter 3. Among various sizes of the designed devices, we choose the same nominal size of $390 \times 110 \text{ nm}^2$ devices on 500 nm wide channels for clarity of comparison between W5 and W10. Both samples were annealed in an air furnace at 300 °C for 1 hour to improve TMR. The annealing temperature dependence of the Hf dusting MTJ switching will be discussed in the next section. Figure 5.4(a) shows a

schematic of the device structure and Fig. 5.4(b) shows an SEM image of the MTJ pillar sitting on the W channel after the E-beam lithography.

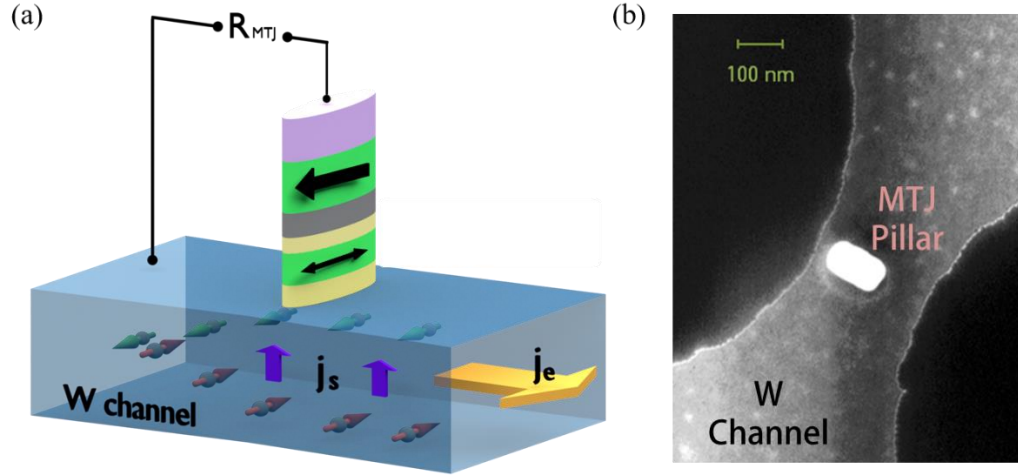


Fig. 5. 4 Device schematic and an SEM image of an MTJ pillar on a W spin Hall channel.

To measure the MTJ resistance, a lock-in measurement method described in Chapter 4 is used with DC probe placed across the top terminal and one of the bottom terminals of the device. To apply DC switching current to the channel, an RF probe connected to a Keithley 2400 current source is placed across the bottom terminals. When current is passed through the channel, the spin current generated from the spin Hall effect carrying a specific spin polarization depending on the polarity of the electric current is deflected upward to the FL, and, if strong enough, switches the FL through the anti-damping torque. First, we show field switching minor loops of the W5 (blue) and W10 (red) devices in Fig. 5.5(a). Both switching directions show a sharp, abrupt reversal of the FL, indicating a well-patterned MTJ pillar shape and a rigid reference layer (RL). The W5 device shows a slightly smaller hysteresis width (coercive field) possibly due to a less ideal ion beam etching that leaves a larger taper

on the FL which reduces the shape anisotropy. As can be seen in eqn. (1), H_c is more than an order of magnitude smaller than M_{eff} , thus having much less influence on the critical switching current density, which should not affect our analysis of the Hf dusting effect on our devices. However, H_c does affect the thermal stability Δ , which will be confirmed in the ramp rate measurement results to be discussed later.

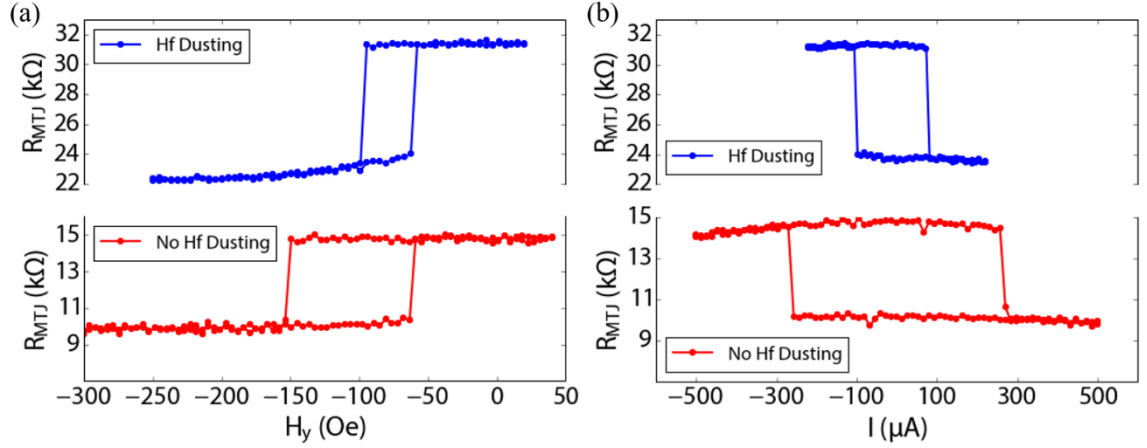


Fig. 5.5 Comparison of W5 and W10 devices. (a), Magnetic minor loop (b), Current induced switching loop

In Fig. 5.5(b) we show a comparison of switching current I_c between W5 and W10 devices when current is swept quasi-statically in the W channel. Note that an external field equal to the dipole field observed in the field switching minor loop is applied during the current sweep to center the loop around zero and all the subsequent measurements are done with this field applied. The dipole field is due to the thick RL inducing a dipolar interaction on the FL and can be eliminated by carefully engineering a synthetic antiferromagnetic (SAF) layer as the RL, which is a well-developed technique in industry. The I_c is seen to be almost 3 times smaller in the W5 device with 0.1 nm of Hf dusting compared to without Hf insertions. To account for

the thermal fluctuation in the devices, we carry out ramp rate measurement in which we ramp the current in the channel at different rates (10^{-7} A/s to 10^{-5} A/s) and record different I_c 's at each current ramp rate. We obtain data sets shown in Fig. 5.6 and fit to a thermal activation model,

$$I_c = I_{c0} \left\{ 1 - \frac{1}{\Delta} \ln \left[\frac{1}{t_0 \Delta} \left(\frac{|I_{c0}|}{|\dot{I}|} \right) \right] \right\} \quad (5.6)$$

Here I_{c0} is the critical current in the absence of thermal fluctuation (zero-temperature critical current), \dot{I} is current ramp rate, Δ is the thermal stability factor that represents the normalized magnetic energy barrier for reversal between the P and AP states, and τ_0 is the thermal attempt time which we assumed to be 1 ns, as is standard practice.

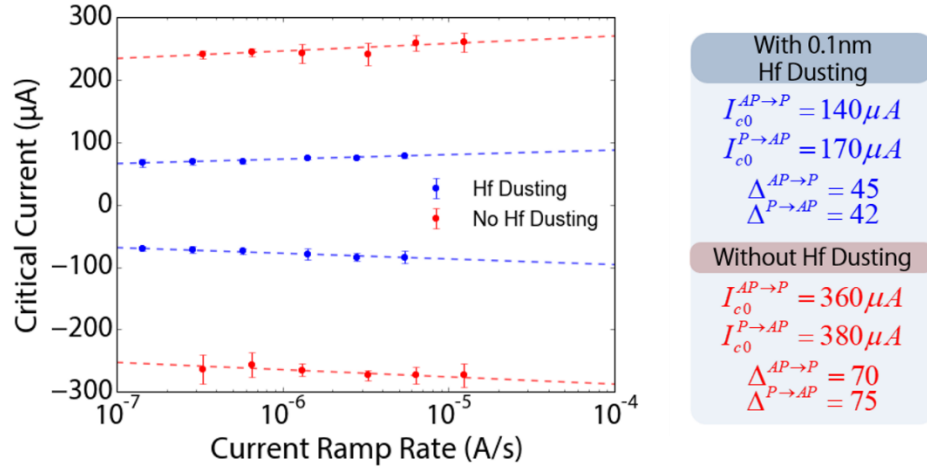


Fig. 5. 6 Current ramp rate measurements on W5 and W10 devices and fitting results

We observe that after accounting for the thermal fluctuation, the W5 device with Hf dusting still shows significant reduction of I_{c0} (an average of 155 μA)

compared to the W10 device (370 μA). As is indicated from the H_c analysis, Δ in the W5 device is smaller than in the W10 device. However, it is still greater than 40, which signifies data retention of 10 years, and better engineering of the fabrication procedure is easily achievable to offer much better thermal stability for device operation at elevated temperatures.

To confirm that the reduction of the I_{c0} is rooted in the reduction of the M_{eff} facilitated by the Hf dusting layer, we performed flip-chip FMR measurements on W5 and W10 structures both annealed at 300 $^{\circ}\text{C}$. The FMR chips were taken from the non-device region of each wafer where full stack of the MTJ is preserved after the fabrication. We first show in Fig. 5.7(a) a comparison of the resonances of the two structures at the same frequency 9 GHz. It can be clearly seen that without Hf dusting layer (red), there are two resonance peaks close to each other, with the larger amplitude peak being the thick RL resonance and the smaller amplitude peak being the FL resonance. However, with the Hf dusting layer (blue), the FL peak is shifted to a much higher magnetic field. The resonance field vs. frequency relation is described by the Kittel model,

$$f = (\gamma / 2\pi) \sqrt{H(H + 4\pi M_{\text{eff}})} \quad (5.7)$$

where γ is the gyromagnetic ratio, H is the resonance field and M_{eff} is the demagnetization field. At a fixed frequency, a larger resonance field indicates a smaller M_{eff} , which coincides with our results on W5 and W10. To further characterize the M_{eff} , we fit the resonance curves to a Lorentzian form as shown by Fig. 5.7(b) and extract the linewidth and the resonance field. In the case where RL and FL resonances are very close or even overlap, we model using a superposition of two Lorentzian

functions with different linewidths and resonance fields, as shown in Fig. 5.7(c). We show the resonance field – frequency relation in Fig. 5.7(d). As fitted by eqn. (5), M_{eff} of W5 (blue) is 1550 Oe, compared to 7570 Oe in W10 (red), almost a $5\times$ reduction. This successfully explains the large reduction of I_{c0} in the devices shown by the ramp rate measurements.

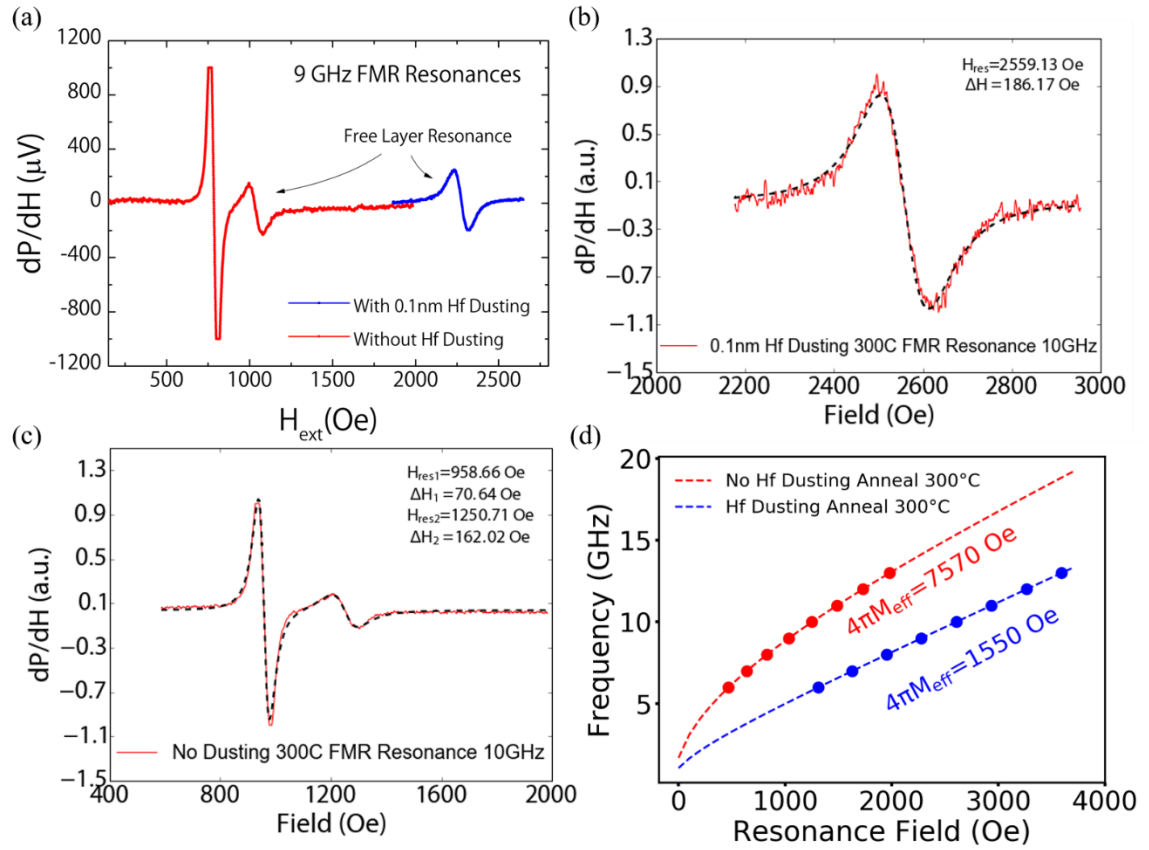


Fig. 5. 7 FMR measurements on W5 and W10 samples. (a), Comparison of 9 GHz resonances of the two samples, showing a large shift of the resonance field with Hf dusting. (b) and (c), Resonance raw data and fitting. (d), Fitting to the Kittel model and extracted M_{eff} showing a large reduction with Hf dusting layer.

Additionally, we grew wafers with different Hf dusting thicknesses and compared the effectiveness in Fig. 5.8. The samples have the same base structure W(4)-FeCoB(1.8)-Hf(t)-MgO(1.6)-FeCoB(4)-Capping with the only difference in the

Hf dusting thickness t from 0 to 0.1 nm. The samples shown in Fig. 5.8 are all annealed at 240 °C for comparison. As is seen in the decreasing trend of M_{eff} , Hf dusting is an effective way of tuning the demagnetization field, thus the critical switching current, and one can adjust the thickness of the Hf layer (in combination with the annealing temperatures, as will be shown in the next section) to achieve the amount of M_{eff} preferred for different applications.

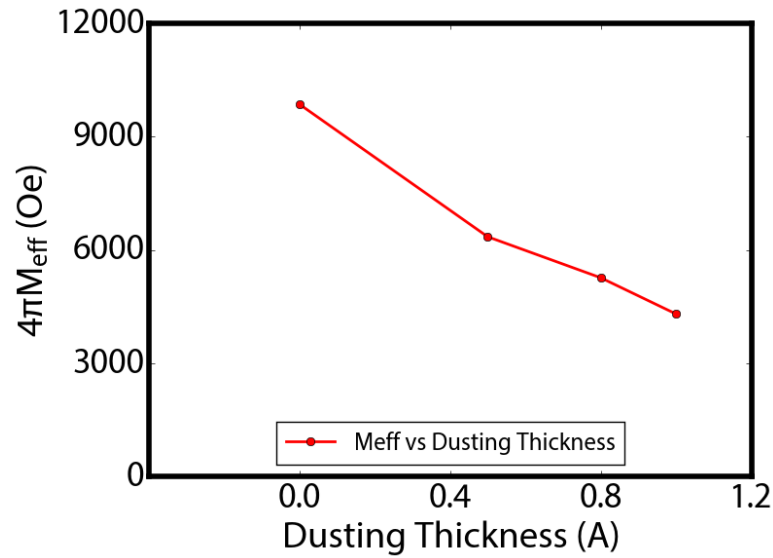


Fig. 5. 8 M_{eff} of MTJ structures with different Hf dusting thicknesses

5.3 Temperature dependence of Hf dusting effect

We have shown in section 5.2 that the insertion of a Hf dusting layer, as thin as 0.1 nm, can dramatically change the demagnetization field of the FL, resulting in large reduction of the critical switching current of the MTJ device. However, it is also crucial to investigate thermal robustness of this engineering method so that it is useful in application in industrial fabrication where back-end-of-the-line thermal procedure can go up in temperature to above 400 °C for up to several hours in total time. People

have found that some metals, including Pt and Hf can possibly diffuse to adjacent layers at high processing temperatures, which can be a big obstacle for future applications of those structures in integrated circuits^{88,89}.

In order to test the thermal robustness of the Hf dusting technique, we take W5 devices and anneal them to different temperatures, 240 °C and 300 °C. We carry out similar FMR measurements first and show in Fig. 5.9(a) the comparison of the two samples. The sample annealed at 240 °C shows $M_{\text{eff}} \sim 4300$ Oe (magenta), almost 3 times larger compared to the sample annealed at 300 °C (blue), although still smaller compared to $M_{\text{eff}} \sim 5600$ Oe in the as-grown state.

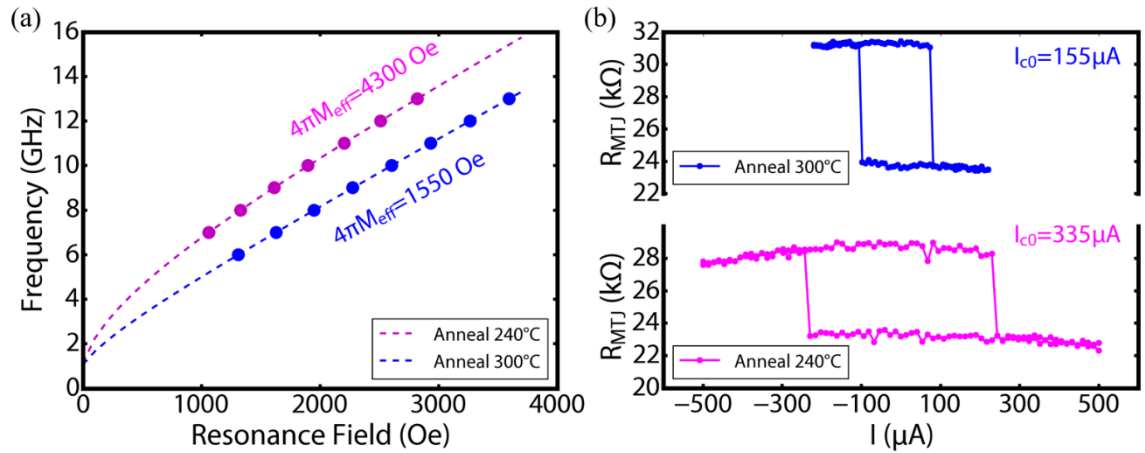


Fig. 5. 9 W5 devices annealed at different temperatures, 240 °C and 300 °C. (a), FMR measurements showing reduced M_{eff} at the higher annealing temperature. (b), Switching experiments confirm the reduction of I_{c0} at the higher annealing temperature.

Consistent with our analysis, the device annealed at 240 °C also shows a larger switching current compared to the device annealed at 300 °C, due to the larger M_{eff} . Shown in Fig. 5.9(b) is the comparison of the current switching loops at two different annealing temperatures with the inset notes showing zero-temperature critical current I_{c0} after the ramp rate measurements (data not shown here).

As a separate check of the Hf dusting effect, we measured the saturation magnetization M_s of the W5 sample at annealing temperatures $T = 240^\circ\text{C}$ and $T = 300^\circ\text{C}$. As is shown by Fig. 5.10, M_s at 300°C annealing is $\sim 1.4 \times 10^6$ A/m, slightly higher than $\sim 1.33 \times 10^6$ A/m at 240°C annealing, which confirms that the reduction of M_{eff} is only due to the enhancement of interfacial PMA caused by the Hf dusting layer, and not by the change of M_s .

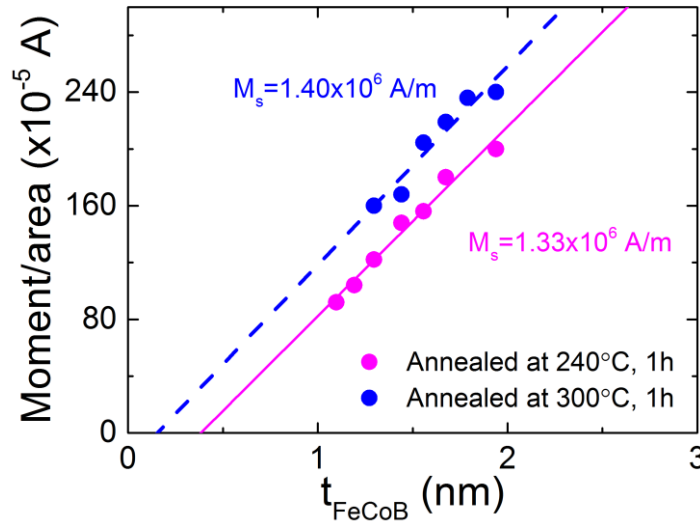


Fig. 5. 10 Saturation magnetization M_s at two different annealing temperatures, 240°C and 300°C .

Next we tried to anneal structures with different Hf dusting thicknesses to different temperatures to confirm our findings in our W5 sample. We prepared three samples with Hf dusting layer thickness $t = 0$ nm (W10), $t = 0.05$ nm (W13), and $t = 0.1$ nm (W5) while keeping the other layers the same in the stack. We carried out FMR measurement after annealing at temperatures $T = 240^\circ\text{C}$, $T = 300^\circ\text{C}$, $T = 350^\circ\text{C}$ as well as in the as grown state. Figure 5.11 shows the results we got from the above measurements. First, we see that M_{eff} decreases with thicker Hf dusting layers, which is consistent with results shown in the previous section. Without Hf dusting,

M_{eff} reaches above 1 T, while with Hf dusting and thermal annealing M_{eff} drops to below 2000 Oe, more than a factor of 5 reduction. Second, all three samples show a monotonic decrease of M_{eff} with higher annealing temperatures, which indicates an enhanced interfacial PMA possibly involving boron diffusion. Note that for W5 the M_{eff} saturates at above 300 °C where the magnetization is close to out-of-plane and further annealing will likely change the anisotropy direction.

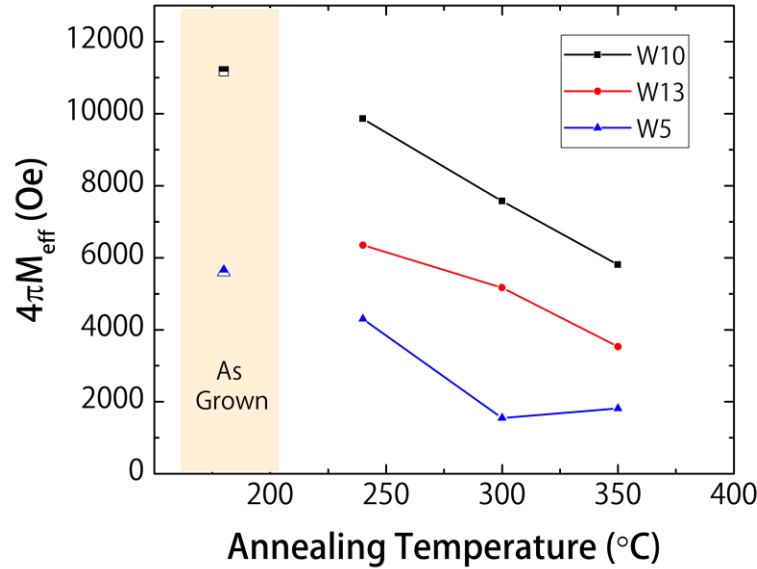


Fig. 5. $11 M_{\text{eff}}$ in various structures at various annealing temperatures. W10 – without Hf dusting layer. W13 – with 0.05 nm Hf dusting layer. W5 – with 0.1 nm Hf dusting layer.

The annealing test results show that the Hf dusting effect is enhanced at higher annealing temperature, which is highly preferable given the standard high temperature processing protocols applied in the existing semiconductor industry. We can achieve even lower write energy in the integrated circuit without degrading the thermal stability if we carefully control the fabrication procedures. When we look at the devices at the highest annealing temperature, we find that the high resistivity tungsten

maintains its β phase, despite some early debates on its high temperature annealing performances^{90,91}.

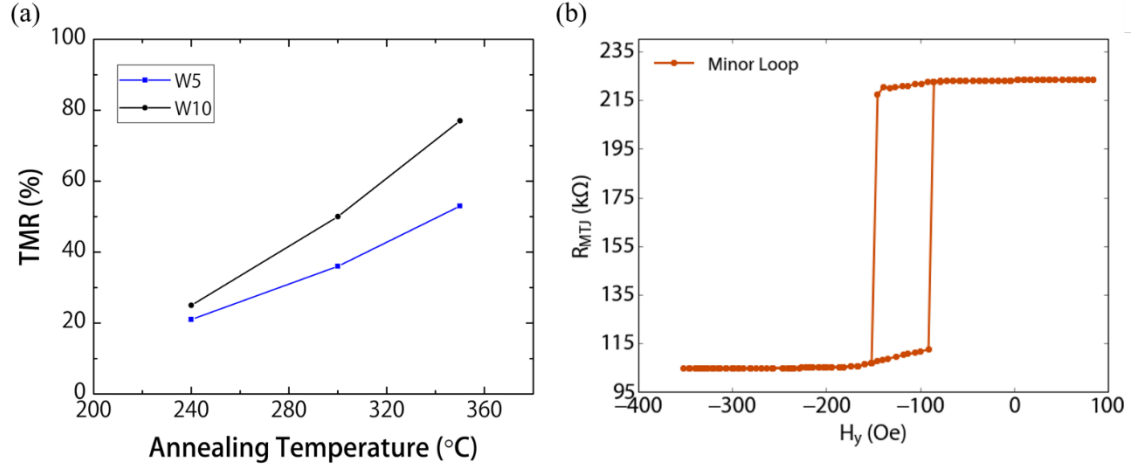


Fig. 5.12 (a), TMR of W5 and W10 devices at different annealing temperatures. (b), A thinner Hf dusting layer and higher annealing temperature result in much higher TMR.

In the meantime, TMR was greatly enhanced at the higher annealing temperatures due to better crystallization of the FeCoB/MgO/FeCoB lattices^{27,92,93}. Figure 5.12(a) shows TMR in W5 (blue) and W10 (black) devices. With Hf dusting layer, TMR is reduced due to the extra HfO_x layer breaking the FeCoB/MgO tunneling interface through additional spin scattering. However, there are methods to address this potential issue including using thinner Hf thickness and higher annealing temperature. Figure 5.12(b) shows an example of a W13 device (0.05 nm Hf dusting) annealed in a vacuum furnace at a set temperature of 350 °C (actual temperature in the chamber is calibrated to be ~ 450 °C). TMR above 100% can be achieved, showing adaptivity of the Hf dusting technique to standard processing protocols.

5.4 Control of magnetic damping through additional Hf spacer layer

While M_{eff} is a key factor determining the critical switching current, there is another important parameter that will affect the efficiency of the switching – the magnetic damping α . Unlike the SOT switching of PMA devices with the effective field of the spin transfer torque where high damping helps to relax the magnetization to the switched state faster, switching through anti-damping torque in the in-plane devices can take advantage of the small damping and excite the precession of the magnetization at the beginning of the switching with lower current. As damping is both a bulk property determined by the ferromagnetic material and an interfacial property affected by the spin scattering at the interface, we tried to reduce the damping through another way of interface modification.

Nguyen et al. have shown that an insertion of a 0.5 nm Hf layer separating Pt and FeCoB can result in an effective reduction of the damping through the suppression of spin dependent scattering without significant attenuation of spin current that is transmitted into the FeCoB layer⁸⁸.

We tried a similar method and inserted an even thinner Hf spacer of only 0.25 nm between the W channel and the FeCoB FL. The structure of the sample was as follows, W(4)-Hf(0.25)-FeCoB(1.8)-Hf(0.1)-MgO(1.6)-Capping layer (hereafter called “W9”). Note that we also used a Hf dusting thickness of 0.1 nm following the analysis in the previous sections to reduce M_{eff} . The sample was annealed in an air furnace at 240 °C for 1 hour.

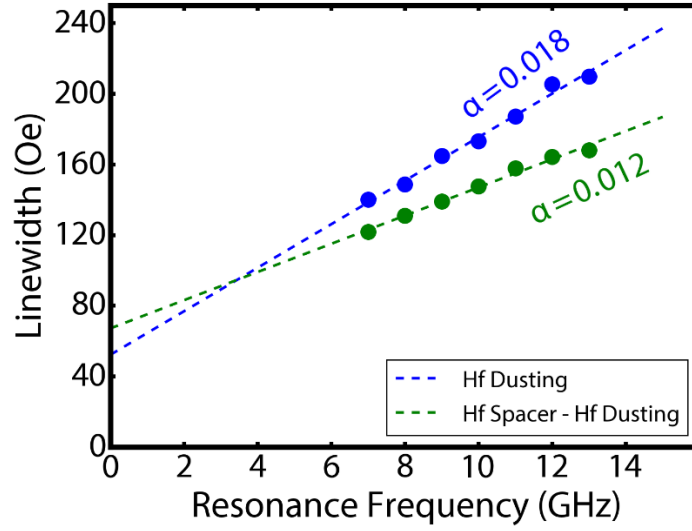


Fig. 5. 13 Comparison of damping α between W5 and W9 samples both annealed at 240 °C

We show in Fig. 5.13 a comparison of damping α between the sample with only Hf dusting layer (W5, blue) and the sample with both Hf dusting and Hf spacer layers (W9, green). The results obtained from the FMR measurements can be fitted using

$$\Delta H = \frac{2\alpha}{\gamma} f + \Delta H_0 \quad (5.8)$$

where ΔH is the linewidth and ΔH_0 is inhomogeneous linewidth that is usually material defect related and is not affected by the resonance frequency. As indicated by the slope of the fitting lines, the damping in the Hf spacer - Hf dusting sample is about 30% lower than the sample with only the Hf dusting layer, which is another boost in the reduction of the I_{c0} .

We summarize the M_{eff} in various W-based MTJ structures in Fig. 5.14. As is explained in section 5.3, a large reduction of M_{eff} in W5 samples compared to W10 without Hf insertion layers is due to the Hf dusting enhancing the interfacial PMA,

and the effect is further enhanced at higher annealing temperatures. While the additional insertion of the 0.25 nm Hf spacer at W/FeCoB interface is aimed at reducing the damping α , we see a further decrease of M_{eff} in this Hf dusting - Hf spacer structure, giving almost half of the value compared to the Hf dusting only sample. This is possibly due to diffusion of some the Hf spacer material during the annealing to the FeCoB/MgO interface, which further helps to strengthen the PMA, as seen in a previous report^{88,94}. Note that in the W9 sample, annealing at 300 °C caused the FL to start losing in-plane anisotropy and fall into an intermediate regime where the anisotropy transitions from in-plane to out-of-plane, which led to a failure of FMR analysis as well as unstable MTJ devices. One can possibly avoid this issue by reducing the thickness of the Hf dusting and anneal to higher temperature to achieve both low M_{eff} and higher TMR.

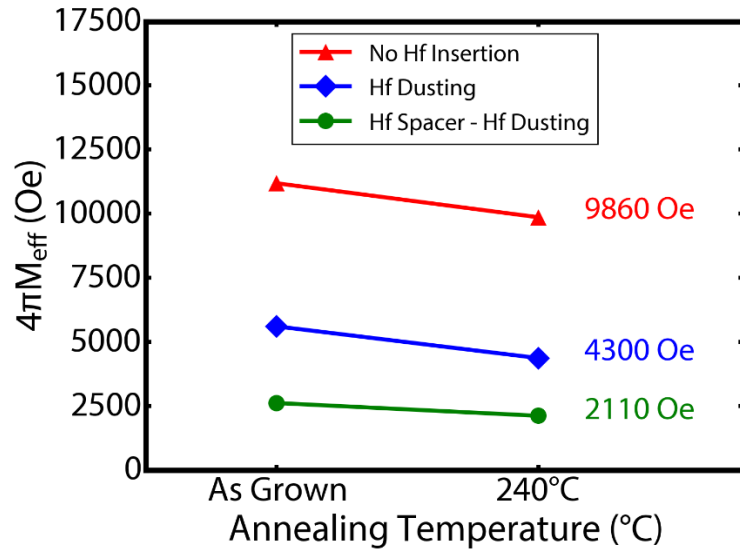


Fig. 5. 14 A summary of M_{eff} in various structures at different annealing temperatures

We next show switching results from a typical W9 sample of size 190×30 nm² on a 480 nm wide, 4.4 nm thick W channel with both Hf spacer and Hf dusting

layers. In the inset of Fig. 5.15(a), field switching minor loop of the W9 sample shows abrupt reversal of the FL with a coercive field of ~ 40 Oe. A DC switching current of ~ 50 μA is observed in this sample. This is about 40% lower than the W5 sample with only Hf dusting layer, as shown by the comparison plotted in Fig. 5.15(b).

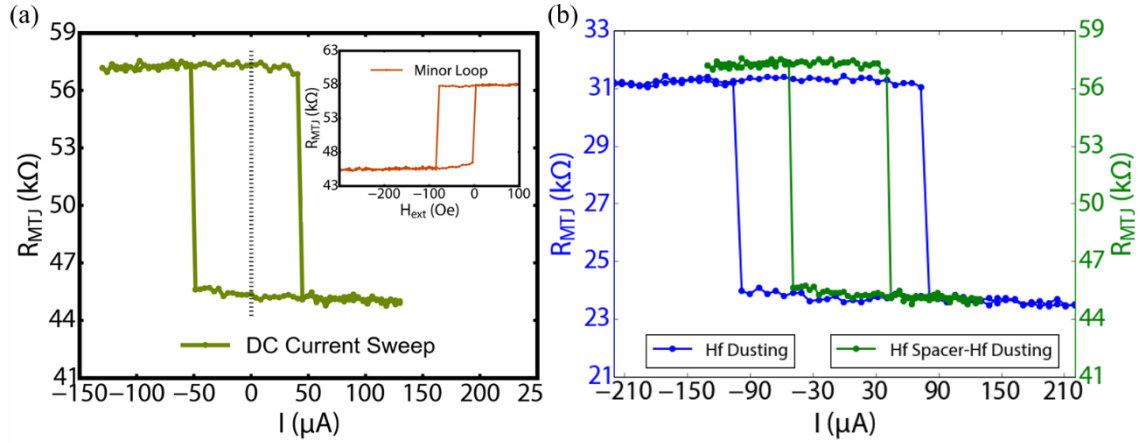


Fig. 5. 15 Current induced switching in Hf dusting - Hf spacer sample (W9) and comparison of I_c between W9 and W5.

We carried out ramp rate measurements and show data and the fitted results in Fig. 5.16. With both Hf dusting and Hf spacer layers, we achieved $I_{c0} = 115$ μA , which converted to switching current density by using $t_{chan} = 4.4$ nm and $w_{chan} = 480$ nm, is $J_{c0} = 5.4 \times 10^6$ A/cm², the lowest ever achieved in any three terminal devices.

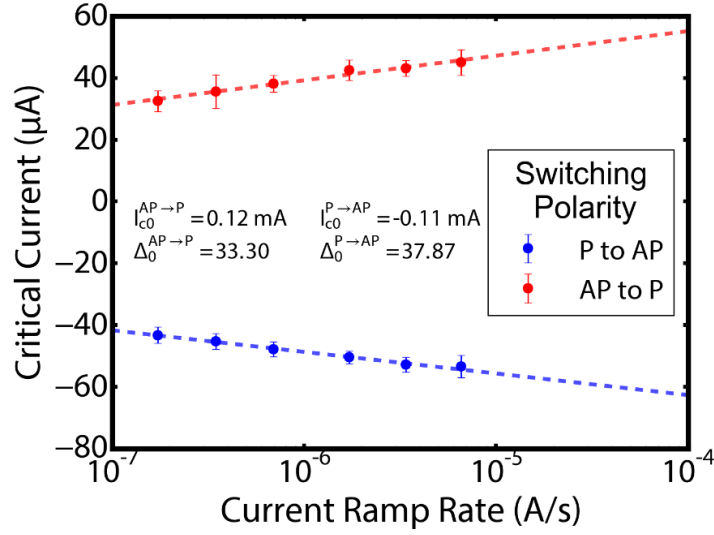


Fig. 5. 16 Ramp rate measurements on a W9 device with both Hf dusting and Hf spacer layers. An average of $I_{c0} = 115 \mu\text{A}$ and $\Delta = 36$ is achieved.

The $3.6 \text{ k}\Omega$ channel resistance indicates that the W channel is still in its β phase. Additionally we can calculate the spin torque efficiency ξ_{DL} from eqn. (5.1) using the parameters obtained from current switching and FMR measurements. We get $\xi_{\text{DL}} = -0.15 \pm 0.03$ for the measured device, which is lower than reported values from previous works^{10,71,95}. This is expected due to the Hf spacer attenuating the spin current, thus reducing the strength of the spin torque exerted on the FL layer. To confirm the results calculated from the switching model, we fabricated two control samples with a Hall bar geometry, W(4)-FeCoB(t_{FeCoB})-Hf(0.1)-MgO-Ta (annealed at 240°C , 1hour) and W(4)-Hf(0.25)-FeCoB(t_{FeCoB})-Hf(0.1)-MgO-Ta (annealed at 240°C , 1hour). We carried out spin torque FMR (ST-FMR) measurement to evaluate the spin torque efficiency in the two structures. When there is a constant, significant field-like torque in the heterostructure⁸⁶, the spin torque efficiency, ξ_{FMR} , measured by the ratio of the symmetric and anti-symmetric components of the ST-FMR lineshape, can

be expressed as¹¹:

$$\frac{1}{\xi_{FMR}} = \frac{1}{\xi_{DL}} \left(1 + \frac{\hbar}{e} \frac{\xi_{FL}}{4\pi M_s t_{FM} t_{HM}} \right) \quad (5.9)$$

where ξ_{DL} and ξ_{FL} stand for damping-like and field-like spin torque efficiency, respectively, and t_{FM} (t_{HM}) stands for the thickness of the ferromagnet (heavy metal).

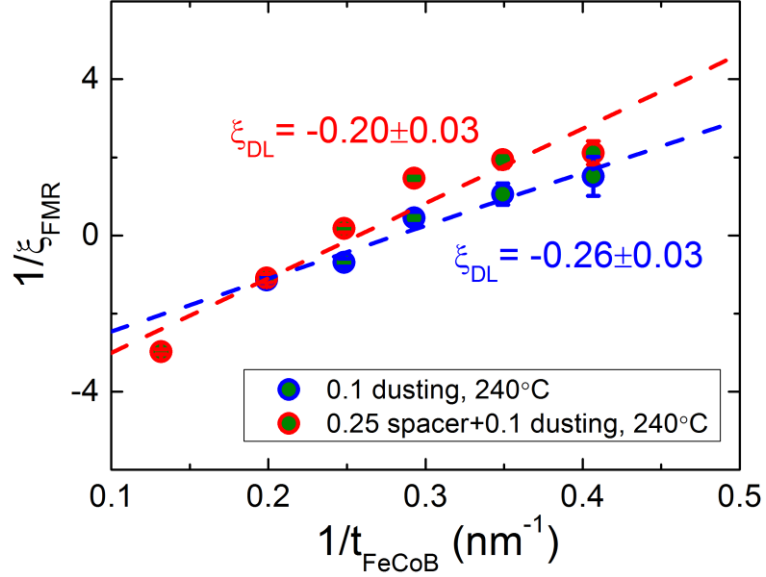


Fig. 5. 17 ST-FMR measurement on two structures with Hf dusting + Hf spacer and without any Hf insertion layers, both annealed at 240 °C

The intercept of the linear fit gives the $\xi_{DL} = -0.26 \pm 0.03$ for sample W(4)-FeCoB(t_{FeCoB})-Hf(0.1)-MgO-Ta and $\xi_{DL} = -0.20 \pm 0.03$ for sample W(4)-Hf(0.25)-FeCoB(t_{FeCoB})-Hf(0.1)-MgO-Ta, in reasonable agreement with the calculated values from our switching measurements, but somewhat above those values. The slight difference could be the result of an increase in damping in our nanostructures due to side-wall oxidation of the nanopillar in the lithography process, which can be addressed by in-situ passivation in the future⁹⁶. We see that there is some attenuation of the spin current as 0.25 nm Hf spacer is inserted. However, the reduction of the

damping outweighs the cost of the spin torque attenuation and further careful engineering of the Hf thicknesses is achievable to optimize the structure for better performance.

Finally, we summarize the critical switching current achieved in various kinds of in-plane and PMA 3T structures in Table 5.1. The in-plane devices show a significantly lower write current density than the PMA devices, which in many cases still require an in-plane external field to deterministically switch the magnetization between two distinct states. Among the in-plane devices, our W-based structure with Hf dusting and spacer layers shows a very great promise for future application with its low energy consumption, non-volatility and high degree of freedom for further optimization.

	W with Hf insertion layers	W	Pt	Ta	PMA W/CoFe B/MgO nanodot	PMA MTJ with Ta channel	3T DW motion device
Anisotropy	In-plane-magnetized				PMA		
Critical current density ($\times 10^6$ A/cm ²)	5.4	18	40	32	>140	>50	>50
Reference	This work	Pai et al. ¹⁰	Aradhya et al. ⁶⁸	Liu et al. ⁹⁷	Fukami et al. ⁹⁸	Cubukcu et al. ⁹⁹	Fukami et al. ¹⁰⁰

Table 5. 1 Comparison of J_{c0} between the different 3T-MTJ structures reported to date

5.5 Fast and reliable pulse switching in Hf dusting – Hf spacer structures

We have shown in the previous sections that the Hf dusting and Hf spacer layers are effective ways to reduce the switching current in 3T-MTJ structures. For application, especially as replacement of SRAM in the cache memory, fast switching

is also highly preferred. We explored the switching of our W-based MTJs with Hf insertion layers in the short pulse switching regime. The device we measured is a W9 device of size $190 \times 30 \text{ nm}^2$ and is annealed at 240°C for 1 hour. We used the pulse switching setup introduced in Chapter 4 and applied short voltage pulses to the W channel. Similar to the DC current flowing continuously in the channel, voltage pulses in the nanosecond (or even picosecond) regime can also generate spin current that will switch the FL in a shorter time scale. When we send a voltage pulse of a specific combination of the amplitude and duration, we measured the resistance of the MTJ after the pulse and determine whether the MTJ has been switched. We repeated the same switching trial 1000 times to calculate the switching probability for this combination. We then varied the pulse amplitudes and durations and obtained switching probability curves as shown in Fig. 5.18. As is expected from the spin torque switching model, the switching probability P_{switch} increases as the pulse duration increases for a fixed pulse voltage. Similarly P_{switch} increases as pulse voltage increases for a fixed pulse duration. Both polarities AP \rightarrow P and P \rightarrow AP reach $P_{\text{switch}} \sim 100\%$ at $V_{\text{switch}} = 1.88 \text{ V}$ in as short as 1 ns.

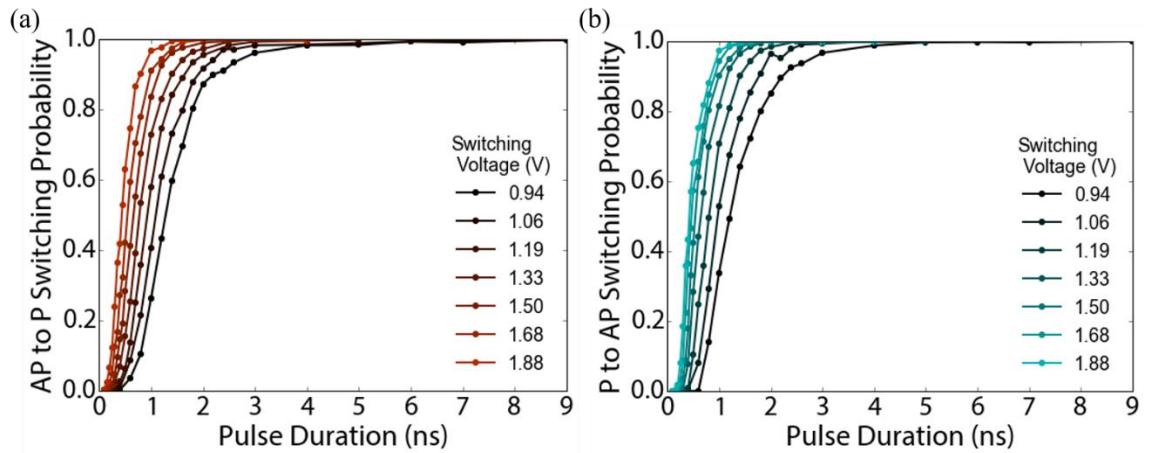


Fig. 5. 18 Pulse switching probabilities of a W9 device annealed at 240 °C for polarities (a), AP→P (b), P→AP.

To get a clearer picture of the switching behavior and more information regarding the critical switching voltage and critical switching time scale, we did more intense measurements on another device with the same nominal size, and plot switching phase diagrams in Fig. 5.19. A voltage range of 0.45 – 1.3 V and a duration range of 0.2 – 8 ns are used to do the measurement and produce the phase diagram with a grid size of 70×70 (4900 data points, with each point being the P_{switch} of 1000 switching attempts). The red color represents the non-switching region and the black color represents the 100% switching region. In the middle where the behavior transitions from non-switching to 100% switching are the 50% switching probability points as shown by green points. Although non-uniform micromagnetic dynamics are likely to be involved in the switching and affect the overall behavior^{67,68}, we employed a macrospin model that still reasonably describes our observation¹⁰¹:

$$V = V_0 \left(1 + \frac{t_0}{t}\right) \quad (5.10)$$

where t_0 and V_0 are the characteristic switching time and the critical switching voltage, respectively. From the fitting we extracted the values to be $V_{0, \text{AP} \rightarrow \text{P}} = 0.44$ V, $t_{0, \text{AP} \rightarrow \text{P}} = 1.2$ ns and $V_{0, \text{P} \rightarrow \text{AP}} = 0.48$ V, $t_{0, \text{P} \rightarrow \text{AP}} = 0.76$ ns. The average critical voltage of 0.46 V corresponds to $I_{c0} = 120$ μA ($J_{c0} = 5.9 \times 10^6$ A/cm²) using the channel resistance $R_{\text{chan}} = 3.6$ k Ω , which is consistent with our ramp rate results on the same structure. The short time scale $t_0 \sim 1$ ns shows that these devices can be driven very fast and still switch reliably for both polarities.

The fast switching combined with low switching current in our W-based

devices with Hf insertion layers achieve 0.2 pJ of write energy at ~ 1 ns operation speed, which is significantly lower than other emerging memory schemes, and is highly scalable compared to SRAM, making it very competitive as the future cache memory technology. Further reduction can be achieved by optimization of the channel design that reduces the channel resistance, thus lowering the energy cost of these devices to the fJ regime.

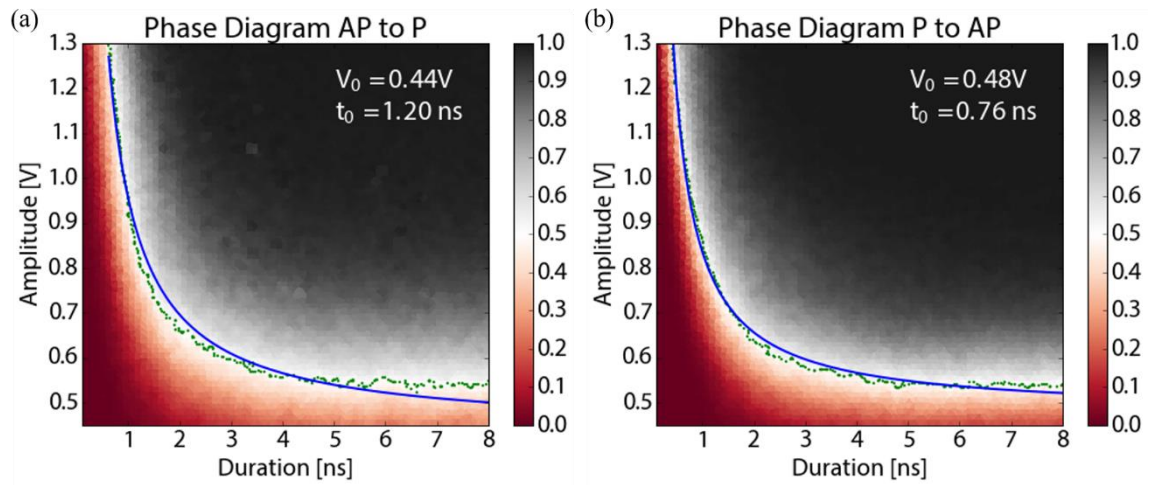


Fig. 5. 19 Pulse switching phase diagrams of a W9 device annealed at 240 °C

The characteristic time scale is much faster than predictions from the macrospin model. This is possibly due to the assistance from the large field-like torque observed in these structures. Aradhya et al. have shown that in Pt-based structures an in-plane Oersted field generated by electric current in the spin Hall channel helps to boost the short pulse switching since it is collinear with the in-plane anisotropy direction and always opposes the anisotropy at the beginning of the switching, which helps to effectively lower the energy barrier for the reversal⁶⁸. While in the W case where the sign of the spin torque efficiency is opposite to that of the Pt, which should

make the Oersted field disadvantageous for the reversal, the field-like torque opposes the Oersted field and is sizable. From the ST-FMR measurements shown in section 5.4 we can also extract the field-like spin torque efficiency $\xi_{\text{FL}} = -0.0364 \pm 0.005$, which corresponds to an effective field -6.68×10^{-11} Oe/(A/m²) in the MTJ structure with a 1.8 nm free layer, about three times larger than the Oersted field. This field-like torque overcomes the Oersted field and can assist the initial precession of the magnetization and lead to the fast reversal.

To further show the high reliability of these devices, we carry out write error rate (WER) measurements at 2 ns pulse duration where $\text{WER} = 1 - P_{\text{switch}}$ calculated at each voltage. Figure 5.20 shows that WER has a fast roll-off at higher pulse voltages and can achieve 10^{-6} with drive amplitude slightly larger than $3V_0$. Here each data point is the result of 10^6 switching trials. The results here are limited by the maximum voltage we can apply due to the poor quality of the protective oxide that breaks down above ~ 2.6 V. However, our WER shows high reliability of these devices and great promise for high endurance fast cache applications.

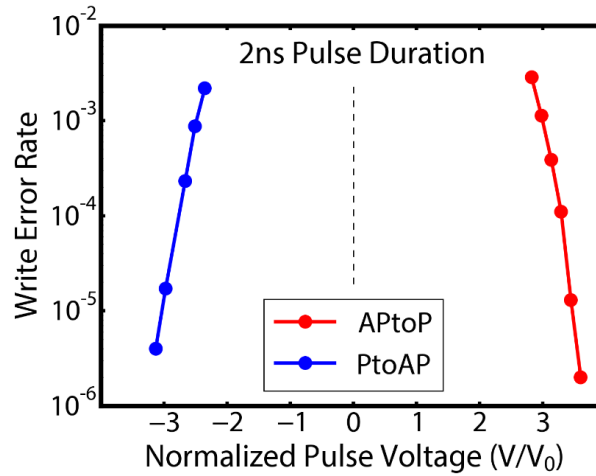


Fig. 5. 20 WER measurement on a W9 device annealed at 240 °C. WER as low as 10^{-6} can be achieved for both switching polarities.

CHAPTER 6

FAST AND RELIABLE SWITCHING IN $\text{Pt}_{85}\text{Hf}_{15}$ BASED IN PLANE MAGNETIC TUNNEL JUNCTIONS

In this chapter we introduce our work on achieving highly reliable pulse switching in in-plane-magnetized MTJs with a $\text{Pt}_{85}\text{Hf}_{15}$ alloy spin Hall channel. We show switching behavior with different MTJ shapes and excellent write error rate below 10^{-6} regardless of the variation of the shapes. These results demonstrate the advantage of the low impedance, high efficiency $\text{Pt}_{85}\text{Hf}_{15}$ as the spin Hall material and pave the way for the application of three terminal SOT devices in memory hierarchy in the near future.

6.1. Fast pulse switching using $\text{Pt}_{85}\text{Hf}_{15}$ alloy as the spin Hall channel

Since the discovery of the spin Hall effect, people have strived to find materials with high spin torque efficiency and low resistivity to optimize the write energy of current induced switching^{10,15,71,97,102}. While the heavy metal Pt is highly conductive with sizable spin torque efficiency, various studies on Pt have revealed different magnitudes of the spin torque efficiency and even have reported that different mechanisms are primarily responsible for the spin Hall effect¹⁰³. Our group has studied Pt with varying resistivity which indicated that the intrinsic mechanism of spin Hall effect in Pt is dominant, in which case the spin Hall conductivity $\sigma_{SH} = \theta_{SH} / \rho$ is the intrinsic property of the material¹². With this mechanism the apparent spin torque efficiency directly scales with the resistivity of the material, which indicates an effective way of raising the spin torque efficiency by introducing

scattering sites in Pt. We have shown that with 15% of Hf (atomic ratio) doped in Pt, the resistivity increases to $\sim 150 \mu\Omega\cdot\text{cm}$ and the highest spin torque efficiency of $\sim 23\%$ can be achieved¹³. Further switching experiments both in the thermally activated regime and in short pulse regime confirm that the $\text{Pt}_{85}\text{Hf}_{15}$ alloy is a more efficient spin Hall material than pure Pt, despite some discrepancy in the observed θ_{SH} between large scale structures and MTJs¹⁴. Here we further explore the short pulse switching behavior of $\text{Pt}_{85}\text{Hf}_{15}$ based MTJs with different device shapes. Reports have shown that in spin torque switching, the geometry of the sample can have a strong influence on the switching dynamics through intricate micromagnetic/domain configurations^{46,47,104}, and can be potentially useful in improving the switching efficiency.

The samples are prepared from a wafer grown by Canon Anelva, with the layer structures Ta(1)- $\text{Pt}_{85}\text{Hf}_{15}$ (5)-Hf(wedge,0.25-0.35)-FeCoB(1.4)-MgO(RA=200)-FeCoB(1.2)-Ta(0.2)-FeCoB(1.2)-FeCo(1)-Ru(0.85)-FeCo(2.5)-IrMn(7)-Ru(4) (Hereafter called “Canon4-7”). We designed devices with the same size of $190 \times 45 \text{ nm}^2$ in a rectangle shape and a triangular shape on 300 nm wide channels. Typical field and DC current switching loops of these devices are shown in Fig. 6.1 for reference.

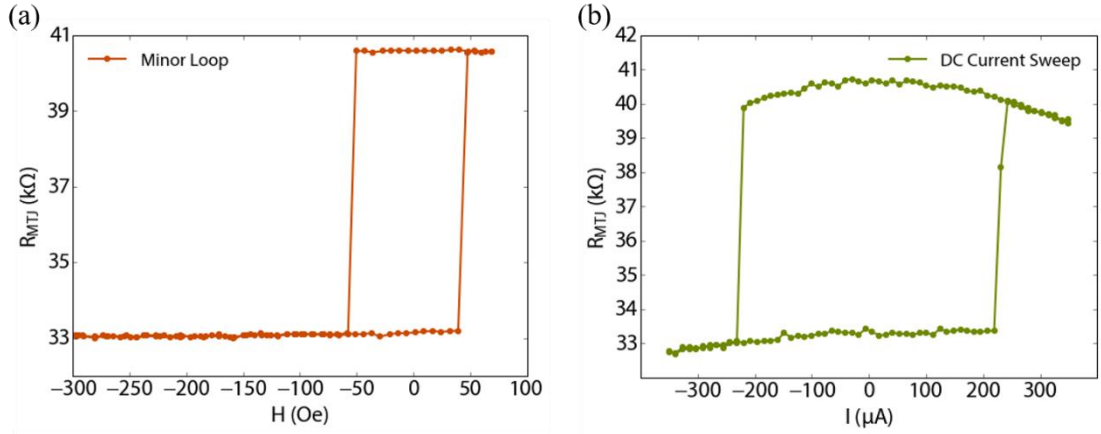


Fig. 6. 1 Typical field and current switching loops of Canon4-7 devices

We then carried out short pulse switching experiments using the DAQ measurement system described in Chapter 4. Previous reports have shown that there is an asymmetry in the switching of the three terminal devices, which is explained by the strength of the reference layer pinning⁶⁷. However, there could be more reasons why we see the asymmetry in our pulse switching experiments.

I will first show an example device with switching phase diagrams and macrospin fitting to the whole duration range in Fig. 6.2(a) and (b), using the model described in Chapter 5. Although the macrospin model describes the general switching behavior well with reasonable fitting parameters, it has the largest discrepancy at the middle of the duration range since it tries to account for both the short pulse region < 1 ns and long pulse region > 5 ns. Due to the sensitive nature of the switching behavior on the time scale, fitting to the same duration range (because the measurement is done with the same range) for $P \rightarrow AP$ and $AP \rightarrow P$ polarities can possibly be misleading because at certain pulse voltage the device could be driven in different regimes for different polarities based on their different V_0 's. The different V_0 's could be due to the

imperfection of the applied offset field, as discussed below, or other more intrinsic reasons possibly including the pulse induced tunneling current through the MgO barrier due to the low impedance path through the MTJ especially when RA product is low. This diverted current may assist the pulse switching through the STT mechanism in addition to the SOT switching from the SHE channel. As indicated by the green raw data points and the red imaginary curve in Fig. 6.2(c) and (d), if we shift one of the curves upward to account for the difference in V_0 , it is more reasonable to compare the behavior in two polarities since now they are driven in the same regime. We then try to fit the 50% probability data points in the range where the pulse amplitude is $V_0 \sim 2V_0$. The choice of the range is based on numerous fitting tests that yield the best fit regardless of the V_0 for each different device. While at the middle pulse durations the fitting lines coincide well with our experimental data, the fits in the long pulse regime and in the short pulse (high drive amplitude) regime deviate significantly from the macrospin model. At short pulses the device is driven with a high pulse amplitude, which could possibly induce complicated multiple domain nucleation procedure or larger assist from the tunneling current mentioned above. This could lower the energy needed to switch the device. As the macrospin switching transitions from ballistic regime to thermally activated regime, it usually happens at a time scale far greater than nanosecond regime. However, due to the domain structures in these devices, the saturation of the critical voltage in the long pulse region could potentially move ahead into the nanosecond regime, which is consistent with our measured results. Figure 6.2(e) and (f) show the new fitting scheme that captures the switching behavior in the same regime driven in two polarities.

To show the validity of this new fitting method, we carried out a set of pulse switching experiments where we varied the offset field on the device and obtained two different sets of phase diagrams for two polarities, as shown in Fig. 6.3. For Fig. 6.3(a) and (b), an offset field of $H_{\text{off}} = -17$ Oe was applied to cancel the small dipole field on the FL by the RL. This offset field was obtained from DC current induced switching measurement where the applied field was adjusted to center the hysteresis loop about zero current. For this applied field there was a small imbalance of the V_0 between the two pulse switching polarities, and the origin of this behavior is unclear at this moment. Figure 6.3(c) and (d) show the same switching experiments when we manually adjust the offset field towards favoring AP→P switching ($H_{\text{off}} = -21$ Oe). As a result, the AP→P curve is shifted downward which gives a smaller V_0 , and in this case reaches a good balance with the P→AP polarity. Although shifted vertically, the fitting of these curves using the adapted method shows almost the same t_0 's, which confirms that as long as the device is driven in the same regime, we are able to separate the V_0 and t_0 , and describe the switching behavior and asymmetry more reasonably. The validation here also indicates that these SOT devices are sensitive to the drive amplitude possibly due to the domain structure and nucleation procedure which, as suggested by micromagnetic modeling, strongly relies on the strength of initial kick which can drive the FL into non-uniform magnetization configurations.

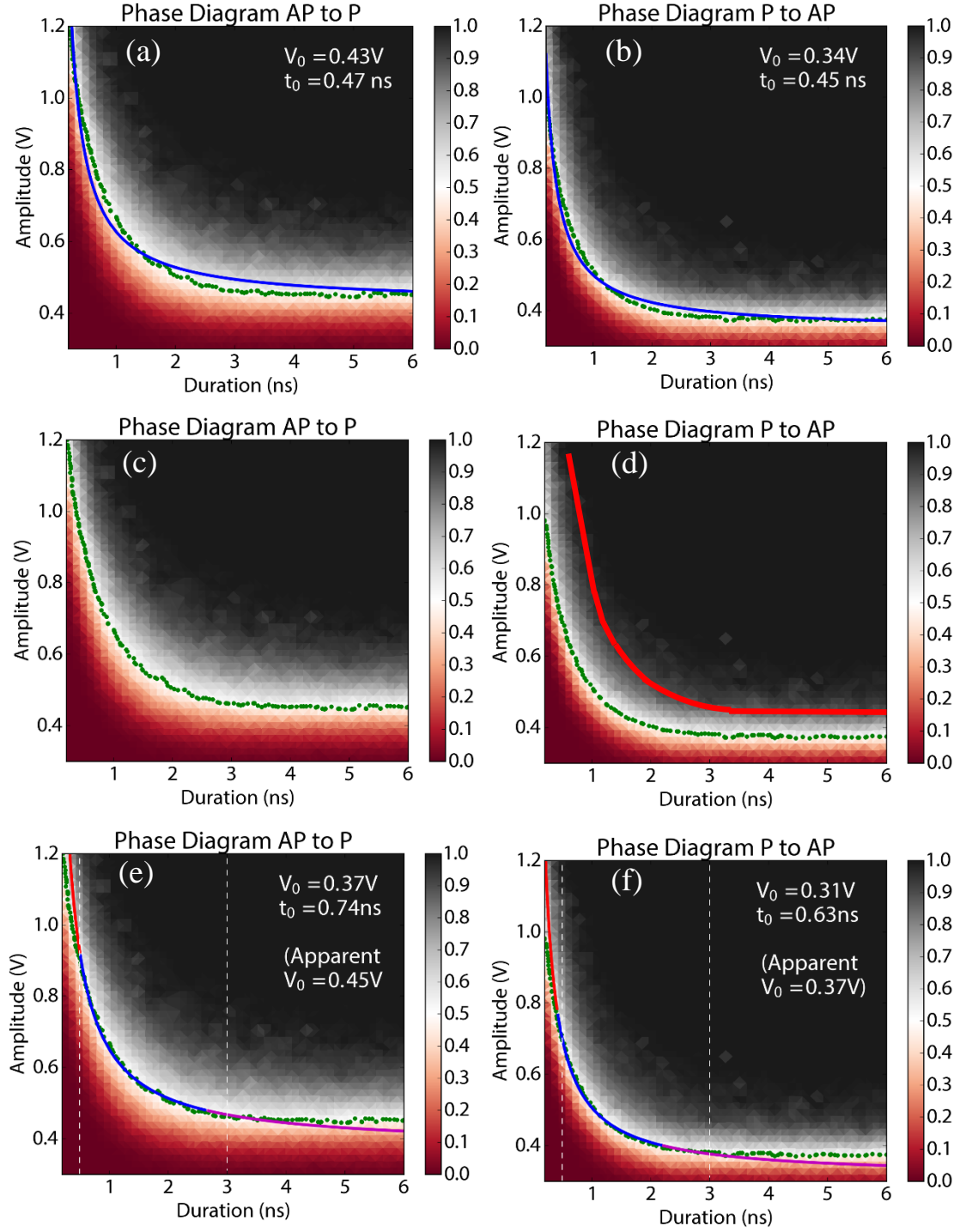


Fig. 6. 2 A typical set of switching phase diagrams of a Canon4-7 device. (a) and (b) show macrospin fit to the whole duration range. (d) shows an imaginary shift of the pulse curve upward for P→AP polarity which makes it look less asymmetric from AP→P in (c). (e) and (f) show the new fitting scheme that captures the same $V_0 \sim 2V_0$ regime for both polarities, regardless of the V_0 in each polarity. White dashed lines are guide to the eyes. For these devices, the $V_0 \sim 2V_0$ regime usually falls into 0.5 ns ~ 3 ns region.

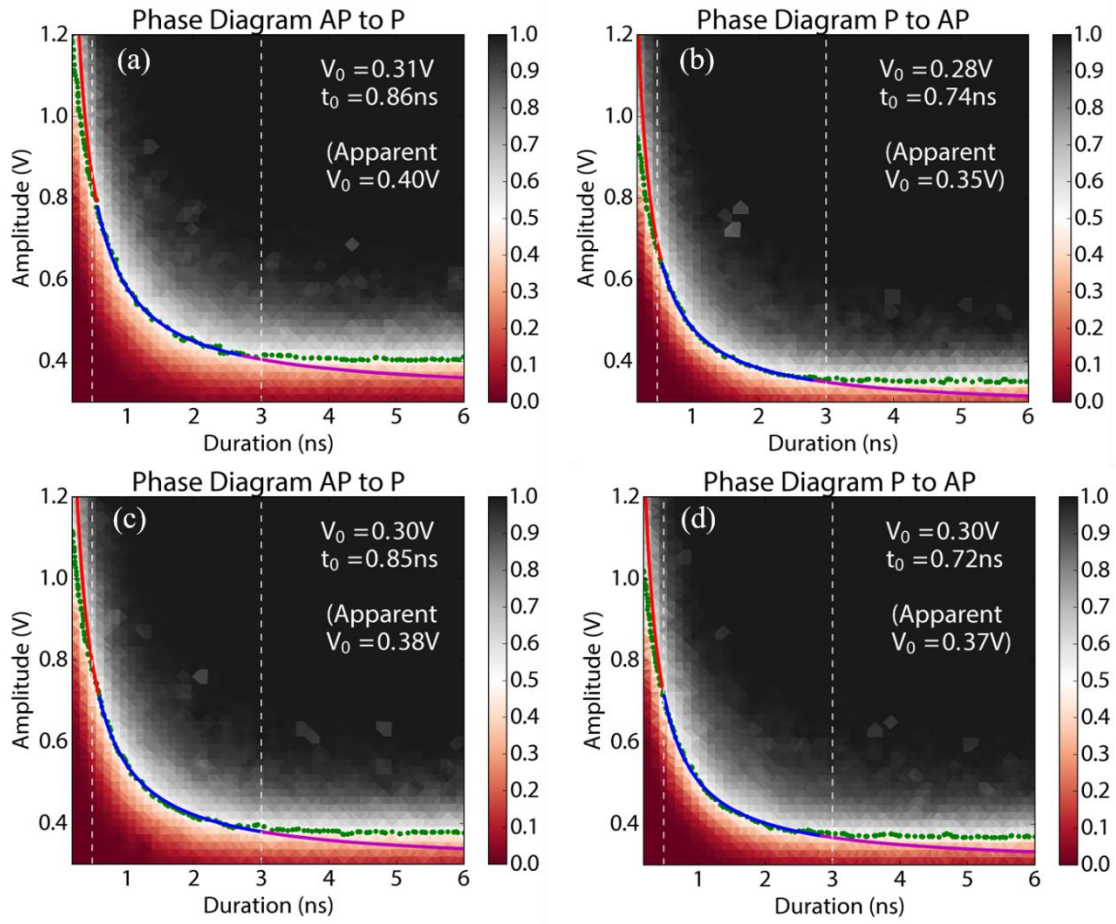


Fig. 6. 3 Switching phase diagrams of a Canon4-7 device with different offset field. (c) and (d) have an offset field of 4 Oe greater than (a) and (b), which effectively adjusted the symmetry of the two polarities. The new fitting scheme yield almost the same results regardless of the V_0 change.

Using this fitting method, we looked at MTJ devices with rectangle and triangle shapes. Table 6.1 summarizes the extracted switching voltages and time scales from the different shapes. From the symmetry analysis, the up and down triangles relative to the channel direction should be accounted for when the current polarity changes, if we assume a uniform channel and ideal positioning of the pillar on the channel. Thus the results shown in the table, which is averaged over three devices of

each type, indicate that the triangular shapes can be switched as fast as the rectangle devices in both polarities with slightly smaller t_0 's.

	AP→P			P→AP	
	V_0	t_0		V_0	t_0
Rectangle	0.327	0.783		0.270	0.787
Up Triangle	0.377	0.703		0.303	0.750
Down Triangle	0.363	0.697		0.287	0.780

Table 6.1 Critical switching voltage and time for MTJ devices with different shapes. Devices are kept at the same nominal area. Data shown is averaged over three devices of each type.

The distinct switching behavior at ultra-short pulse regime and medium duration regime may be the result of slightly different reversal mechanisms. Thomas et al. have reported that two-terminal spin transfer torque induced switching has two different aspects¹⁰⁵. The first is “propagation” which refers to a sharp increase of switching voltage at a short time scale and nucleation which refers to a more gradual decrease of switching voltage at longer time scales. Although our switching time scales are significantly shorter than studied by Thomas et al., it could be that at high drive amplitude multiple domains are nucleated quickly and the propagation of the switched domain governs the switching time scale. However, at lower pulse amplitude the switching is slower because first the energy barrier for nucleation of a single (or few) sub-domain(s) has to be overcome, which is then followed by the subsequent propagation of the domains.

6.2 Highly reliable SOT switching at short pulse durations

For this new memory technology to be applied in industry, we need to demonstrate both a high speed of operation and highly reliable switching, since both are crucial considerations¹⁰⁶. Different from STT-MRAM where the writing and reading pulses proceed through the same path, SOT devices do not suffer from endurance issues due to tunnel barrier wear/out or break-down or from the read disturbance, which leaves as the only reliability parameter the write error rate in device writing. We have shown in the previous section, that the short pulse switching remains fast and energy efficient when there is some variation of the shapes, which is a positive indicator for manufacturability. Here we check the reliability of these devices with different shapes by doing the write error rate (WER) measurement at various pulse durations. Figure 6.4 shows rectangle devices in black color, triangular devices in red and blue colors, with pulse durations at 1 ns and 500 ps. The steep decrease of the WER at the higher pulse amplitudes for the different shapes and pulse durations demonstrates the high reliability of the three terminal SOT devices for fast, reliable technological applications. My current results are limited by the highest pulse amplitude I can apply to the device due to the poor quality of the insulator around MTJ pillars, which should be readily improved in an industrial fabrication process. The small difference of WER behavior with different shapes also indicates that there is a high tolerance in lithography and/or ion beam etching in the device patterning, which again indicates good prospects for reasonable manufacturing margins.

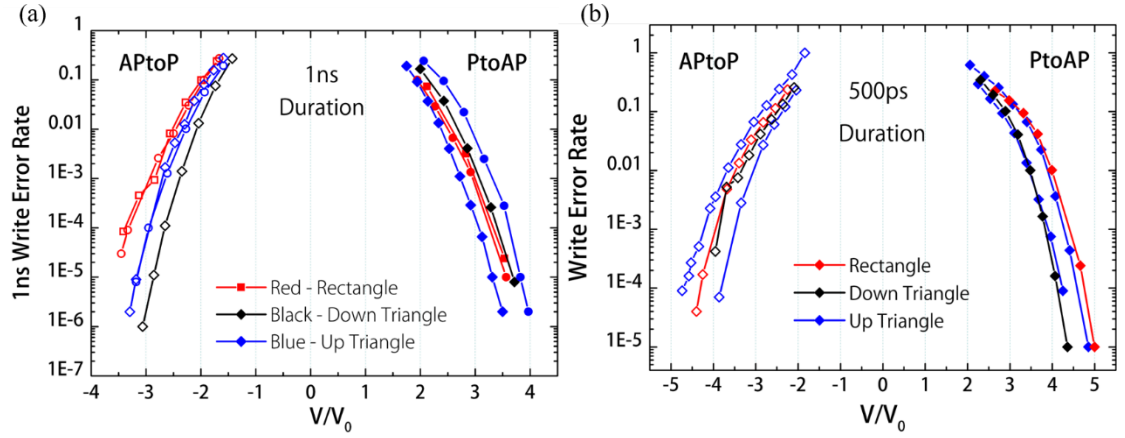


Fig. 6. 4 Write error rate measurement on different shapes at different pulse durations. WER has a steep decrease at large pulse amplitude regardless of the shapes and can reach 10^{-6} for both $P \rightarrow AP$ and $AP \rightarrow P$ polarities.

In the previous section, I had discussed the asymmetry of the two switching polarities and one of the possible reasons behind this phenomenon. Interestingly, by varying the offset field, I also observe a small difference in WER behavior as shown by Fig. 6.5. As is discussed above, by varying the offset field applied during the experiment, we can tune the V_0 's of two polarities and achieve almost the same critical voltage for switching in both directions. However, as the WER results are plotted against V/V_0 , which in theory removes the dependence on the actual V_0 , the WER shows a small transition from favoring $AP \rightarrow P$ (left branch, lower WER with blue data) to favoring $P \rightarrow AP$ (right branch, higher WER with blue data) as the field decreases from -21 Oe to -17 Oe. These results indicate that the external field has an extra effect on the switching dynamics besides tuning the critical voltage (current) which is simply shifting the current induced loop horizontally, making it favor $AP \rightarrow P$ or $P \rightarrow AP$ (see Fig. 6.1(b)). Note that the difference of the applied field is only 4 Oe, far less than the offset field needed to balance the two polarities. This effect is

possibly caused by the external field modifying the micromagnetic configuration of the device during the switching and could be more pronounced if the variation of the field is larger. Further exploration of this effect could potentially give more insights to our understanding of the SOT switching.

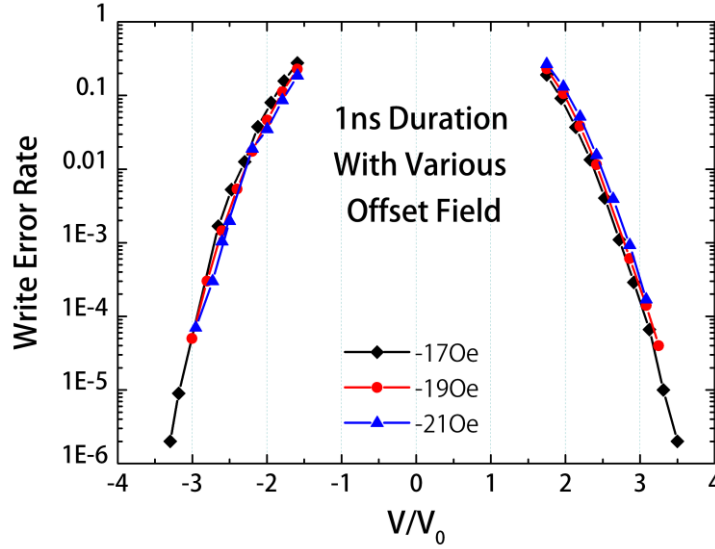


Fig. 6. 5 WER measurement on a Canon4-7 device with slightly different offset field. As the field is tuned, the switching transitions from favoring one polarity to the other.

Finally I tried to confirm the reliability of our SOT devices with a different wafer Canon4-3 which has the following stack structure Ta(1)-Pt85Hf15(4)-Pt(1)-Hf(0.3)-FeCoB(wedge,1.3-1.6)-MgO(RA=200)-FeCoB(1.2)-Ta(0.2)-FeCoB(1.2)-FeCo(1)-Ru(0.85)-FeCo(2.5)-IrMn(7)-Ru(4). We carried out WER measurements on devices of size $190 \times 75 \text{ nm}^2$ on 300 nm wide channels. Figure 6.6 show WER of two devices with the same nominal design. Similar behavior with WER $\sim 10^{-5}$ down to 200 ps pulse duration indicates that these SOT devices are very reliable in very short pulse switching, demonstrating the high feasibility of utilizing these structures in future cache memory applications. Note that these results are obtained using a pulse

generator that has distorted pulse shapes at pulses shorter than 1 ns, which slightly over-estimated the speed of the switching in these devices (see Chapter 4 for pulse shape comparison with different pulse generators). However, our results still show large improvement of the switching efficiency and reliability over other emerging memory technologies.

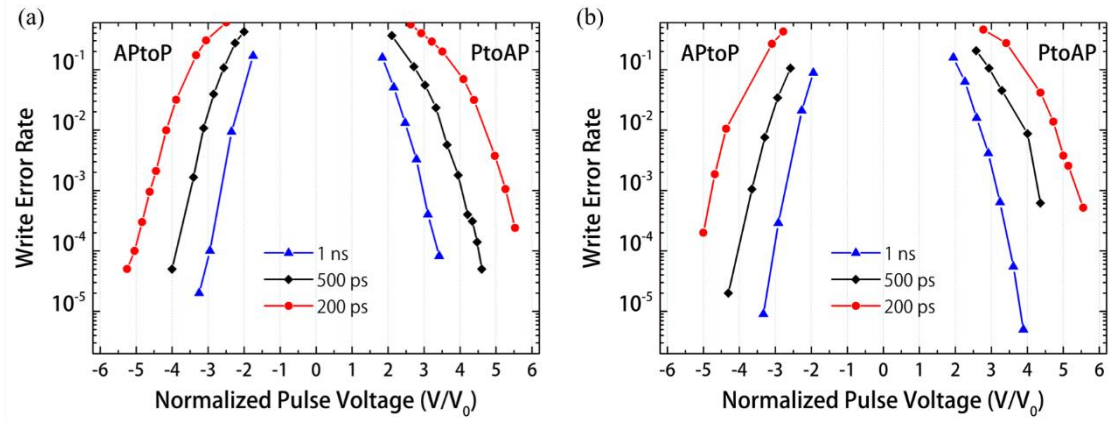


Fig. 6. 6 WER measurements on two different samples with the same nominal design, showing reliability of these SOT devices with WER $\sim 10^{-5}$ down to 200 ps pulse duration.

CHAPTER 7

VARIOUS NOVEL SWITCHING PHENOMENA IN IN-PLANE MAGNETIZED MAGNETIC TUNNEL JUNCTIONS

In this chapter I will briefly introduce a few novel considerations that could be affecting the detailed behavior of our 3T-MTJ devices. As I showed in the previous chapters the macrospin model that I use to describe spin-orbit-torque (SOT) switching serves as a good, first order description of these devices but is possibly neglecting some important micromagnetic details that may affect the short pulse switching behavior. By varying the size of the MTJ bits, engineering the profile of the pillar shape, and studying the MTJs with the magnetization collinear with injected spin polarization, I have attempted to develop some more insight into the details of SOT switching and its applications.

7.1. Size and shape dependence of the switching current of in-plane magnetized MTJs

For SOT switching of in-plane MTJs, as discussed in Chapter 5, the macrospin model predicts a zero-temperature critical current density

$$J_{c0} = \frac{2e}{\hbar} \mu_0 M_s t_{FM} \alpha (H_c + M_{eff} / 2) / \xi_{DL} \quad (11)$$

where e is the electron charge, \hbar is the reduced Plank constant, μ_0 is the permeability of free space, M_s is the saturation magnetization of the free layer (FL) and t_{FM} is the FL's effective magnetic thickness, M_{eff} is the FL's effective demagnetization field, and α is the effective magnetic damping constant of the FL. We notice that the

switching current density is proportional to the thickness of the FL but is not dependent on the area of the FL. This can be understood from the macrospin perspective that the total moment of the FL scales with the area of the FL, and the amount of the spin current that is injected through the HM/FL interface scales with the area of the FL in the same manner. Thus as long as one uses the same HM/FL system, the switching current density should not scale with the size of the FL. However, many works have shown that complicated micromagnetic dynamics exists and can greatly influence the switching behavior in the MTJs^{67,68,104}. Due to the limitations of the fabrication tools, it is evident that our MTJ pillar profile does not have sharp edges at the FL-channel corner. This tapering effect at the edges of the FL, as shown in the transmission electron microscopy (TEM) image in Fig. 7.1, leads to an increased contact area between the FL and the spin Hall channel, and could potentially change the magnetization configuration of the FL too³⁹. Here we vary the lateral size of our MTJs in our design and try to explore the dependence of the critical switching current on the MTJ size.

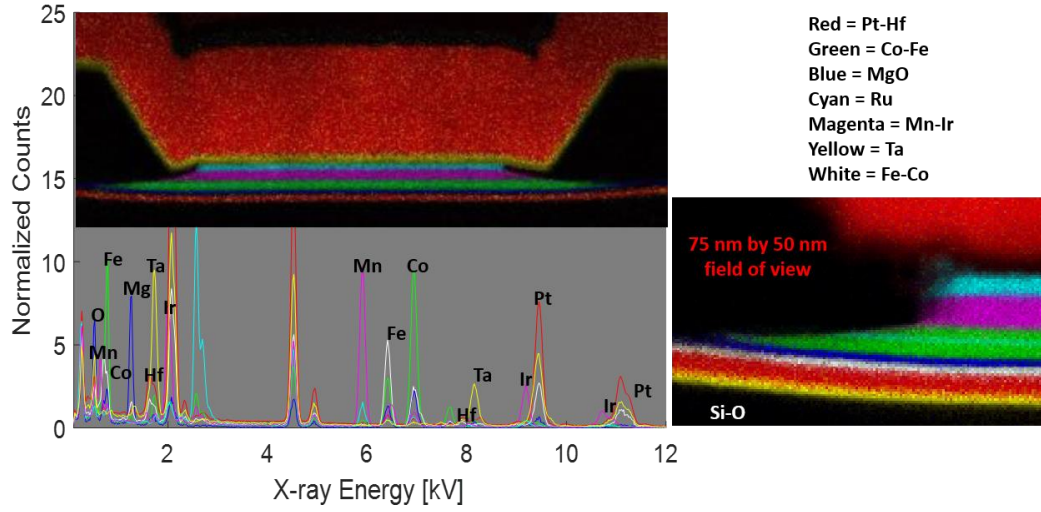


Fig. 7. 1 TEM image of an MTJ showing the cross section of the pillar with elements denoting materials in each layer. Instead of a sharp profile, a long tail of ~ 20 nm long at the bottom of the MTJ is observed, which causes the actual FL aspect ratio to be smaller than designed.

To do this series of switching experiments, I fabricated an MTJ stack grown by Canon Anelva, with the layer structure Ta(1)-Pt(5)-Hf(0.3)-FeCoB(1.4)-MgO(RA=50)-FeCoB(1.2)-Ta(0.2)-FeCoB(1.2)-FeCo(1)-Ru(0.85)-FeCo(2.6)-IrMn(7)-Ru(4) (hereafter called “Canon5-5”). Before patterning, the wafer was pre-annealed at 360 °C for 1 hour in a magnetic field of 1 T parallel to the longer axis of the to-be-patterned devices. I designed a series of devices having the sizes of 220×86 , 210×82 , 200×78 , 190×74 , 180×70 , 170×66 , 160×62 (dimensions in nanometers) on 300 nm wide channels. The size decreased within a die from the top (row1) to the bottom (row7). I first confirmed that the variation of the sizes was qualitatively consistent with my design after the full patterning. Figure 7.2 shows the MTJ resistance at each row within the die, with red points showing the AP state and black points showing the P state.

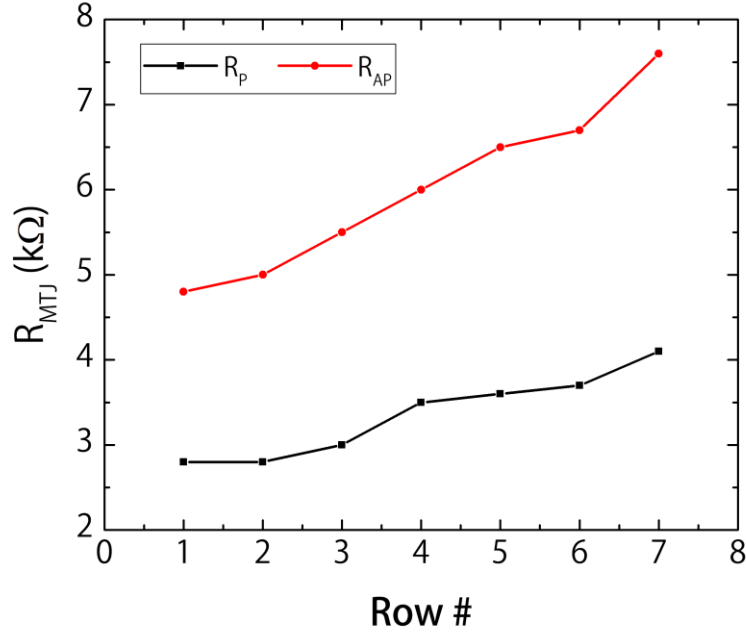


Fig. 7. 2 MTJ resistances at different sizes. Row 1 denotes the largest size $220 \times 86 \text{ nm}^2$ and row 7 the smallest $160 \times 62 \text{ nm}^2$.

A monotonic increase in the MTJ resistance with the row number for both P and AP states is seen. As the resistance-area (RA) product was kept constant across the wafer at $50 \text{ } \Omega \cdot \mu\text{m}^2$ as determined by the MgO tunnel barrier growth, the increase in MTJ resistance indicates the decrease in the MTJ area (size), consistent with our design. Note that Fig. 7.2 is a representative result of the size-varying design and other dies behave qualitatively the same way with minor differences in the baseline MTJ resistance.

I then carried out current switching measurements including ramp rate measurements to obtain the zero-temperature critical current of each MTJ size. Plotted in Fig. 7.3 is the trend of I_{c0} at different sizes. Each point on the plot is the averaged critical current from P→AP and AP→P polarities, and this number is averaged over a

couple devices with the same nominal size.

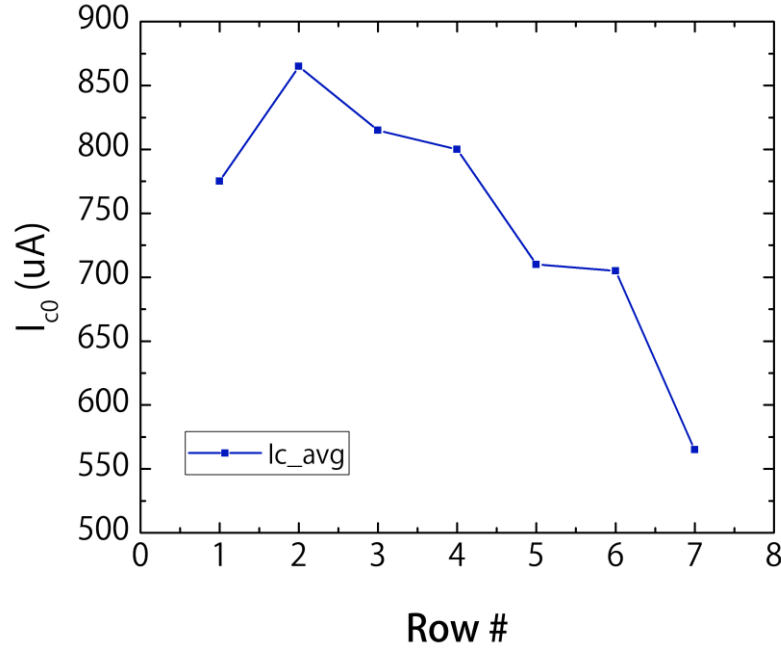


Fig. 7. 3 Zero-temperature critical current in MTJ devices with different sizes ranging from largest in row 1 to smallest in row 7.

From the data we see a clear decrease ($\sim 40\%$) of I_{c0} when the device size was decreased, although at the largest size the current was also slightly lower. As discussed above, this size dependence of the I_{c0} is not expected from the macrospin model of the switching and is likely related to the tapering of the FL edges in two ways. First, due to the taper there is a larger contact area between the FL and the HM which increases the amount of spin current injected into the FL compared to the ideal geometry. Also, because the top of the FL is closer to the designed size, we gain the advantage of larger spin current input and switch the device more efficiently. As the size of the device increases the taper naturally stops due to the limitation of the channel width and we get less advantage of the extra spin current injection, as shown by Fig. 7.4(a).

Second, as You et al. have indicated, the wedged shape at the edge of the FL could potentially induce an anisotropy that tilts the end somewhat out-of-plane³⁹ (Fig. 7.4(b)). Based on the switching model, the magnetization is excited to precession around the demagnetization field by the spin torque until the energy needed to switch across the saddle point is reached. With a larger volume of the FL that has the magnetization tilted somewhat out-of-plane initially, less energy is needed to activate the switching, resulting in smaller switching current. The decrease of the I_{c0} at the largest size could potentially be due to certain micromagnetic configurations that make the switching enter a different regime, which reduces the switching current. More data is needed to explore the switching behavior for devices with larger sizes but still confined on a narrow channel.

The decrease of I_{c0} at smaller MTJ sizes is advantageous for application as it improves the scalability of our devices. As the spin Hall channel is narrowed down for smaller devices, the switching current will decrease given the same switching current density. If the switching current density also scales with the size of the memory bit, we could potentially get a further reduction in write energy, which makes this approach promising for high density, low power memory applications.

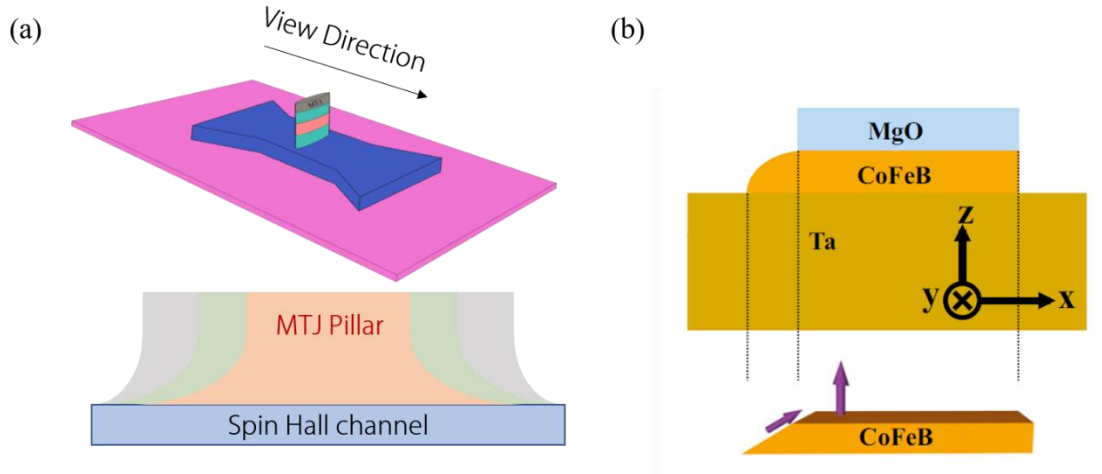


Fig. 7. 4 Possible explanation for the I_{c0} decrease with smaller MTJ sizes. (a), Larger devices has a smaller tapered area due to the limitation of the channel width. (b), Tapered region has tilted magnetic anisotropy, which helps the activation of the magnetization precession and switching. (Part (b) reproduced from Ref. 4)

Next, we describe another set of experiments that show new switching behavior that cannot be explained by the macrospin mechanism. As indicated from above, the area of the MTJ can significantly change the critical switching current, which is possibly explained by a micromagnetic configuration that leads to domain nucleation, expansion and propagation. This leads to the question of whether the geometrical shape of the devices can affect the switching behaviors. To explore that I designed a series of MTJ pillars with the same nominal area of $190 \times 75 \text{ nm}^2$, but with different shapes, namely rectangle, triangle, dumbbell and diamond, shown by the SEM images in Fig. 7.5. The MTJs are fabricated on 300 nm wide channels with the stack structure Ta(1)-Pt₈₅Hf₁₅(4)-Pt(1)-Hf(0.3)-FeCoB(wedge,1.3-1.6)-MgO(RA=200)-FeCoB(1.2)-Ta(0.2)-FeCoB(1.2)-FeCo(1)-Ru(0.85)-FeCo(2.5)-IrMn(7)-Ru(4) (hereafter called “Canon4-3”). The devices measured are un-annealed.

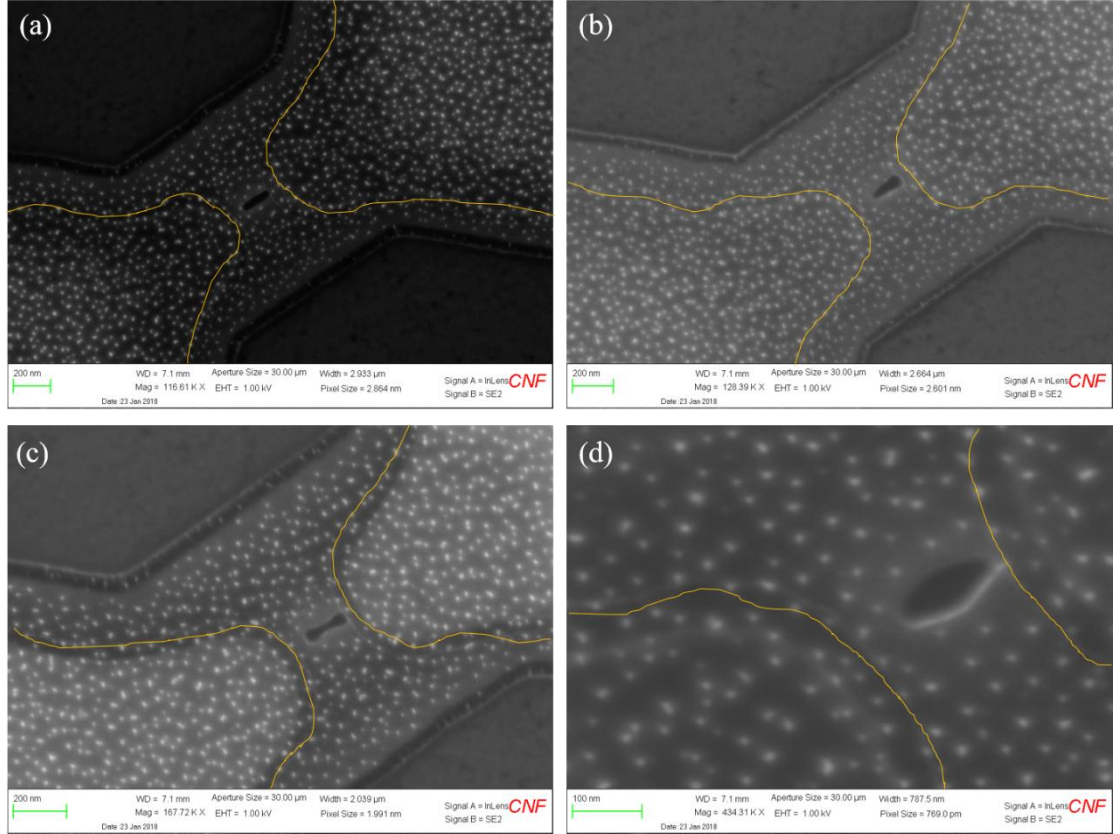


Fig. 7. 5 SEM images showing various shapes of the MTJ pillars with the same nominal area. (a), regular rectangle (b), triangle (c), dumbbell (d), diamond (Note that (d) has a different scale from the other three images. Yellow lines are channel contours as guide to the eyes.)

I carried out switching experiments on these various shapes and I summarize the results in Fig. 7.6. The numbers shown are averaged over a few devices for better statistics. First, notice that due to the wedged CoFeB free layer, the switching current on the left-hand side of the wafer is smaller than on the right mainly because of the lower M_{eff} of the FL due to the FL thickness variation across the wafer. From the FMR measurement taken on the un-patterned chips in the vicinity of the corresponding dies, we estimate that the $M_{\text{eff}} \sim 2750$ Oe for column 2 and 4220 Oe for column 7. The current reduction due to this decrease in M_{eff} is consistent with our macrospin analysis

in Chapter 5. Next, we compare devices within column 6 and column 7. We find that the triangular devices have slightly smaller I_{c0} than the rectangle devices within column 6, which has the same M_{eff} . In column 7, the dumbbell devices have a slightly larger I_{c0} than the rectangle devices, and the diamond devices have a 20% smaller I_{c0} than the rectangle devices. These results indicate that having a pointy tip at the end of the MTJ pillar can help reduce the critical current compared to having a large end of the pillar. This could possibly be explained by domain nucleation happening more easily with a smaller end of the pillar serving as a nucleation spot. Reports have also shown that the magnetization at the edge of a nanomagnet tends to align perpendicular to the edge¹⁰⁷, so in the triangular tip the magnetization could have more curling which would reduce the energy for nucleation. Thus with the small tips on the ends it is easier to nucleate a larger area of the domain which makes the switching more energy efficient. Based on these analyses, the switching current is mainly dominated by the initial stage of the spin current injection, which makes the diamond shape the most energy efficient geometry.

Furthermore, we confirm the results by plotting all the devices on the same plot (Fig. 7.7), with the horizontal axis defined as the MTJ resistance in the P state. Due to imperfection in the fabrication, we can get devices with slightly varying resistances (actual sizes) although they are designed to have the same nominal size. When we plot all the nominally identical devices on the same graph, we see an upgoing trend of I_{c0} at lower P resistances (in other words, larger device sizes), which qualitatively follows the results and analysis from the first part of this section. Besides that, we see a clear difference between rectangle devices and diamond devices, with

diamond devices having $\sim 20\%$ smaller I_{c0} than rectangle devices.








Thicker Free CoFeB Layer		
$M_{\text{eff}} \sim 2750 \text{ Oe}$		$M_{\text{eff}} \sim 4220 \text{ Oe}$
Col2	Col6	Col7
Rect 190x75	Rect 190x75 Up Triangle Down Triangle	Rect 190x75 Dumbbell Diamond
 285 μA $\Delta \sim 54$	 455 μA $\Delta \sim 93$	 520 μA $\Delta \sim 83$
	 415 μA $\Delta \sim 66$	 530 μA $\Delta \sim 85$
	 410 μA $\Delta \sim 74$	 440 μA $\Delta \sim 73$

Fig. 7. 6 Comparison of the critical switching current in various shaped MTJs with the same nominal size.

We also notice that the dumbbell devices, as shown in column 7 of Fig. 7.6, have the largest I_{c0} , which, from another point of view, confirms that the geometry for the domain nucleation is critical⁶². From the averaged results, there is also a slight trend of thermal stability reduction in the geometries with sharp ends, which could be due to these special shapes having a weaker shape anisotropy, which results in the lower H_c , thus reducing the energy barrier for the switching. However, for room temperature (and/or low temperature) applications, Δ of 80 is higher than needed, which means that by changing the shapes we reduce the excessive Δ but gain the

advantage of lower switching current in these in-plane magnetized MTJs.

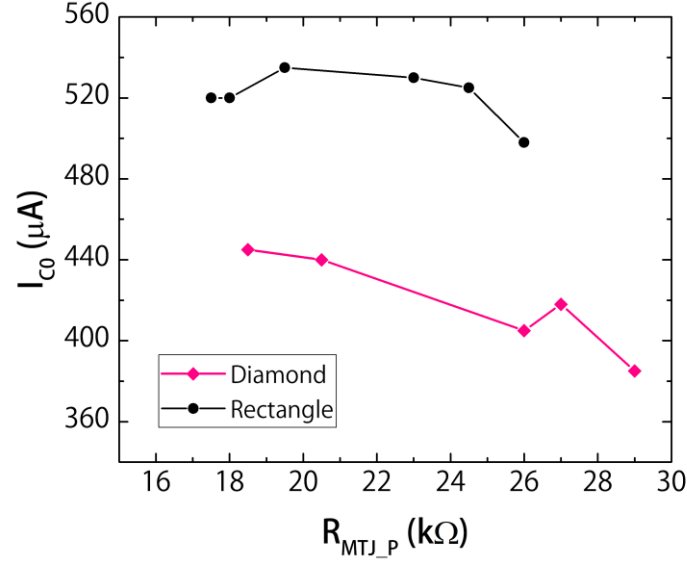


Fig. 7. 7 Comparison of rectangle and diamond devices with slightly varying sizes.

7.2 Switching of MTJs with an easy axis parallel to the spin Hall channels

In the current SOT switching scheme, the MTJs are placed on the spin Hall channel with the longer axis perpendicular to the current flow direction in the channel to utilize the anti-damping torque from the spin current. Some argue that an obstacle for scaling down these three terminal MTJs is the high aspect ratio of the pillars needed to provide the coercivity and thus the thermal stability Δ of the device, although the three terminal, two transistor aspect of the device is the largest contributor to the device footprint. To have high enough Δ , the longer axis of the pillars needs to be 3 ~ 4 times of the shorter axis, depending on the fidelity of the ion beam etching (degree of tapering) and this places a limit on the width of the narrowest channels one can make. One alternative switching scheme³² is to place the longer axis

of the MTJ pillars parallel to the spin Hall channel so that we can scale down the channel to just the width of the MTJ pillars, which in our current design, could potentially be less than 50 nm wide. However, due to the directions of the torques created by the spin current, in this scenario the switching is driven by the effective field exerted by the incident spin current rather than by the anti-damping torque. In that case, similar to the SOT switching of a PMA device, an external field is required to break the symmetry and give deterministic switching³². In this in-plane magnetized case the bias field has to be out-of-plane rather than in-plane as for the PMA device. In this section, I will introduce my recent work on designing and measuring MTJs with this “orthogonal” or x-type geometry.

I show a typical device of size $190 \times 45 \text{ nm}^2$ on a 300 nm channel with the Canon4-3 film structure. Field switching minor loop and current switching loops are shown in Fig. 7.8. The square, abrupt switching of the FL by external field is similar to the regular, “collinear” devices which have the injected spin polarization collinear with the easy axis direction. Although the orthogonal devices may have a different tapering situation as the geometry is rotated by 90° compared to the collinear devices, they show robust coercive field of $\sim 50 \text{ Oe}$. When we apply an electric current along the channel and an external field in the z direction of $\pm 1200 \text{ Oe}$, we observe switching of the FL in two opposite polarities unique to the direction of the external field, as shown by the red and blue data in Fig. 7.8(b). Different from a previous report³², a large field ($\geq 500 \text{ Oe}$) is required to generate clean two-way switching in these devices. At smaller field, we either do not observe the switching or the switching is partial or non-abrupt.

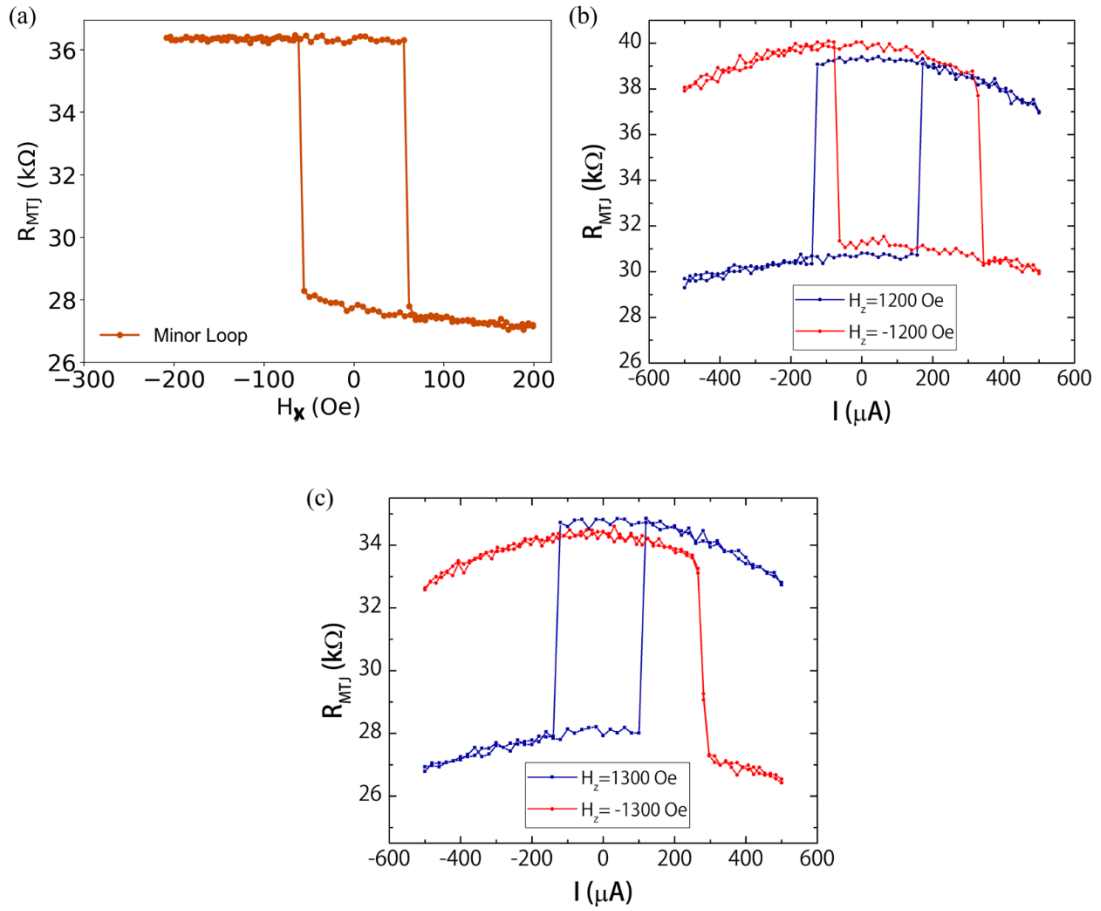


Fig. 7. 8 Field switching minor loop and current induced switching with out-of-plane external field in an orthogonal device.

We then try to apply the external field with different magnitudes and observe how the switching behavior changes with field. Surprisingly, we see a continuous change of the current switching loops which gives larger current as the field is decreased even below the threshold field we mentioned above. As we reduce the field to zero (magenta, dashed line) and even reverse the direction (black line) as shown in Fig. 7.9, we still obtain full switching of the FL, which does not follow the simple symmetry analysis. I conclude that there is a history effect in this special geometry

which is not observed in the collinear type devices. It is possible that due to the large z-direction field we apply during the initial switching, some magnetic domains are trapped in an excited energy state that helps the next switching attempt with a lower external field. This could explain the fact that we observe zero-field switching when we gradually decrease the external field while no zero-field switching can be observed if we start the switching attempt with a new device on the same chip without first ramping up to high fields. Another point that is worth attention is that in these structures with a FL of 1.4 nm, the in-plane anisotropy, M_{eff} is on the order of 3000 Oe, which is only about three times higher than the external field that we apply. Thus, the applied field could be of significant influence on the current induced switching. For example, in Fig. 7.8(c) where an external field of ± 1300 Oe is applied, the current switching loop for one polarity of the out-of-plane bias field shrinks to zero hysteresis, and both switching steps, P to AP and AP to P, happen on the same positive current side. This could be due to the applied field being too strong that interferes with the effective field from the spin current to switch the FL.

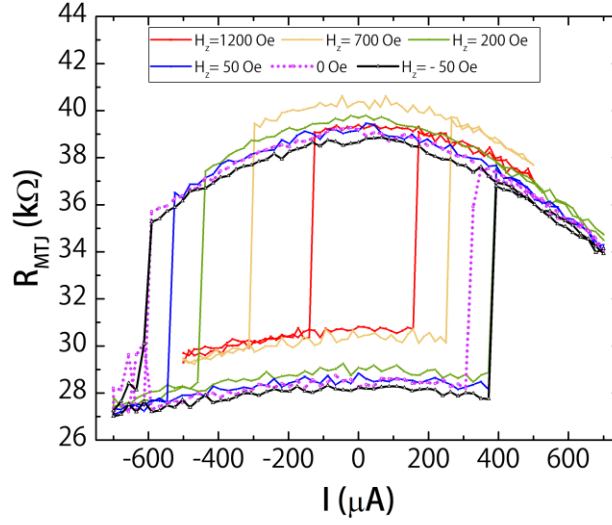


Fig. 7. 9 Current induced switching in an orthogonal device with different applied external field. The device can be switching at zero field and even at opposite field that would otherwise give switching in an opposite polarity.

As I have shown in previous chapters, the MTJs with collinear geometry show sub-nanosecond switching with high reliability. I tried to explore the pulse switching behavior of these orthogonal devices and compare it to their collinear counterparts. As an example I show results from a device of size $190 \times 45 \text{ nm}^2$ on a 300 nm channel, with an applied field in the positive z direction $H_z = 1000 \text{ Oe}$. Figure 7.10 shows the switching probabilities for two polarities $P \rightarrow AP$ and $AP \rightarrow P$ with various pulse amplitudes and durations. With this large external field, we observe a fast rise of switching probability of both polarities especially for $P \rightarrow AP$. Consistent with the change of current switching loops under different fields, the pulse switching behavior also shows some field dependence, which is shown in Fig. 7.11 with $H_z = -1200 \text{ Oe}$, -1000 Oe and -900 Oe . When the field is decreased, the low pulse amplitude performance starts to degrade, which indicates that the threshold for switching has

increased, similar to the increased switching current in the DC measurements. These results show that the orthogonal devices can be switched fast and efficiently with large applied field, provided that this bias field it is not too large to interfere with the micromagnetic dynamics during the switching process.

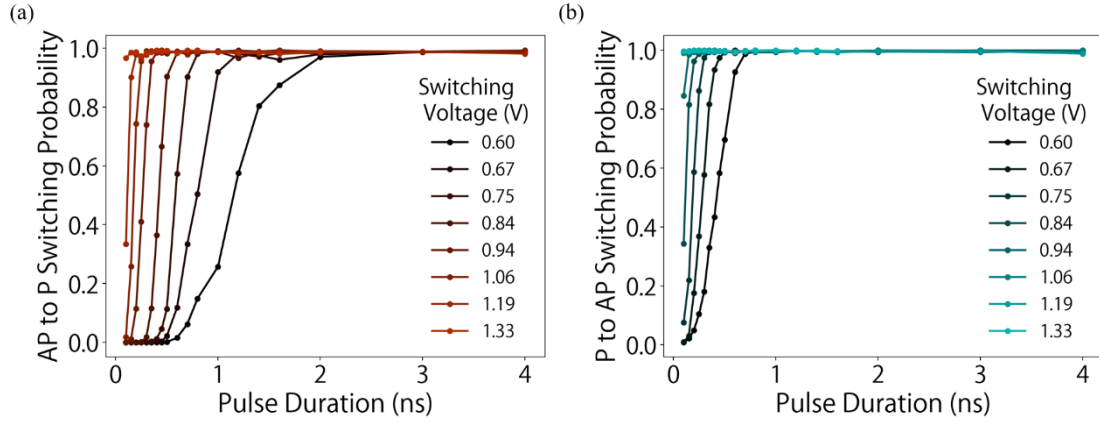


Fig. 7. 10 Pulse switching probability of an orthogonal device ($190 \times 45 \text{ nm}^2$) with an applied external field $H_z = 1000$ Oe.

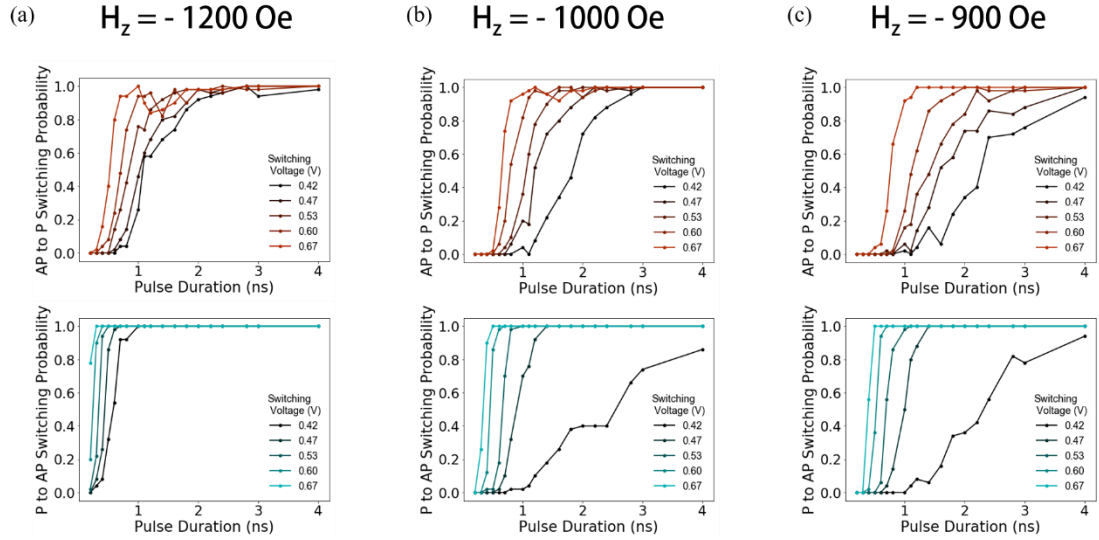


Fig. 7. 11 Pulse switching behavior of an orthogonal device with different applied z field.

I extracted the characteristic switching time and critical switching voltages

from the orthogonal device discussed above and compared to a collinear device fabricated on the same wafer with the same dimensions. In Fig. 7.11 we plot the data on the same graph with red curve showing the behavior of orthogonal device and the blue curve showing the behavior of the collinear device. At the longer time scales the switching voltage for both types of the devices is inversely proportional to the switching time as predicted by the macrospin model. However at shorter time scales both types show a critical voltage scale that is smaller than the prediction of the macrospin model. The orthogonal devices are more efficient in the shorter time scale compared to the collinear ones, which is similar to the results reported by Fukami et al.³² However, further study is needed to explain the discrepancy of the reported external field scales required to assist the deterministic switching. A key question is whether this requirement for a bias field for the orthogonal devices can be eliminated, or at least greatly reduced, while still achieving reliable, fast switching with this geometry. At this point the history effect that I have observed in my version of these devices indicates a potential problem with non-uniformities due to magnetic hysteresis that, until eliminated, could be a major obstacle for reliable applications of this device approach.

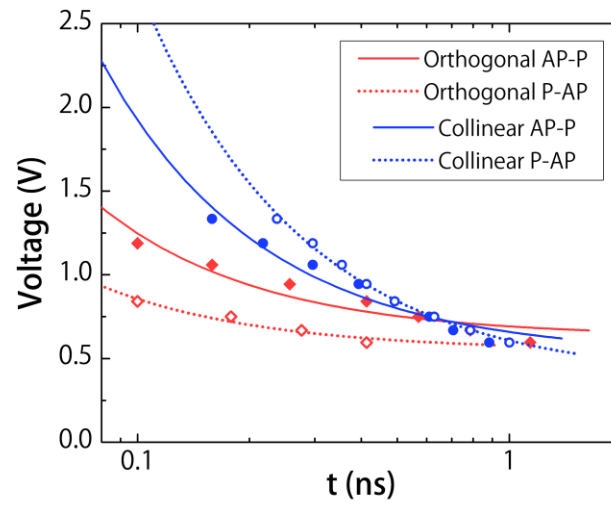


Fig. 7. 12 Comparison of fast pulse switching characteristics between orthogonal devices and collinear devices.

CHAPTER 8

CONSTRUCTION OF HIGH FREQUENCY LOW TEMPERATURE MEASUREMENT SYSTEM AND THE SWITCHING BEHAVIOR OF MTJS AT LOW TEMPERATURES

In this chapter I will describe the set-up of a high frequency, low temperature measurement system and some switching behavior of our MTJs both in the thermally activated regime and the short pulse regime.

8.1 High frequency low temperature measurement system and its operation

Besides room temperature applications, there can also be rich physics in spin orbit torques at low temperatures, and spin torque SHE devices can possibly be beneficial to low power, exascale cryogenic computing. In order to probe the switching behavior of the MTJs at below room temperature, a new measurement system based on an existing Janis continuous flow cryostat was designed and constructed. It supports high frequency (GHz) probing of the MTJ switching as well as DC and FMR measurements. The constructed sample positioner that is inserted into the cryostat is shown in Fig. 8.1.

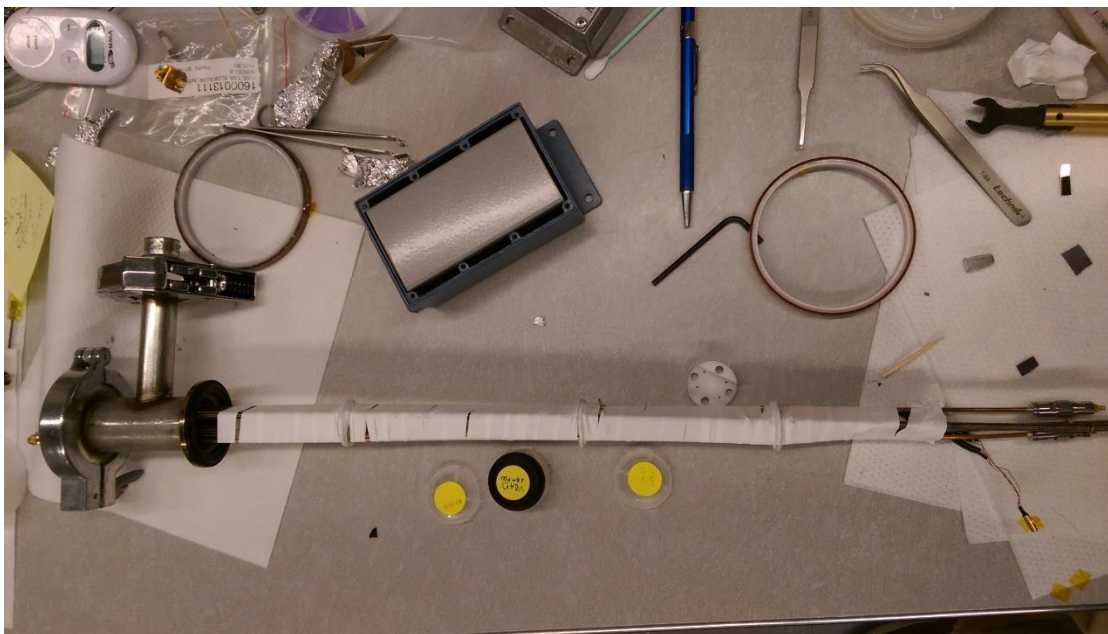


Fig. 8. 1 A picture showing the details of the high frequency sample positioner for low temperature measurements

There are two RF SMA type connectors are secured by two sets of nuts on the top plate of the sample positioner. They are connected to the bottom sample stage through two regular RF cables. To prevent the cables from oscillation and motion during the cooling, four circular Delrin baffles are placed at even distance from the top to the bottom (Fig. 8.2). The baffles have two holes on the edges where the two steel rods can go through as the support of the sample positioner. There are two groves cut into the baffles where the RF cables fit in. The baffles are oppositely oriented to each other so that the opposite direction of the groves give steady support to secure the cables in place. The position of the baffles along the vertical direction can be adjusted by turning the low profile nuts up and down to allow for better positioning of the cables.

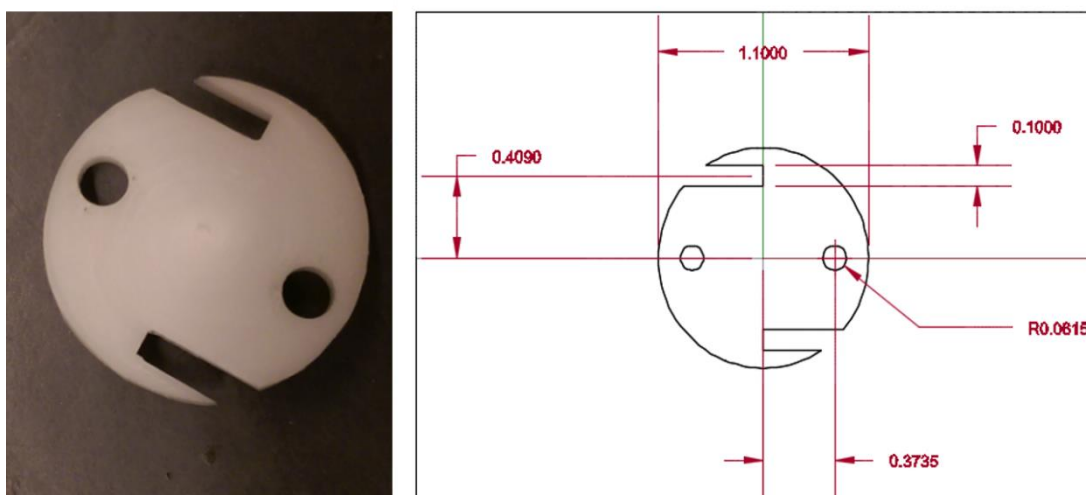


Fig. 8. 2 Delrin baffles used to hold RF cables in place

At the bottom of the sample positioner a customized sample holder is designed and machined using the same material Delrin (Fig. 8.3). In the center of the sample holder sits a high frequency gold plated waveguide, which is secured by brass screws and nuts. It is critical to use non-magnetic material to reduce any possible interference on the measurement. Two SMPM connectors are soldered onto the waveguides rigidly using solder paste with subsequent heating. They are connected to the RF cables through SMA to SMPM adapters on the end of the cables. There are various types of waveguides with different hole sizes in the middle for different sizes of the samples. The FMR waveguide does not have a hole since it does not require electrical contact from the sample to the waveguide.

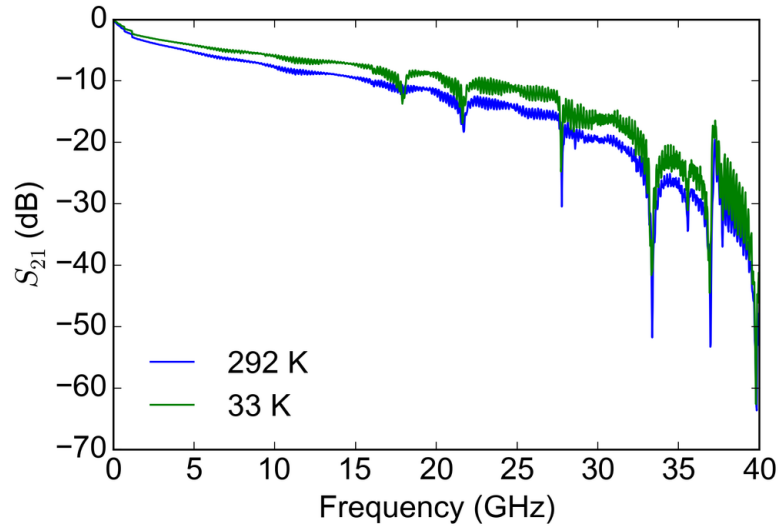


Fig. 8. 4 Transmitted signal at room temperature and low temperatures at different frequencies

The sample of interest is placed in the hole of the waveguide and secured using double sided tapes. In the case of the FMR measurement, the sample is placed upside down with the magnetic stack facing downward and four corners glued down on the waveguide using cement glue. The devices on the sample are wire bonded to the corresponding signal and ground lines of the waveguide using a West Bond 747630E wire bonder. A typical bonding schematic for an MTJ sample is shown in Fig. 8.5. Note that the MTJ device is exaggerated in size for clarity of the illustration. During wire bonding it is crucial to ground the sample to avoid static charge destroying the device.

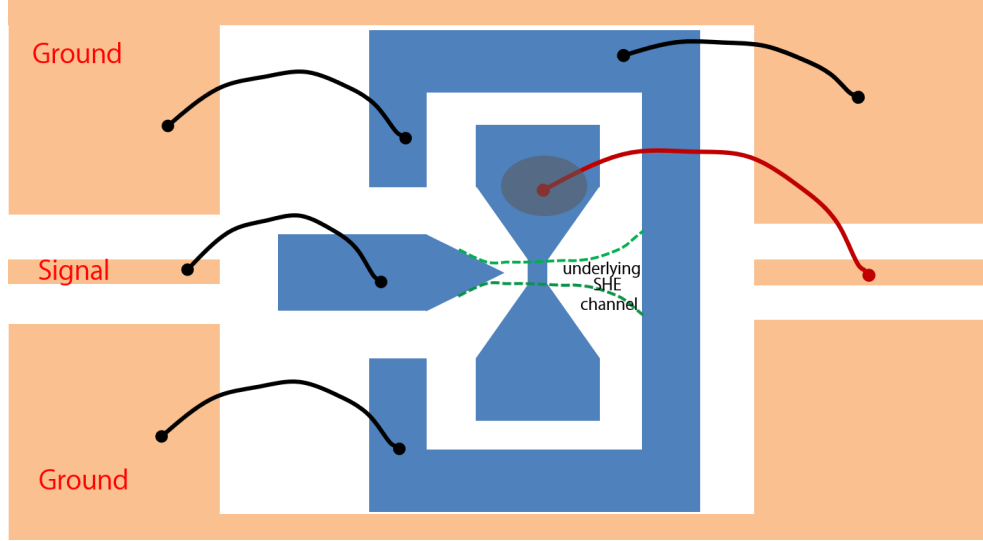


Fig. 8. 5 Bonding diagram for MTJ samples on high frequency waveguides

To use the measurement system, we take a liquid helium dewar and use a transfer line to transfer helium into the cryostat through an extended helium inlet. Two temperature sensors are connected to the temperature controller (Lakeshore 332). One GaAlAs sensor A is built in on the vaporizer stage which is at the bottom of the cryostat where liquid helium comes down and is vaporized by the heater on the same stage. Typically, we control the temperature of the system using the feedback from sensor A since it is next to the heater and can be more easily tuned. The other Cernox sensor B is inserted on the sample holder beside the waveguide. This is the sensor that measures the temperature of the sample more accurately due to the closer distance. Both feedthroughs for the sensors are located on the top part of the cryostat with the same type of the connectors. Two helium recovery lines are inserted into the top of the cryostat and the helium dewar to collect helium for re-process and re-use. When inserting the transfer line into the helium dewar, the pressure inside the dewar will

increase due to vaporization of the helium inside the dewar. Usually a pressure of ~5 psi is enough to pump liquid helium into the cryostat and no high-pressure helium gas is needed to assist. The cooling efficiency increases at lower temperatures so as soon as we get the transfer to go at the beginning, it will be good for the rest of the measurement. There is a needle valve on the transfer line that is used to control the amount of the helium flow into the cryostat. We need to keep the flow steady and not so fast in order to protect samples from flying out from the waveguide. At the end of the measurement we release the excess pressure in the dewar through the recovery line and pull out the transfer line at relatively low pressure (1~2 psi).

8.2 Field switching behavior and DC current induced switching at low temperatures

First I studied the field switching behavior of the MTJs grown at Cornell using the AJA sputtering system. The stack structure was as follows, Ta(1)-Pt(5)-Hf(0.5)-FeCoB(1.6)-MgO(1.6)-FeCoB(2.4)-IrMn(10)-Hf(1)-Ru(4) (numbers in parentheses are thicknesses in nanometers, the stack is hereafter called “IrMn-pinned sample”). The 10 nm IrMn is an antiferromagnetic pinning layer, which, by thermal annealing, can lock the thick FeCoB reference layer in place (under small applied field) and thus allows the reversal of the free CoFeB to achieve P and AP states of the MTJ. The samples are annealed in a vacuum furnace at 275 °C for 1 hour. In Fig. 8.6, we show major magnetic loops done on an example device with temperatures from room temperature to 100 K.

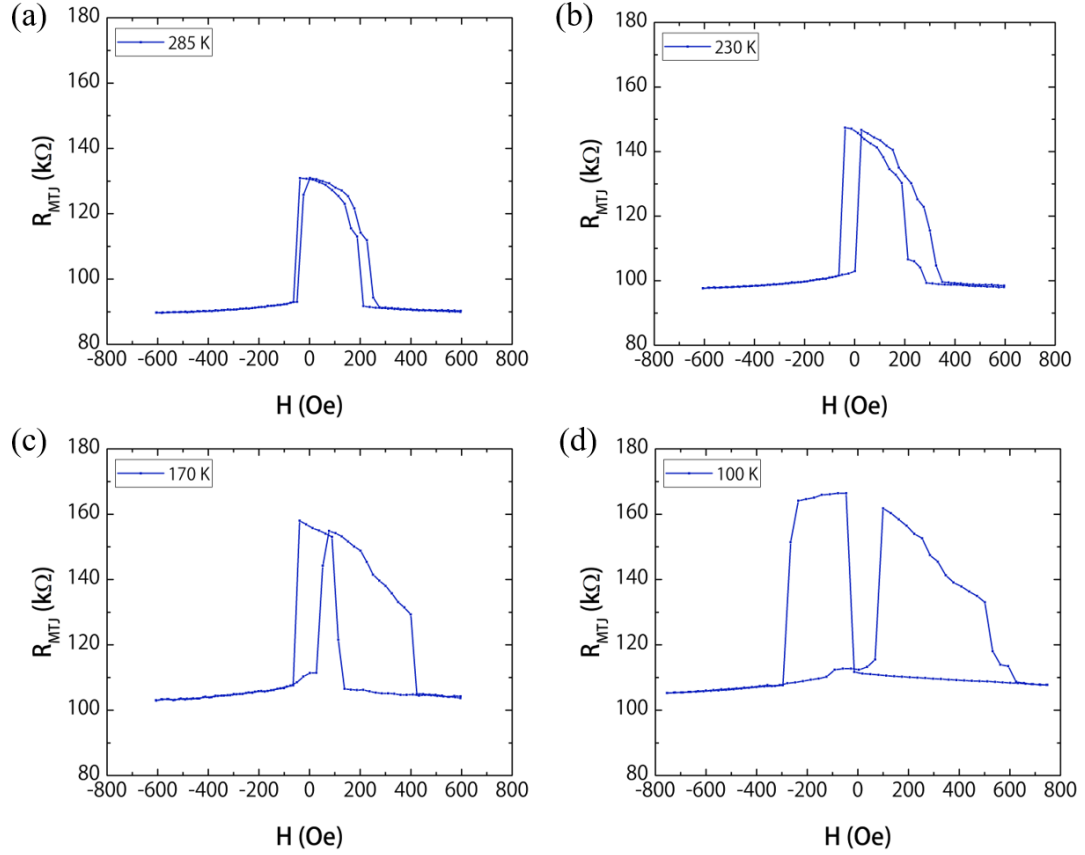


Fig. 8. 6 Major magnetic loops of an IrMn-pinned sample from room temperature to 100 K

As indicated by the MTJ resistance scale, both the P and AP resistance increases and with a larger increase in AP state, the TMR increases from 44% to 57%. The increase is consistent with results reported on similar MgO-based MTJs^{27,108–111}. At 285 K, due to the relatively strong pinning, the two abrupt reversals at negative fields show the switching of the free layer while the gradual switching on the positive field side shows rotation of the reference layer with external field until a point where the applied field overcomes the exchange field and reverses the reference layer.

As the temperature decreases, we can see the widening of the loop on the positive field side as well as the appearance of abrupt reversals for the reference layer,

which indicates that the pinning is gradually lost at lower temperatures. Although exchange coupling has been shown in many systems to increase with lower temperatures^{112,113}, it could be sensitive to film roughness due to its interfacial nature. When the temperature further decreases, as shown in Fig. 8.7, the TMR keeps increasing as expected, while the magnetic pinning keeps getting worse. The measured curves are repeated twice to show reproducibility. Moreover, non-uniform states start to show up which is manifested by the increasing curvature before the abrupt switching of the free layer and intermediate resistance states during the reference layer reversal. These behaviors are likely due to the poor film uniformity and defects in the magnetic layers, which are less frequently seen in devices grown in a Canon Anelva tool (discussed in the next part).

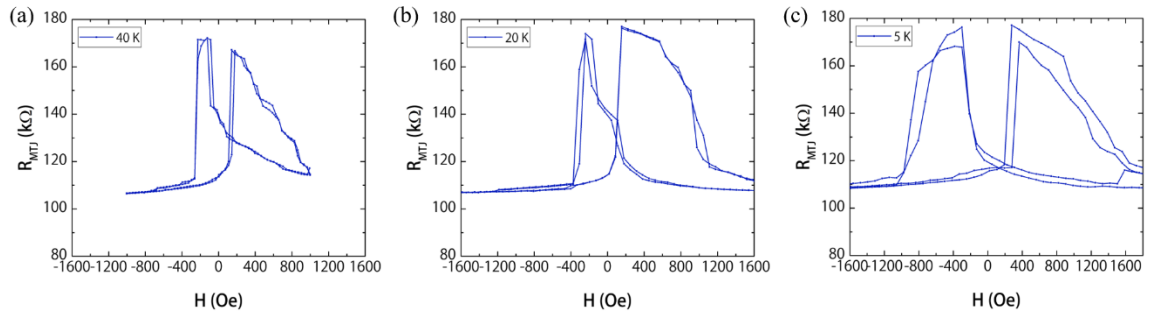


Fig. 8. 7 Major magnetic loops of an IrMn-pinned sample from 40 K to 5 K

Apart from the changing behavior of the reference layer (pinning layer), we observe a change in the free layer behavior too. Figure 8.8(a) shows a comparison of minor magnetic loops at different temperatures, which shows the free layer reversal and gives coercive field at different temperatures. As expected from a thermal activation model, the apparent coercive field, which is mainly governed by the shape anisotropy in the amorphous FeCoB layer, increases as the temperature decreases.

This is consistent with results reported on various magnetic structures with both in-plane and out-of-plane anisotropy^{114–116}. A single domain model has been raised to

explain the increase in H_c at lower temperatures, predicting $H_c = H_{c0} \left[1 - \left(\frac{T}{T_B} \right)^{1/2} \right]$,

where H_{c0} is the coercive field at 0 K, and T_b is the blocking temperature^{114,117}.

However, in our systems the increase is also possibly due to the thermal fluctuation being frozen out at lower temperatures, suppressing the random domain nucleation at lower external field, which would rather give a smaller switching field. At lower temperatures, the observed H_c approaches the intrinsic anisotropy field of the in-plane magnet.

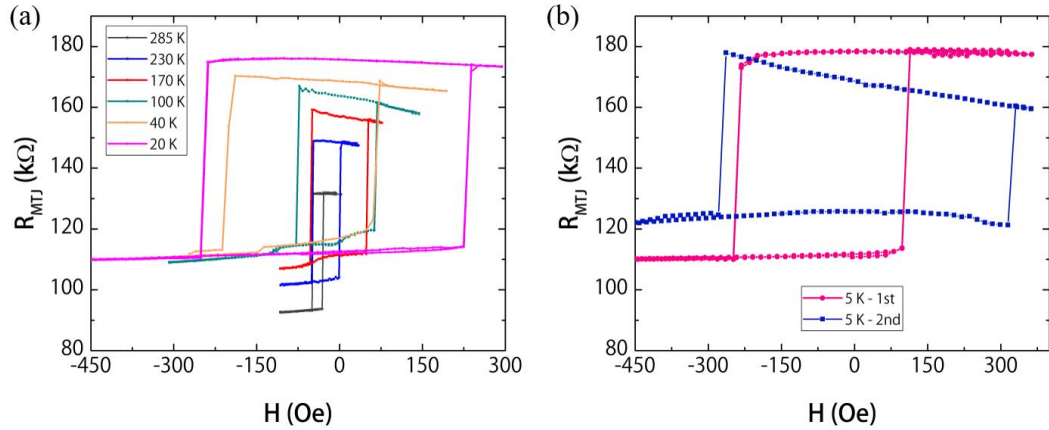


Fig. 8. 8 Minor magnetic loops of an IrMn pinned sample at low temperatures

I found that at very low temperatures (≤ 10 K), the CoFeB free layer can be trapped in some intermediate state where the P state resistance is higher, and the hysteresis loop seems distorted (Fig. 8.8(b)). This is again likely related to the non-uniform property of the magnetic layers that causes domain reversal to be sporadic and history-dependent.

Next, I show current switching behaviors of this MTJ structure at various temperatures. As indicated in Fig. 8.9, DC current needed to switch the free layer starts with a small value of around 100 μA due to the small coercive field at close to room temperature. Then it starts to increase almost linearly as the temperature decreases. However, the increase of the I_c slows down at below 50 K and almost reaches a steady value of around 950 μA at below 10 K. In Fig. 8.9(b) we show the change of $2H_c$ (full hysteresis loop width) and I_c with the change in the temperature. Although the coercive field increases continuously with lower temperatures, the switching current saturates below 10 K. The initial increase in the switching current is due to the larger energy barrier to overcome caused by increased coercive field and meanwhile suppressed thermal activation. However, as it reaches very low temperatures the current needed to switch the free layer becomes high, which effectively induces much more heat in the sample due to current flowing in the channel. This current induced heating raises the temperature to above the measured temperature and thus causes thermal fluctuation to become dominant again, giving a saturation-like behavior.

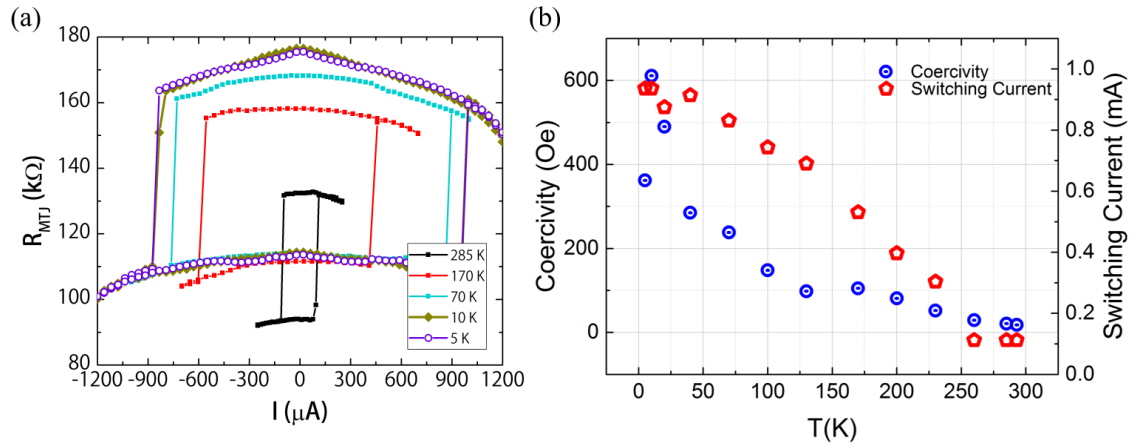


Fig. 8.9 DC current induced switching of an IrMn pinned sample at various temperatures

To gain more insight into the low temperature behavior of the Pt-based MTJs, we patterned a different stack structure grown by Canon Anlewa with full SAF and IrMn pinning layers. The structure is as follows, Ta(1)-Pt(5)-Hf(0.7)-FeCoB(1.6)-MgO(RA = $800 \text{ } \Omega \cdot \mu\text{m}^2$)-Pinned Reference Layer-Capping Layers. The device is a large device with nominal size of $390 \times 110 \text{ nm}^2$ and is annealed in an air furnace at 360°C for 1 hour (Hereafter called “Canon Large 1”). Due to the optimized MgO crystallization developed by Canon, the TMR is significantly higher in these samples, reaching 160% as shown by Fig. 8.10(a). The temperature dependence of TMR is qualitatively consistent with the calculation based on the Bloch model that predicts a $T^{3/2}$ dependence of magnetization M_s ^{109–111}. Similar to IrMn-pinned samples, Canon Large 1 also shows a monotonic increase in coercivity as temperature decreases (Fig. 8.10(b)). The critical current also shows a dramatic increase at the beginning of the cooling but saturates below 200 K, where the current reaches 1.07 mA.

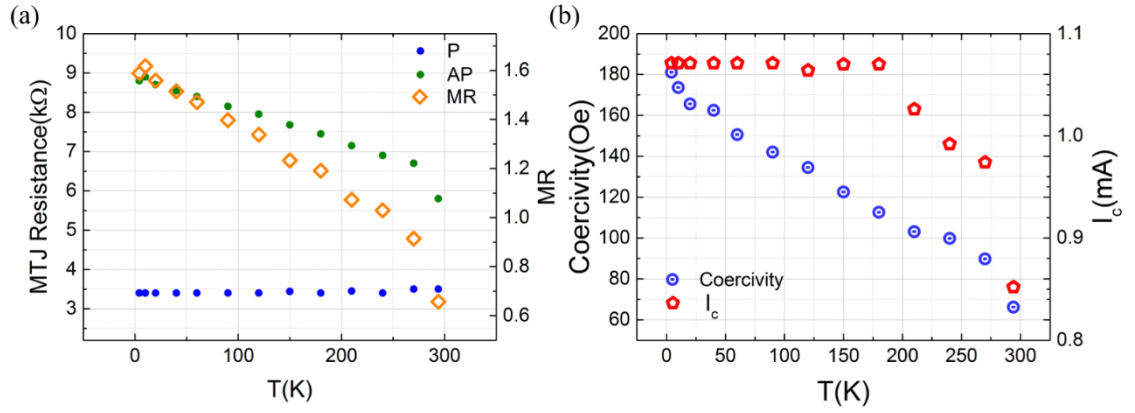


Fig. 8. 10 Temperature dependence of TMR, coercivity and switching current of a Canon Large 1 device

The saturation of the switching current due to heating can be qualitatively confirmed by measured channel resistance change at different temperatures. Figure 8.11 shows that the channel resistance of the device decreases as temperature goes down, as expected from an electron-phonon scattering picture of metal resistivity. However, as the temperature keeps decreasing, the curvature of the channel resistance vs. I increases, which indicates that at lower temperature, the resistivity is more sensitive to the applied current in the channel, which, in other words, indicates that heating is more apparent at lower temperatures. At maximum applied current, the resistance of the channel, nominally at 4 K, can reach the steady value equivalent to a temperature of ~ 150 K (red data) - slightly lower than the saturation temperature of the I_c observed in Fig. 8.10 (b). The slight difference is likely due to the constant heating in the switching experiments where we sweep the current a few times, thus further increasing the device temperature.

Note that in these Canon samples, due to better uniformity and strong IrMn pinning, the major loops remain clean without the distortions seen in Cornell grown

devices. Figure 8.12(a) shows a comparison of the major loops at four different temperatures, while Fig. 8.12(b) shows the minor loops indicating the increase in H_c at lower temperatures. The minor loops show an asymmetric expansion of the hysteresis loop where coercive field increases more in the dipole field direction. This is consistent with the behavior of the major loops in the negative field region where the reference layer is rotated by the large external field. From the larger saturation field at lower temperatures, it is evidenced that the pinning (exchange coupling) gets stronger at lower temperatures with the Canon stack, which may strengthen the dipole field from the reference layer to the free layer, causing the minor loop to expand more in one direction.

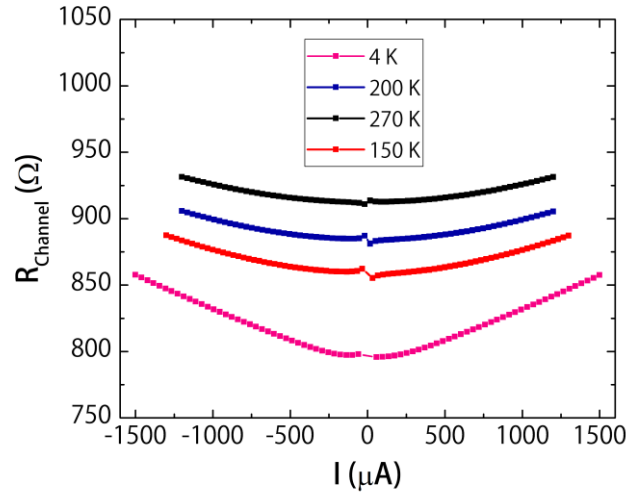


Fig. 8. 11 Channel resistance of the Canon Large 1 sample at various cryogenic temperatures

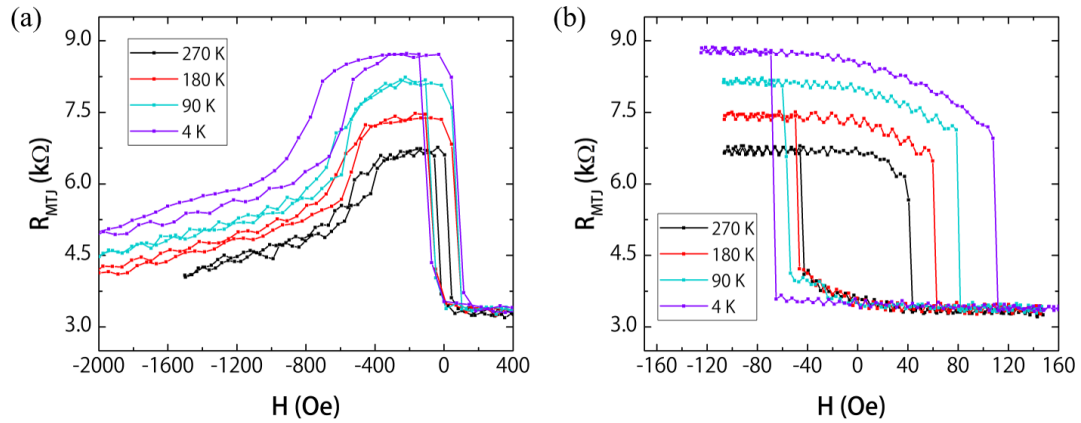


Fig. 8.12 Major (a) and minor (b) loops of a Canon Large 1 sample at low temperatures

8.3. Low temperature FMR measurements

To understand the low temperature switching behavior better, I carried out FMR measurement to find out the damping and the demagnetization field at various temperatures. I used the same cryostat and sample positioner except that I replaced the waveguide on the sample holder with an FMR waveguide that does not have the center hole. The FMR sample chip, which is taken from the edge of the device wafer, where the full magnetic stack is preserved during the device fabrication, was placed at the center of the waveguide with the magnetic stack facing down. The four corners of the chip were glued onto the waveguide with cement glue, which hardens quickly and adheres to the waveguide surface when dried in air and can be easily scraped off by a razor blade after the measurement is done.

I show the FMR results in Fig. 8.13. As temperature decreases, the demagnetization field slightly increases from 4100 Oe to 4650 Oe, which is likely due to the increase in the saturation magnetization of FeCoB at lower temperatures. The

damping parameter α increases from 0.0165 at room temperature to 0.018 at 100 K and slightly decreases at lower temperatures, except for an abnormal drop at 50 K. The increase of magnetic damping could be due to some antiferromagnetic iron oxide layers that introduce extra spin relaxation mechanism below their blocking temperatures⁹⁶. It is not clear why there is a sudden drop of damping at around 50 K, where the FMR lineshape and amplitude are still good enough not to severely affect the data processing.

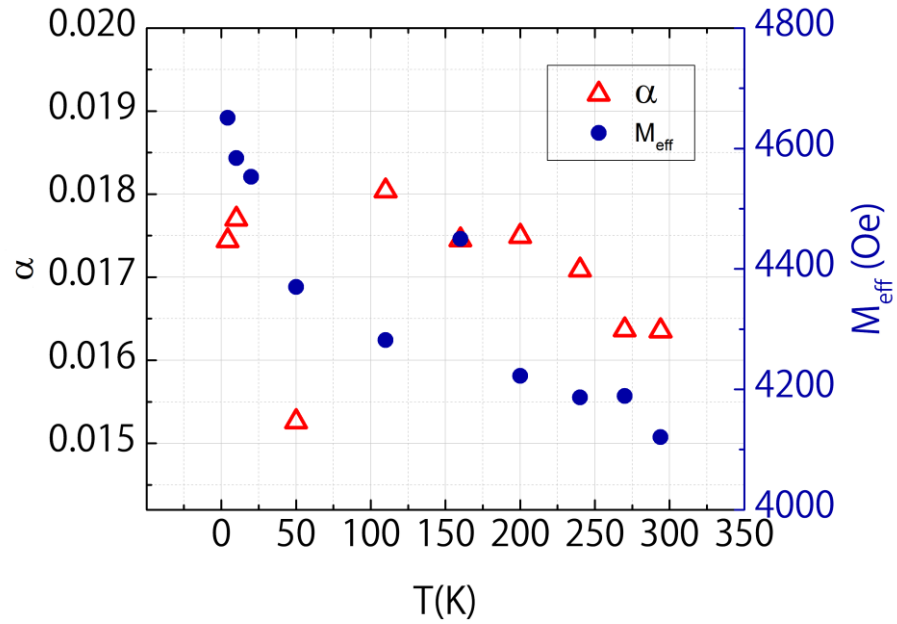


Fig. 8. 13 FMR measurement on Canon 1 sample

However, the increased M_{eff} and α qualitatively explain the increased I_c we observed in Canon Large 1 devices. Aradhya et al. reported a zero-temperature critical current density of $\sim 4 \times 10^{11}$ A/m² in a similar Pt-based 3T-MTJ structure⁶⁸. If we take this current density and calculate the current needed to switch a device on a 500-nm channel, it gives $I_c = 1$ mA, which is consistent with our observed I_c at low

temperatures given that at lower temperatures thermal fluctuation gradually freezes out and the switching current will approach the zero-temperature critical current from the macrospin fit. However this doesn't account for the independent increase of M_{eff} and α at low temperatures, which will contribute to higher I_c 's.

8.4. Switching of the MTJs under short voltage pulses at low temperatures

Next, I briefly show how the 3T-MTJs behave with short switching pulses at low temperatures. Due to the large increase in critical current (voltage) at lower temperatures, I expected that the critical short pulse voltage needed to switch the MTJs would become significantly large. Therefore, I choose to look at a W-based sample with Hf dusting which had a much smaller I_{c0} at room temperature compared to the Pt-based samples. First, I show the typical room temperature behavior of these MTJs as a comparison to the low temperature behavior that will be introduced later. The devices have a material stack of W(4)-FeCoB(1.8)-Hf(0.1)-MgO(1.6)-FeCoB(4)-Ta(5)-Pt(3)-Ru(5) ("W5"), and are annealed at 300 °C for 1 hour. In Fig. 8.14 I show the typical field and DC current switching of a device having a nominal size $190 \times 45 \text{ nm}^2$. It has $H_c \sim 35 \text{ Oe}$ (Fig. 8.14(a) inset) and I_{c0} at room temperature $\sim 130 \text{ }\mu\text{A}$ as fitted from the ramp rate measurement (Fig. 8.14(b)).

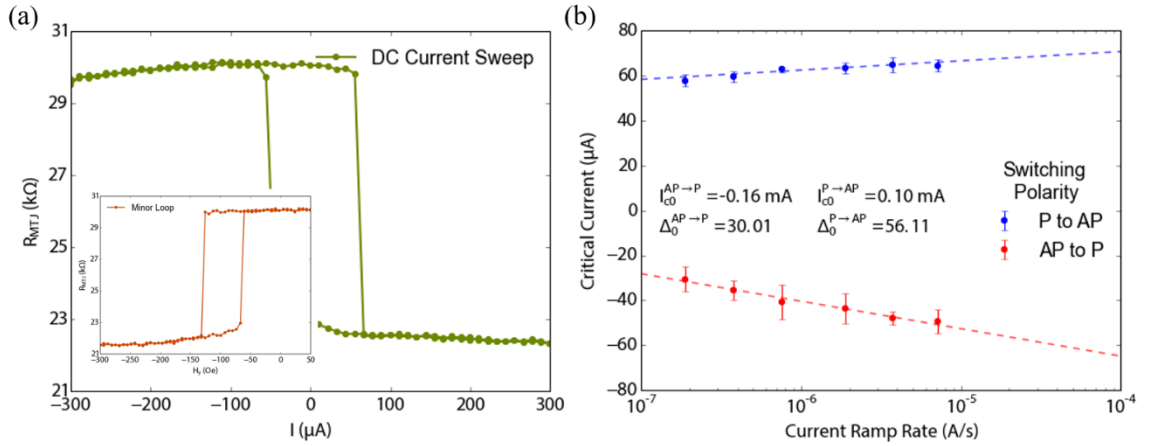


Fig. 8. 14 (a), Field and DC current switching of a typical W5 device (b), ramp rate measurement of the W5 device

I carried out pulse measurements at room temperature. Shown in Fig. 8.15(a) and (b) are pulse switching probabilities of the device at different pulse amplitudes and durations, for $P \rightarrow AP$ and $AP \rightarrow P$ respectively. Smooth probability curves with 100% probability at high voltage/large duration can be achieved for both switching polarities with a slight asymmetry possibly due to the imperfect offset field applied to balance the dipole field on the free layer given by the reference layer. Switching voltages and durations at 50% probability are extracted from the pulse curves and are plotted in Fig. 8.15(c) and (d), along with macrospin fitting curves. From the average switching voltage V_0 , we get equivalent switching current $I_{c0} \sim 133$ μA, consistent with ramp rate results shown in Fig. 8.14.

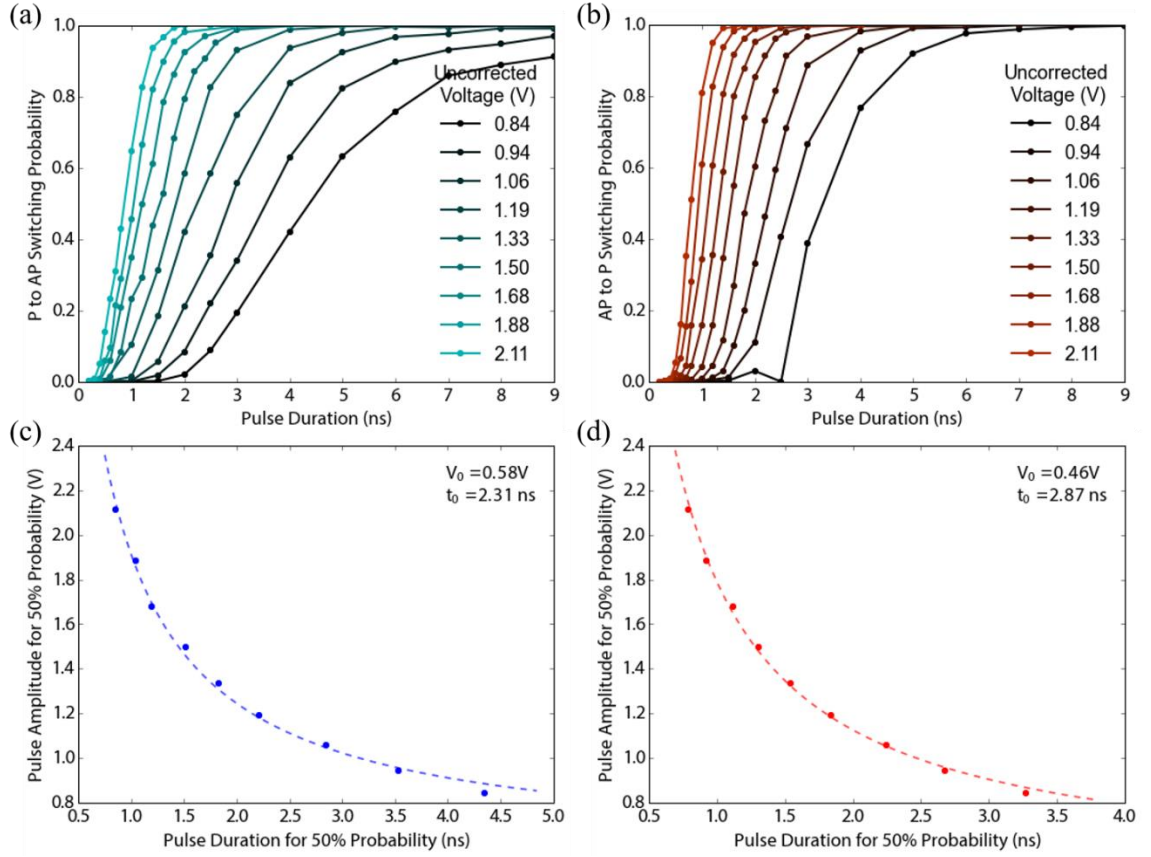


Fig. 8. 15 Pulse switching probability curves for a W5 device for P→AP and AP→P polarities (a) and (b), along with 50% probability points and macrospin fitting (c) and (d)

Next, I did low temperature pulse measurement on W5 devices in collaboration with the quantum information group at Raytheon BBN Technologies. A high frequency cryogenic probe station with automated probe-motion capability is used to enhance the measurement efficiency at as low as 4 K. We show two pulse switching phase diagrams for P→AP and AP→P in Fig. 8.16. Compared to the room temperature results, the average critical switching current, when converted from V_0 's using $R_{\text{channel}} = 3.9 \text{ k}\Omega$, is $140 \mu\text{A}$, which is slightly higher and is as expected from the DC switching comparison between at room temperature and low temperatures.

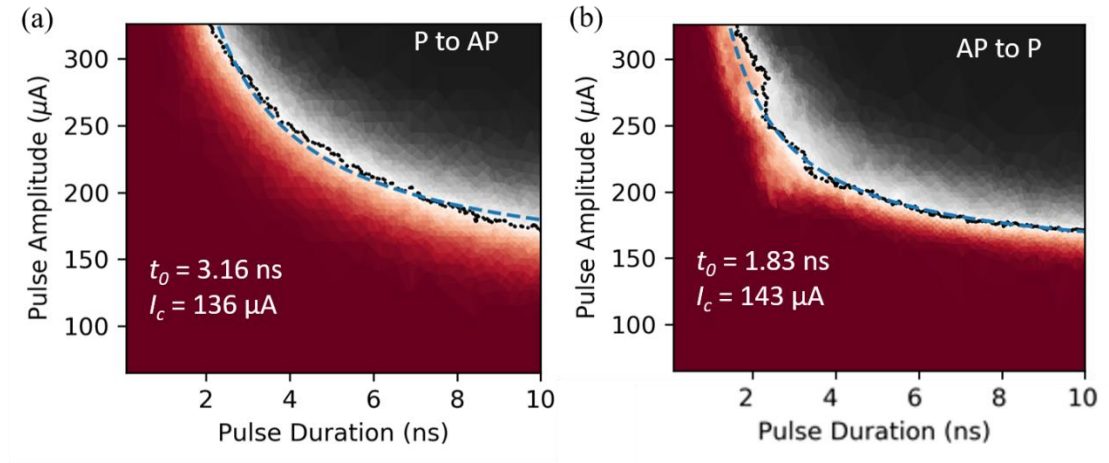


Fig. 8.16 Pulse switching phase diagrams of a W5 device at 4 K

The 4 K pulse results show that these 3T-MTJs behave well at low temperatures and can be useful for cryogenic applications such as superconducting computers. Of course with unbalanced reference layers and non-ideal film uniformity there are some regions of the phase diagrams where the switching probability fluctuates slightly which reflects potential magnetization trapping or switch-back behavior. However, the small increase in the switching current and large increase in the coercivity (and hence thermal stability) show great promise for low energy writing application and also manifests the advantage of the three terminal design that enables achieving excellent performance in different aspects at the same time.

REFERENCES

1. Baibich, M. N. *et al.* Giant Magnetoresistance of (001)Fe(001)Cr Magnetic Superlattices. *Phys. Rev. Lett.* **61**, 2472–2475 (1988).
2. Binasch, G., Grünberg, P., Saurenbach, F. & Zinn, W. Enhanced magnetoresistance in layered magnetic structures. *Phys. Rev. B* **39**, 4828–4830 (1989).
3. Slonczewski, J. C. Current-driven excitation of magnetic multilayers. *J. Magn. Magn. Mater.* **159**, L1–L7 (1996).
4. Berger, L. Emission of spin waves by a magnetic multilayer traversed by a current. *Phys. Rev. B* **54**, 9353–9358 (1996).
5. Hirsch, J. E. Spin Hall Effect. *Phys. Rev. Lett.* **83**, 1834 (1999).
6. Locatelli, N., Cros, V. & Grollier, J. Spin-torque building blocks. *Nat. Mater.* **13**, 11–20 (2014).
7. Ralph, D. C. & Stiles, M. D. Spin transfer torques. *J. Magn. Magn. Mater.* **320**, 1190–1216 (2008).
8. Liu, L. *et al.* Spin-Torque Switching with the Giant Spin Hall Effect of Tantalum. *Science* (80-.). **336**, 555–558 (2012).
9. Miron, I. M. *et al.* Perpendicular switching of a single ferromagnetic layer induced by in-plane current injection. *Nature* **476**, 189–193 (2011).
10. Pai, C. F. *et al.* Spin transfer torque devices utilizing the giant spin Hall effect of tungsten. *Appl. Phys. Lett.* **101**, 122404 (2012).
11. Pai, C.-F., Ou, Y., Vilela-Leão, L. H., Ralph, D. C. & Buhrman, R. A.

- Dependence of the efficiency of spin Hall torque on the transparency of Pt/ferromagnetic layer interfaces. *Phys. Rev. B* **92**, 064426 (2015).
12. Nguyen, M. H., Ralph, D. C. & Buhrman, R. A. Spin Torque Study of the Spin Hall Conductivity and Spin Diffusion Length in Platinum Thin Films with Varying Resistivity. *Phys. Rev. Lett.* **116**, 1–6 (2016).
 13. Nguyen, M. H., Zhao, M., Ralph, D. C. & Buhrman, R. A. Enhanced spin Hall torque efficiency in Pt_{100-x}Al_x and Pt_{100-x}Hf_x alloys arising from the intrinsic spin Hall effect. *Appl. Phys. Lett.* **108**, 242407 (2016).
 14. Nguyen, M. H. *et al.* Efficient switching of 3-terminal magnetic tunnel junctions by the giant spin Hall effect of Pt₈₅Hf₁₅ alloy. *Appl. Phys. Lett.* **112**, 062404 (2018).
 15. Ou, Y., Shi, S., Ralph, D. C. & Buhrman, R. A. Strong Spin Hall Effect in the Antiferromagnet PtMn. *Phys. Rev. B* **93**, 220405(R) (2016).
 16. Fukami, S., Zhang, C., Duttagupta, S., Kurenkov, A. & Ohno, H. Magnetization switching by spin-orbit torque in an antiferromagnet / ferromagnet bilayer system. *Nat. Mater.* **15**, 535–542 (2016).
 17. Gibbons, J. D., Macneill, D., Buhrman, R. A. & Ralph, D. C. Reorientable Spin Direction for Spin Current Produced by the Anomalous Hall Effect. *Phys. Rev. Appl.* **9**, 64033 (2018).
 18. Ou, Y., Ralph, D. C. & Buhrman, R. A. Strong Enhancement of the Spin Hall Effect by Spin Fluctuations near the Curie Point of Fe_xPt_{1-x} Alloys. *Phys. Rev. Lett.* **120**, 97203 (2018).
 19. Mellnik, A. R. *et al.* Spin-transfer torque generated by a topological insulator.

- Nature* **511**, 449–451 (2014).
20. MacNeill, D. *et al.* Control of spin-orbit torques through crystal symmetry in WTe₂/ferromagnet bilayers. *Nat. Phys.* **13**, 300–305 (2017).
 21. Katine, J., Albert, F., Buhrman, R., Myers, E. & Ralph, D. Current-Driven Magnetization Reversal and Spin-Wave Excitations in Co /Cu /Co Pillars. *Phys. Rev. Lett.* **84**, 3149–3152 (2000).
 22. Myers, E. B., Ralph, D. C., Katine, J. A., Louie, R. N. & Buhrman, R. A. Current-Induced Switching of Domains in Magnetic Multilayer Devices. *Science* (80-.). **285**, 867–870 (1999).
 23. Fuchs, G. D. *et al.* Spin torque, tunnel-current spin polarization, and magnetoresistance in MgO magnetic tunnel junctions. *Phys. Rev. Lett.* **96**, 1–4 (2006).
 24. Julliere, M. Tunneling between ferromagnetic films. *Phys. Lett.* **54**, 225–226 (1975).
 25. Soulen, R. J. *et al.* Measuring the Spin Polarization of a Metal with a Superconducting Point Contact. *Science* (80-.). **282**, 85–88 (1998).
 26. Yuasa, S., Nagahama, T., Fukushima, A., Suzuki, Y. & Ando, K. Giant room-temperature magnetoresistance in single-crystal Fe/MgO/Fe magnetic tunnel junctions. *Nat. Mater.* **3**, 868–871 (2004).
 27. Parkin, S. S. P. *et al.* Giant tunnelling magnetoresistance at room temperature with MgO (100) tunnel barriers. *Nat. Mater.* **3**, 862–867 (2004).
 28. Ikeda, S. *et al.* Tunnel magnetoresistance of 604% at 300 K by suppression of Ta diffusion in CoFeBMgOCoFeB pseudo-spin-valves annealed at high

- temperature. *Appl. Phys. Lett.* **93**, 1–4 (2008).
29. Fuchs, G. D. *et al.* Spin-transfer effects in nanoscale magnetic tunnel junctions. *Appl. Phys. Lett.* **85**, 1205–1207 (2004).
 30. Katine, J. A. & Fullerton, E. E. Device implications of spin-transfer torques. *J. Magn. Magn. Mater.* **320**, 1217–1226 (2008).
 31. Shi, S., Ou, Y., Aradhya, S. V., Ralph, D. C. & Buhrman, R. A. Fast Low-Current Spin-Orbit-Torque Switching of Magnetic Tunnel Junctions through Atomic Modifications of the Free-Layer Interfaces. *Phys. Rev. Appl.* **9**, 011002 (2018).
 32. Fukami, S., Anekawa, T., Zhang, C. & Ohno, H. A spin-orbit torque switching scheme with collinear magnetic easy axis and current configuration. *Nat. Nanotechnol.* **11**, 621–625 (2016).
 33. Yu, G. *et al.* Switching of perpendicular magnetization by spin-orbit torques in the absence of external magnetic fields. *Nat. Nanotechnol.* **9**, 548–554 (2014).
 34. Lau, Y. C., Betto, D., Rode, K., Coey, J. M. D. & Stamenov, P. Spin-orbit torque switching without an external field using interlayer exchange coupling. *Nat. Nanotechnol.* **11**, 758–762 (2016).
 35. Cai, K. *et al.* Electric field control of deterministic current-induced magnetization switching in a hybrid ferromagnetic/ferroelectric structure. *Nat. Mater.* **16**, 712–716 (2017).
 36. Ma, Q. *et al.* Switching a Perpendicular Ferromagnetic Layer by Competing Spin Currents. *Phys. Rev. Lett.* **120**, 117703 (2018).
 37. Chen, T.-Y., Chan, H.-I., Liao, W.-B. & Pai, C.-F. Current-Induced Spin-Orbit

- Torque and Field-Free Switching in Mo-Based Magnetic Heterostructures. *Phys. Rev. Appl.* **10**, 044038 (2018).
38. Oh, Y. W. *et al.* Field-free switching of perpendicular magnetization through spin-orbit torque in antiferromagnet/ferromagnet/oxide structures. *Nat. Nanotechnol.* **11**, 878–884 (2016).
 39. You, L. *et al.* Switching of perpendicularly polarized nanomagnets with spin orbit torque without an external magnetic field by engineering a tilted anisotropy. *Proc. Natl. Acad. Sci.* **112**, 10310–10315 (2015).
 40. Van Den Brink, A. *et al.* Field-free magnetization reversal by spin-Hall effect and exchange bias. *Nat. Commun.* **7**, 10854 (2016).
 41. Bedau, D. *et al.* Spin-transfer pulse switching: From the dynamic to the thermally activated regime. *Appl. Phys. Lett.* **97**, (2010).
 42. Diao, Z. *et al.* Spin-transfer torque switching in magnetic tunnel junctions and spin-transfer torque random access memory. *J. Phys. Condens. Matter* **19**, 165209 (2007).
 43. Kent, A. D. & Worledge, D. C. A new spin on magnetic memories. *Nat. Nanotechnol.* **10**, 187–191 (2015).
 44. Liu, H. *et al.* Dynamics of spin torque switching in all-perpendicular spin valve nanopillars. *J. Magn. Magn. Mater.* **358–359**, 233–258 (2014).
 45. Garello, K. *et al.* Ultrafast magnetization switching by spin-orbit torques. *Appl. Phys. Lett.* **105**, 30–34 (2014).
 46. Safeer, C. K. *et al.* Spin-orbit torque magnetization switching controlled by geometry. *Nat. Nanotechnol.* **11**, 143–146 (2015).

47. Zhang, J. *et al.* Role of Micromagnetic States on Spin-Orbit Torque-Switching Schemes. *Nano Lett.* **18**, 4074–4080 (2018).
48. Yu, G. *et al.* Switching of perpendicular magnetization by spin-orbit torques in the absence of external magnetic fields. *Nat. Nanotechnol.* **9**, 548–554 (2014).
49. Hellman, F., Van Dover, R. B. & Gyorgy, E. M. Unexpected unidirectional anisotropy in amorphous Tb-Fe/Ni-Fe-Mo bilayer films. *Appl. Phys. Lett.* **50**, 296–298 (1987).
50. Shiomi, S., Kato, J., Saito, S., Kobayashi, T. & Masuda, M. Tilted uniaxial magnetic anisotropy in sputtered TbFeCo films. *Japanese J. Appl. Physics, Part 2 Lett.* **33**, (1994).
51. Krupa, N. N. Spin-dependent tunneling conductance in TbCoFe/Pr₆O₁₁/TbCoFe films. *JETP Lett.* **87**, 548–550 (2008).
52. Zhao, Z., Jamali, M., Smith, A. K. & Wang, J. P. Spin Hall switching of the magnetization in Ta/TbFeCo structures with bulk perpendicular anisotropy. *Appl. Phys. Lett.* **106**, 1–5 (2015).
53. Zhang, P. X. *et al.* Spin-orbit torque in a completely compensated synthetic antiferromagnet. *Phys. Rev. B* **97**, 1–7 (2018).
54. Zhang, W. *et al.* All-electrical manipulation of magnetization dynamics in a ferromagnet by antiferromagnets with anisotropic spin Hall effects. *Phys. Rev. B - Condens. Matter Mater. Phys.* **92**, 1–7 (2015).
55. Tshitoyan, V. *et al.* Electrical manipulation of ferromagnetic NiFe by antiferromagnetic IrMn. *Phys. Rev. B - Condens. Matter Mater. Phys.* **92**, 1–11 (2015).

56. Zhang, W. *et al.* Spin hall effects in metallic antiferromagnets. *Phys. Rev. Lett.* **113**, 1–6 (2014).
57. Chen, H., Niu, Q. & Macdonald, A. H. Anomalous hall effect arising from noncollinear antiferromagnetism. *Phys. Rev. Lett.* **112**, 1–5 (2014).
58. Mendes, J. B. S. *et al.* Large inverse spin Hall effect in the antiferromagnetic metal Ir₂₀ Mn₈₀. *Phys. Rev. B - Condens. Matter Mater. Phys.* **89**, 1–5 (2014).
59. Nguyen, M.-H. *et al.* Enhancement of the anti-damping spin torque efficacy of platinum by interface modification. *Appl. Phys. Lett.* **106**, 222402 (2015).
60. Lee, O. J. *et al.* Central role of domain wall depinning for perpendicular magnetization switching driven by spin torque from the spin Hall effect. *Phys. Rev. B - Condens. Matter Mater. Phys.* **89**, 1–8 (2014).
61. Haazen, P. P. J. *et al.* Domain wall depinning governed by the spin Hall effect. *Nat. Mater.* **12**, 299–303 (2013).
62. Baumgartner, M. *et al.* Spatially and time-resolved magnetization dynamics driven by spin-orbit torques. *Nat. Nanotechnol.* **12**, 980–986 (2017).
63. Tetienne, J. P. *et al.* The nature of domain walls in ultrathin ferromagnets revealed by scanning nanomagnetometry. *Nat. Commun.* **6**, 1–6 (2015).
64. Allwood, D. A. *et al.* Magnetic domain-wall logic. *Science (80-.).* **309**, 1688–1692 (2005).
65. Omari, K. A. & Hayward, T. J. Chirality-based vortex domain-wall logic gates. *Phys. Rev. Appl.* **2**, 1–9 (2014).
66. Omari, K. *et al.* Ballistic rectification of vortex domain wall chirality at nanowire corners. *Appl. Phys. Lett.* **107**, (2015).

67. Rowlands, G. E. *et al.* Nanosecond magnetization dynamics during spin Hall switching of in-plane magnetic tunnel junctions. *Appl. Phys. Lett.* **110**, 122402 (2017).
68. Aradhya, S. V., Rowlands, G. E., Oh, J., Ralph, D. C. & Buhrman, R. A. Nanosecond-Timescale Low Energy Switching of In-Plane Magnetic Tunnel Junctions through Dynamic Oersted-Field-Assisted Spin Hall Effect. *Nano Lett.* **16**, 5987–5992 (2016).
69. Parkin, S. S., Hayashi, M. & Thomas, L. Magnetic domain-wall racetrack memory. *Science* (80-.). **56**, 1552–1565 (2008).
70. Parkin, S. & Yang, S.-H. Memory on the racetrack. *Nat. Nanotechnol.* **10**, 195–198 (2015).
71. Hao, Q. & Xiao, G. Giant Spin Hall Effect and Switching Induced by Spin-Transfer Torque in a W/Co₄₀Fe₄₀B₂₀/MgO Structure with Perpendicular Magnetic Anisotropy. *Phys. Rev. Appl.* **3**, 1–6 (2015).
72. Liu, L., Lee, O. J., Gudmundsen, T. J., Ralph, D. C. & Buhrman, R. A. Current-induced switching of perpendicularly magnetized magnetic layers using spin torque from the spin hall effect. *Phys. Rev. Lett.* **109**, 1–5 (2012).
73. Å, G. J. *et al.* High Spin Torque Efficiency of Magnetic Tunnel Junctions with MgO/CoFeB/MgO Free Layer. **5**, 1 (2012).
74. Rahman, M. T. *et al.* Reduction of switching current density in perpendicular magnetic tunnel junctions by tuning the anisotropy of the CoFeB free layer. *J. Appl. Phys.* **111**, 7–9 (2012).
75. Liu, L., Moriyama, T., Ralph, D. C. & Buhrman, R. A. Reduction of the spin-

- torque critical current by partially canceling the free layer demagnetization field. *Appl. Phys. Lett.* **94**, 19–21 (2009).
76. Moriyama, T. *et al.* Tunnel magnetoresistance and spin torque switching in MgO-based magnetic tunnel junctions with a Co/Ni multilayer electrode. *Appl. Phys. Lett.* **97**, 4–6 (2010).
 77. Liu, R. S. *et al.* Reducing spin-torque switching current by incorporating an ultra-thin Ta layer with CoFeB free layer in magnetic tunnel junctions. *Appl. Phys. Lett.* **105**, 2012–2015 (2014).
 78. Lee, J. M. *et al.* Oscillatory spin-orbit torque switching induced by field-like torques. *Commun. Phys.* **1**, 2 (2018).
 79. Min, T. *et al.* A Study of Write Margin of Spin Torque Transfer Magnetic Random Access Memory Technology. *IEEE Trans. Magn.* **46**, 2322–2327 (2010).
 80. Sun, J. Spin-current interaction with a monodomain magnetic body: A model study. *Phys. Rev. B* **62**, 570–578 (2000).
 81. Dieny, B. & Chshiev, M. Perpendicular magnetic anisotropy at transition metal/oxide interfaces and applications. *Rev. Mod. Phys.* **89**, (2017).
 82. Wang, W. X. *et al.* The perpendicular anisotropy of Co₄₀Fe₄₀B₂₀ sandwiched between Ta and MgO layers and its application in CoFeB/MgO/CoFeB tunnel junction. *Appl. Phys. Lett.* **99**, (2011).
 83. Sinha, J. *et al.* Influence of boron diffusion on the perpendicular magnetic anisotropy in Ta/CoFeB/MgO ultrathin films. *J. Appl. Phys.* **117**, 043913 (2015).

84. Mukherjee, S. *et al.* Role of boron diffusion in CoFeB/MgO magnetic tunnel junctions. *Phys. Rev. B - Condens. Matter Mater. Phys.* **91**, 1–6 (2015).
85. Yang, H. X. *et al.* First-principles investigation of the very large perpendicular magnetic anisotropy at Fe|MgO and Co|MgO interfaces. *Phys. Rev. B - Condens. Matter Mater. Phys.* **84**, 1–5 (2011).
86. Ou, Y., Pai, C.-F., Shi, S., Ralph, D. C. & Buhrman, R. A. Origin of fieldlike spin-orbit torques in heavy metal-ferromagnet-oxide thin film heterostructures. *Phys. Rev. B* **94**, 140414(R) (2016).
87. Ou, Y., Ralph, D. C. & Buhrman, R. A. Strong perpendicular magnetic anisotropy energy density at Fe alloy/HfO₂ interfaces. *Appl. Phys. Lett.* **110**, 192403 (2017).
88. Nguyen, M.-H. H. *et al.* Enhancement of the anti-damping spin torque efficacy of platinum by interface modification. *Appl. Phys. Lett.* **106**, 222402 (2015).
89. Lee, D. Y., Lee, S. E., Shim, T. H. & Park, J. G. Tunneling-Magnetoresistance Ratio Comparison of MgO-Based Perpendicular-Magnetic-Tunneling-Junction Spin Valve Between Top and Bottom Co₂Fe₆B₂Free Layer Structure. *Nanoscale Res. Lett.* **11**, 1–7 (2016).
90. Hao, Q., Chen, W. & Xiao, G. Beta (β) tungsten thin films: Structure, electron transport, and giant spin Hall effect. *Appl. Phys. Lett.* **106**, (2015).
91. O’Keefe, M. J. & Grant, J. T. Phase transformation of sputter deposited tungsten thin films with A-15 structure. *J. Appl. Phys.* **79**, 9134–9141 (1996).
92. Kurt, H., Oguz, K., Niizeki, T. & Coey, J. M. D. Giant tunneling magnetoresistance with electron beam evaporated MgO barrier and CoFeB

- electrodes. *J. Appl. Phys.* **107**, (2010).
93. Read, J. C. *et al.* High magnetoresistance tunnel junctions with Mg-B-O barriers and Ni-Fe-B free electrodes. *Appl. Phys. Lett.* **94**, 1–4 (2009).
 94. Pai, C. F. *et al.* Enhancement of perpendicular magnetic anisotropy and transmission of spin-Hall-effect-induced spin currents by a Hf spacer layer in W/Hf/CoFeB/MgO layer structures. *Appl. Phys. Lett.* **104**, 082407 (2014).
 95. Mondal, S. *et al.* All-optical detection of the spin Hall angle in W/CoFeB/SiO₂ heterostructures with varying thickness of the tungsten layer. *Phys. Rev. B* **96**, 1–8 (2017).
 96. Ozatay, O. *et al.* Sidewall oxide effects on spin-torque- and magnetic-field-induced reversal characteristics of thin-film nanomagnets. *Nat. Mater.* **7**, 567–573 (2008).
 97. Liu, L. *et al.* Spin-Torque Switching with the Giant Spin Hall Effect of Tantalum. *Science* (80-.). **336**, 555–558 (2012).
 98. Fukami, S. & Ohno, H. Magnetization switching schemes for nanoscale three-terminal spintronics devices. *Jpn. J. Appl. Phys* **56**, 0802A1 (2017).
 99. Cubukcu, M. *et al.* Spin-orbit torque magnetization switching of a three-terminal perpendicular magnetic tunnel junction. *Appl. Phys. Lett.* **104**, 042406 (2014).
 100. Fukami, S. *et al.* Electrical endurance of Co/Ni wire for magnetic domain wall motion device. *Appl. Phys. Lett.* **102**, 222410 (2013).
 101. Sun, J. Z. *et al.* Effect of subvolume excitation and spin-torque efficiency on magnetic switching. *Phys. Rev. B* **84**, 064413 (2011).

102. Demasius, K.-U. *et al.* Enhanced spin orbit torques by oxygen incorporation in tungsten films. *Nat. Commun.* **7**, 10644 (2015).
103. Sagasta, E. *et al.* Tuning the spin Hall effect of Pt from the moderately dirty to the superclean regime. *Phys. Rev. B* **94**, 1–6 (2016).
104. Han, D. S. *et al.* Asymmetric hysteresis for probing Dzyaloshinskii-Moriya interaction. *Nano Lett.* **16**, 4438–4446 (2016).
105. Guenole, J. *et al.* Achieving Sub-ns switching of STT-MRAM for future embedded LLC applications through improvement of nucleation and propagation switching mechanisms. *Dig. Tech. Pap. - Symp. VLSI Technol.* **2016–Septe**, 50–51 (2016).
106. Nowak, J. J. *et al.* Dependence of Voltage and Size on Write Error Rates in Spin-Transfer Torque Magnetic Random-Access Memory. *IEEE Magn. Lett.* **7**, 4–7 (2016).
107. Cubukcu, M. *et al.* Dzyaloshinskii-Moriya anisotropy in nanomagnets with in-plane magnetization. *Phys. Rev. B* **93**, 1–5 (2016).
108. Chien-Tu Chao *et al.* Temperature Dependence of Electrical Transport and Magnetization Reversal in Magnetic Tunnel Junction. *IEEE Trans. Magn.* **46**, 2195–2197 (2010).
109. Wang, S. G. *et al.* Temperature dependence of giant tunnel magnetoresistance in epitaxial Fe/MgO/Fe magnetic tunnel junctions. *Phys. Rev. B - Condens. Matter Mater. Phys.* **78**, 2–5 (2008).
110. Drewello, V., Schmalhorst, J., Thomas, A. & Reiss, G. Evidence for strong magnon contribution to the TMR temperature dependence in MgO based tunnel

- junctions. *Phys. Rev. B - Condens. Matter Mater. Phys.* **77**, 1–5 (2008).
111. Gan, H. D. *et al.* Origin of the collapse of tunnel magnetoresistance at high annealing temperature in CoFeB/MgO perpendicular magnetic tunnel junctions. *Appl. Phys. Lett.* **99**, (2011).
 112. Yang, Z. *et al.* A study on pinned layer magnetization processes in different antiferromagnetic coupling systems of spin-valves. *J. Appl. Phys.* **87**, 5729–5731 (2000).
 113. Martí, X. *et al.* Electrical measurement of antiferromagnetic moments in exchange-coupled IrMn/NiFe stacks. *Phys. Rev. Lett.* **108**, 1–4 (2012).
 114. Tsai, M. C., Cheng, C. W., Tsai, C. C. & Chern, G. The intrinsic temperature dependence and the origin of the crossover of the coercivity in perpendicular MgO/CoFeB/Ta structures. *J. Appl. Phys.* **113**, 2011–2014 (2013).
 115. Liu, H. *et al.* Manipulation of magnetization switching and tunnel magnetoresistance via temperature and voltage control. *Sci. Rep.* **5**, 1–8 (2015).
 116. Vertesy, G., Pust, L., Tomas, I. & Paces, J. Direct measurement of domain wall coercive field. *J. Phys. D Appl. Phys* **24**, 1482 (1991).
 117. Nunes, W. C., Folly, W. S. D., Sinnecker, J. P. & Novak, M. A. Temperature dependence of the coercive field in single-domain particle systems. *Phys. Rev. B - Condens. Matter Mater. Phys.* **70**, 1–6 (2004).